8-4-2017

Nanoparticle-Based Drug-Delivery Systems Studied by Second Harmonic Generation

Raju Ram Kumal
Louisiana State University and Agricultural and Mechanical College, rajuramkumal@hotmail.com

NANOPARTICLE-BASED DRUG-DELIVERY SYSTEMS STUDIED BY SECOND HARMONIC GENERATION

A Dissertation

Submitted to the Graduate Faculty of the
Louisiana State University and
Agricultural and Mechanical
College in partial fulfillment of the
requirements for the degree of
Doctor of Philosophy

in

The Department of Chemistry

by
Raju Ram Kumal
M. Sc., Tribhuvan University, 2008
B. Sc., Tribhuvan University, 2006
December 2017

Dedicated to

My Father and Mother

My Wife Muna and my children Prinsa and Ruben

ACKNOWLEDGEMENTS

I am deeply grateful to my advisor, Professor Louis H Haber for giving me an opportunity to join his group and for his continued support to complete this journey. Thank you for your incredible guidance, feedback, encouragement and your valuable time to make my PhD very productive. It was a wonderful experience working with you. You are the best professor and mentor anyone could ask for.

I am very grateful to Professor Robin L. McCarley for his constant support and encouragements. It was a golden opportunity for me to be a part of collaborative work with his group. I am thankful for his creative collaboration, wonderful ideas, great support and valuable time. Additionally, I would like to express my sincere gratitude to Professor Bin Chen and Professor Sunggook Park for their valuable time and guidance. I am also thankful to Professor Daniel Hayes for his support and being a part of the collaborative work with his group. Additionally, being a recipient of the Coates Scholar Research Award, I would like to acknowledge Coates Family for their generous financial support.

It is not possible to do science by yourself without the help of other people. Here are few people without their heroic efforts the collaborative works would not have been possible. I would like to thank Dr. James Winter and Huy Nguyen for liposome samples and active involvement in the projects. Similarly, I am grateful to Mohammad Abu-Laban and Corey Landry for micro-RNA projects and all of the valuable discussions we had. Both were very helpful and creative to finish the projects. I would like to thank our wonderful and hardworking undergraduate students Blake Kruger and Nikka Khorsandi for their help in nanoparticle synthesis.

I am also grateful to Dr. Raphael Cueto for his valuable advice and help in dynamic light scattering and zeta potential measurements.mI am also grateful to Ying Xiao for her help with transmission electron microscopy and Dr. Thomas Blanchard for his help with ICP-OES measurement for nanoparticles. No acknowledgements are complete without remembering the wonderful people working in the same lab. I am grateful to Dr. Zhenyu Zhang, Dr. Tony Karam, Rami Khoury, Jeewan Ranasinghe, Holden Smith, Joel Taylor, Prakash Hamal and Asela Sampath Dikkumbura for valuable discussion, great help and active collaborations. You are the most wonderful guys in the world.

Last but not least, I wish to thank my family members for their love, continued support, encouragement and their sacrifices to complete my PhD journey. I am also thankful to Dr. Uttam Pokharel, Dr. Suresh Regmi and Dr. Bishnu Regmi for their great help and valuable advice.

TABLE OF CONTENTS

LIST OF ABBREVIATIONS

Abbreviation	Name
SHG	second harmonic generation
SFG	sum frequency generation
MSA	mercaptosuccinic acid
miRNA	micro ribonucleic acid
UV	ultraviolet
NIR	near-infrared
TEM	transmission electron microscopy
CCD	charge-coupled device
MG	malachite green
MetG	methyl green
DLS	dynamic light scattering
$AgNO_3$	silver nitrate
NaOH	sodium hydroxide
CS	core-shell
CSS	core-shell-shell
ICP-OES	inductively coupled plasma optical emission spectroscopy
OPA	optical parametric amplifier
NaCl	sodium chloride
$HAuCl_4$	gold chloride
Au	gold
DOPG	dioleoylphosphatidylglycerol

DOPS	dioleoylphosphoserine
QDOPE	tri-methyl quinone dioleoylphosphoethanolamine
DOPC	dioleoylphosphocholine

ABSTRACT

Second harmonic generation (SHG) is used to study different types of colloidal nanoparticle drug-delivery systems. The surface charge density, electrostatic surface potentials, and ion adsorptions of 50 nm colloidal gold nanoparticle samples coated with mercaptosuccinic acid are determined using SHG measurements under varying NaCl and $MgCl_2$ concentrations in water. Numerical solutions to the spherical Poisson-Boltzmann equation are fit to the SHG results to account for the nanoparticle surface curvature and ion adsorption to the Stern layer interface, showing excellent agreement with electrophoretic mobility measurements. In another study, nanoparticles of gold, silver and polystyrene are functionalized with microRNA using a nitrobenzyl photocleavable linker that cleaves upon ultraviolet irradiation. The SHG is shown to be a sensitive probe for monitoring the photocleaving dynamics of the oligonucleotides in real time. The photoactivated controlled release is observed to be most efficient on resonance at 365 nm irradiation, with pseudo-first-order rate constants that are linearly proportional to irradiation powers. Silver nanoparticles show an approximate 6-fold plasmon enhancement in photocleaving efficiency over corresponding polystyrene nanoparticles and an approximate 3-fold plasmon enhancement over gold nanoparticles. Additionally, gold-silver-gold core-shell-shell nanoparticles are prepared and are functionalized with miRNA using Diels-Alder chemistry. The plasmonic extinction peak of these nanoparticles, centered at near-infrared (NIR) wavelengths, that can be controlled by varying the thickness of gold and silver shells. Photothermal release of oligonucleotides from the nanoparticle surface under NIR irradiation is studied for drug-delivery applications in the NIR optical window of biological tissue. Lastly, SHG is used to investigate molecular adsorption and transport kinetics of positively charged dyes at the surface of liposomes in water. The adsorption and time-dependent SHG results are analyzed to obtain the free energies

of adsorption, the adsorption site densities, and the transport kinetics under varying liposome chemistries and buffer conditions. Parameters such as electrostatic interactions, the chemical structure of the lipid head group, the buffer conductivity, ion-pair formation and adsorbate-adsorbate repulsion are found to influence the adsorption and transport at the liposome surface. In all of these studies, real-time SHG measurements are shown to be highly sensitive for investigating surface dynamics in nanoparticle-based drug delivery systems.

CHAPTER 1
INTRODUCTION

1.1 Metallic Nanoparticles

Metallic nanoparticles have drawn great interest due to their unique properties which can be utilized in nanomedicine, sensing, catalysis, and optoelectronic fields.[1] They are a bridge between the corresponding metallic atoms and bulk materials. Metallic nanoparticles also have important optical properties derived from surface plasmon resonances (SPRs) which are characterized by the coherent oscillation of free electrons under incident light.[2-5]

Gold and silver nanoparticles have been widely used due to their many unique physical, chemical, and optical properties that are useful for biological applications such as molecular sensing, labelling, drug delivery, and photothermal cancer treatment.[6-9] The ease of synthesis, biocompatibility, and the functionalization with biomolecules through thiolation have led to the developments in diagnostic and therapeutic nanomedicines.[8, 10] Nanoparticles having various geometries such as nanorods,[11] nanocages,[12] and nanoshells[13] have been synthesized and studied extensively due to their tunable optical properties. These nanomaterials are attractive for optical contrast enhancement agents and for cancer diagnosis and treatment. In order to develop and optimize potential biological applications of metallic nanoparticles, it is important to more fully understand the surface chemistries and surface charge densities of metallic nanoparticles in aqueous colloidal suspension. [6-9]

Metallic core-shell or core-shell-shell nanoparticles are layered nanoparticles consisting of a core surrounded by a shell or by two shells of different metallic materials.[14] These nanoparticles can be very useful in nanomedicine and catalysis due to their diverse functionalities and optical properties that are provided by the layered hybrid nanostructures.[15-17] Gold and silver

core-shell nanoparticles, in particular, exhibit strong optical plasmon resonances which are usually shifted to longer wavelengths compared to the single corresponding nanospheres.[18] The plasmon peaks of these core-shell nanoparticles can be tuned from visible to the near infrared region by changing the shell material and its thickness. Multilayered gold-silver-gold core-shell-shell nanoparticles can be used in drug delivery and photothermal treatments of tumors due to their affinity to bind with biological molecules and their ability to absorb near infrared radiation with high photothermal efficiencies.[19] Figure 1.1 shows representative transmission microscopy (TEM) images of gold (68 ± 7 nm), silver (65 ± 7 nm), gold-silver core-shell (60 ± 7 nm) and gold-silver-gold core-shell-shell (140 ± 10 nm) nanoparticles produced in our laboratory. Figure 1.2 shows the extinction spectra of these silver, gold and gold-silver-gold core-shell-shell nanoparticles.

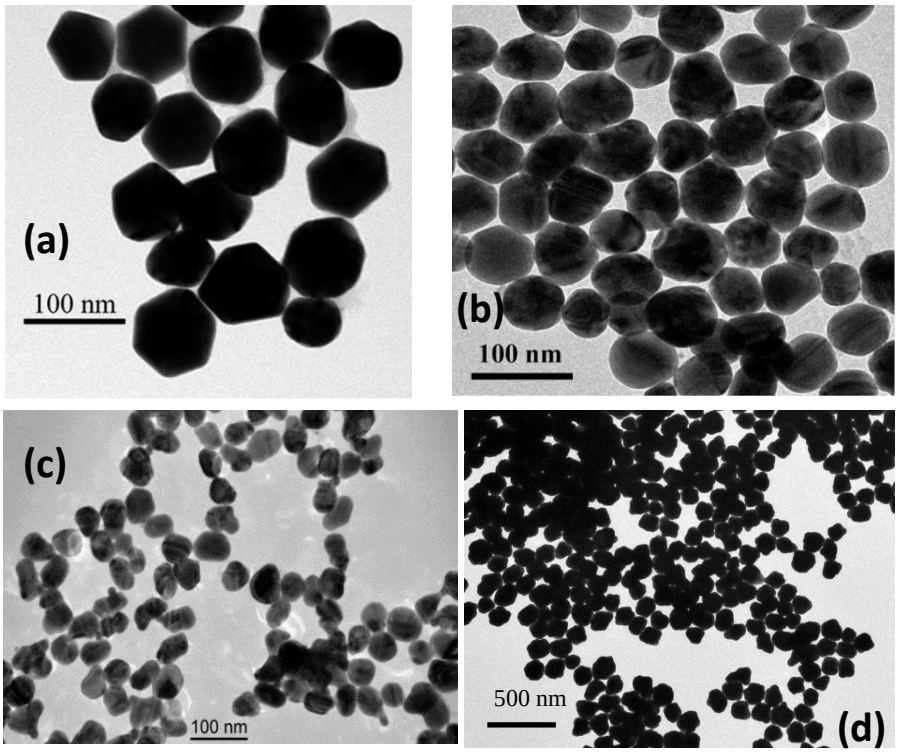

Figure 1.1**.** Representative TEM images of (a) gold, (b) silver, (c) gold-silver core-shell, and (d) gold-silver-gold core-shell-shell nanoparticles.

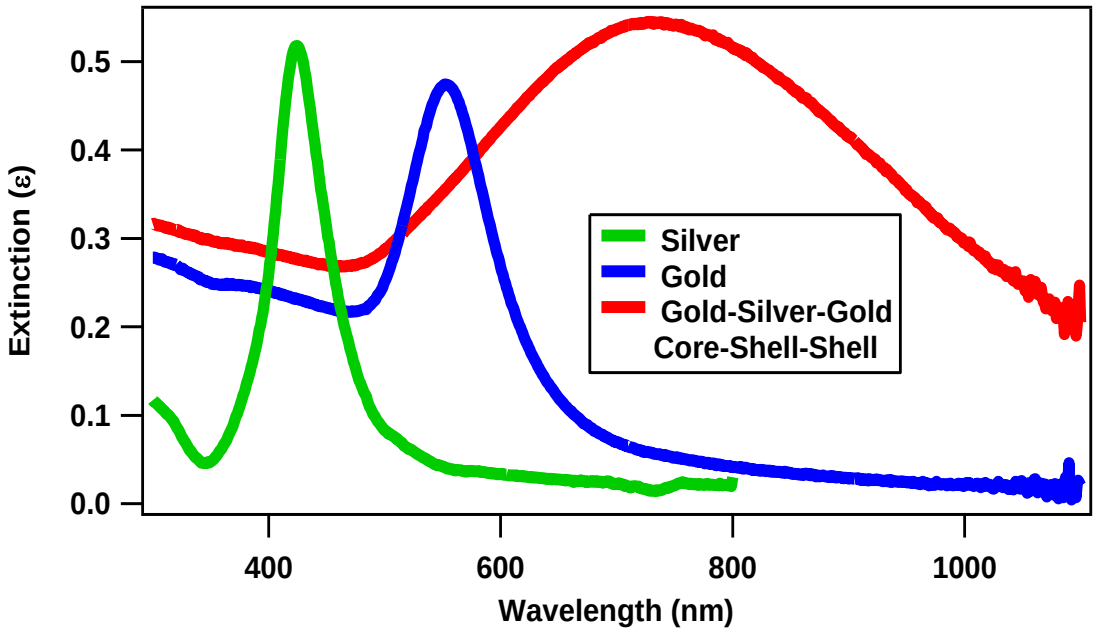

Figure 1.2. Extinction spectra of gold, silver, and gold-silver-gold core-shell-shell nanoparticles showing the plasmon peaks at different wavelengths.

1.2 Surface Plasmon Resonances

The localized surface plasmon resonances of metallic nanoparticles are characterized by the coherent oscillations of free electrons in the conduction band induced by incident electromagnetic radiation, where the plasmon energies depend on the nanoparticle size, shape, composition, and surrounding medium.[20-24] Surface plasmons interact strongly with nearby molecules and can lead to significant optical field enhancements for processes such as surface-enhanced Raman scattering (SERS) and molecular fluorescence.[25-28] Surface plasmons of nanoparticles can be tuned from ultraviolet to infrared photon energies for various applications including plasmonic tags and particle-based therapies,[29-31] biological and chemical sensing,[32-37] and catalysis.[38-41] Figure 1.3 shows an illustration of a surface plasmon resonance of a metallic nanoparticle induced by an optical electromagnetic field.

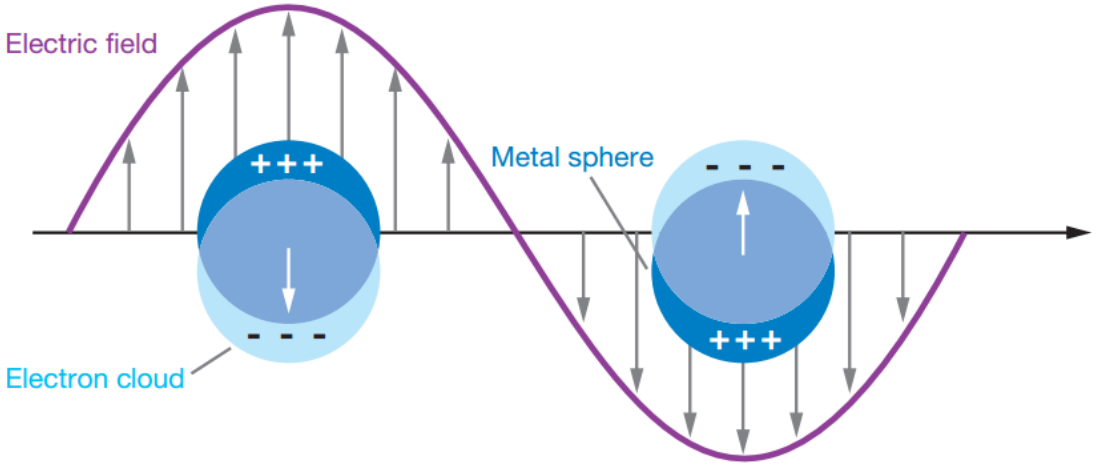

Figure 1.3. Illustration of the surface plasmon resonance of spherical metallic nanoparticle under an incident electric field.[33]

1.3 Surface Charge Density

A colloidal particle often develops charge on its surface when suspended in a solution either from adsorption of ionic species to the surface or from dissociation of ions from the surface.[42-43] A surface charge density causes a corresponding electrostatic potential to develop on the surface of the nanoparticle. The electrostatic potential decays linearly until reaching the Stern layer, and then decays approximately exponentially through the diffuse layer. A boundary line separates the double layer from the bulk electrolyte solution at the hydrodynamic radius. This boundary is called the slipping plane and the potential at this plane is defined as the zeta potential. Figure 1.4 depicts the structure of the electrical double layer and the variation of the electrostatic potential as a function of the distance from the nanoparticle surface. In order to accurately describe the interfacial chemistry and electrostatic properties of colloidal particles, it is important to determine the surface charge density (σ) and electrostatic surface potential (Φ_0).

1.4 Second Harmonic Generation

Nonlinear spectroscopies such as sum frequency generation (SFG) and second harmonic generation (SHG) are noninvasive and nondestructive techniques which are highly sensitive to the

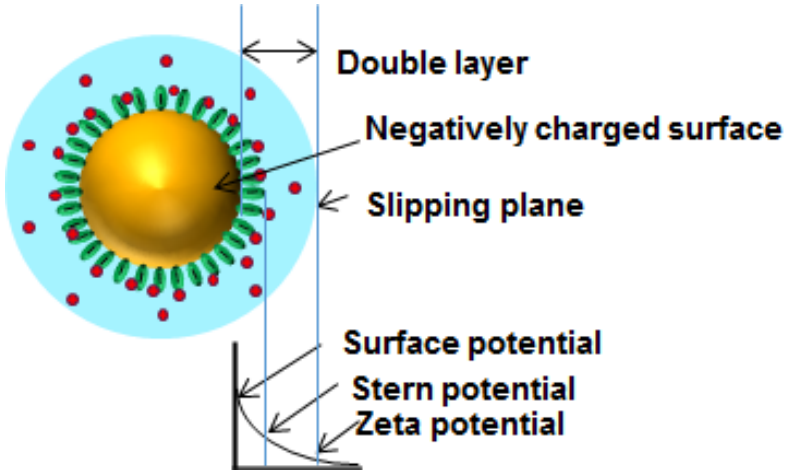

Figure 1.4. Schematic representation of the electrical double layer structure surrounding the surface of a colloidal nanoparticle with the corresponding electrostatic potential as a function of distance.

surface due to the optical symmetry of the measurement.[44-45] SHG is an optical process in which two incident photons of frequency ω add coherently to generate a photon of frequency 2ω.[44] SHG is typically forbidden in bulk media that have inversion symmetry but it can be generated at the surface of nanoparticles where the inversion symmetry is broken. The SHG signal from an interface has contributions from the second-order and third-order nonlinear susceptibilities, $\chi^{(2)}$ and $\chi^{(3)}$, respectively. The $\chi^{(2)}$ term originates from the two-photon spectroscopy of the surface, whereas the $\chi^{(3)}$ term is a consequence of the electric field of the surface inducing a polarization of bulk molecules in the solvent. The second harmonic electric field ($E_{2\omega}$) is given by equation (1.1),

$$E_{2\omega} \propto P_{2\omega} = \chi^{(2)} \mathrm{E}_{\omega} \mathrm{E}_{\omega} + \chi^{(3)} \mathrm{E}_{\omega} \mathrm{E}_{\omega} \phi_0 \qquad (1.1)$$

where, $\mathrm{P}_{2\omega}$ is the induced second-order polarization at the interface that generates second harmonic generation, E_{ω} is the electric field of the incident laser light and ϕ_0 is the surface potential due to the static electric field. The second-order polarization from the $\chi^{(2)}$ process, $\mathrm{P}_{2\omega}^{(2)}$, is equal to a summation of the density of adsorbed species ($\mathrm{N_i}$) and their second-order hyperpolarizabilities

($\alpha_i^{(2)}$), according to equation (1.2),

$$E_{2\omega}^{(2)} \propto P_{2\omega}^{(2)} = \chi^{(2)} E_\omega E_\omega = \sum_i^n N_i \langle \alpha_i^{(2)} \rangle E_\omega E_\omega \qquad (1.2)$$

Similarly, the second-order polarization from the $\chi^{(3)}$ process, $P_{2\omega}^{(3)}$, of a nanoparticle sample in aqueous colloidal suspension is associated with the interfacial water molecules and can be expressed using equation (1.3),

$$E_{2\omega}^{(3)} \propto P_{2\omega}^{(3)} = \chi^{(3)} E_\omega E_\omega \Phi_0 = N_{water} \left(\alpha_{water}^{(3)} + \frac{\mu \langle \alpha_{water}^{(2)} \rangle}{bkT} \right) E_\omega E_\omega \Phi_0 \qquad (1.3)$$

where, $\alpha_{water}^{(3)}$ is the third order hyperpolarizability of water, μ is the permanent dipole of water, b is a constant determined by the susceptibility element and kT is the thermal energy. The process of SHG is depicted schematically in Figure 1.5.

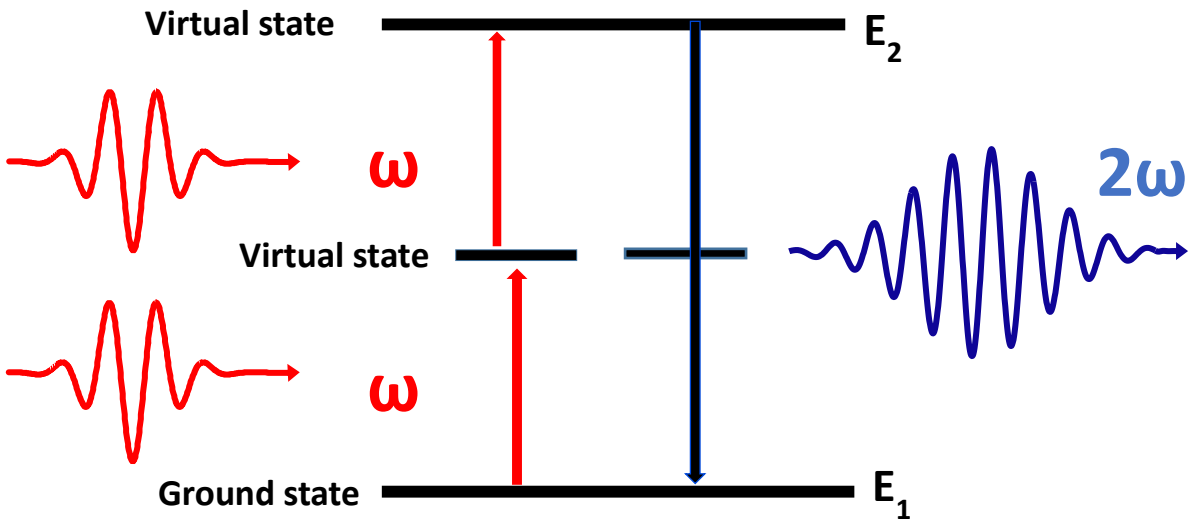

Figure 1.5. Schematic diagram showing the energy level diagram of second harmonic generation.

1.5 Scope of the Dissertation

This dissertation describes the use of the surface-sensitive nonlinear spectroscopy of second harmonic generation for the study of nanoparticles in colloidal suspension. Chapter 2 describes investigations of the surface charge density of the colloidal gold nanoparticles in water and their subsequent interactions with different salts measured as a function of added NaCl and

$MgCl_2$ solutions. Chapter 3 describes the dynamics of light-activated controlled release of the oligonucleotides from the miRNA-functionalized gold nanoparticles monitored as a function of the irradiation laser power and wavelengths. Light-activated drug delivery using biocompatible plasmonic nanoparticles presents a method with greater potential for spatiotemporally controlled release than alternate methods based on chemical stimuli, pH, or ionic strength. Plasmon-enhanced light-activated drug delivery systems are further studied using silver nanoparticles and the rate of photo-cleaving is compared with gold nanoparticles and polystyrene sulfate nanoparticles, as described in Chapter 4. In order to extend this photoactivated drug delivery to near infrared wavelengths that are better suited for the optical window of biological samples, novel colloidal gold-silver-gold core-shell-shell nanoparticles are prepared and characterized. These nanoparticles are functionalized with microRNA using Diels-Alder chemistry and the kinetics of the photothermal release of oligonucleotides is studied, as presented in Chapter 5. In addition to the SHG studies on plasmonic nanoparticles, the adsorption and transport of the drug-like molecule, malachite green dye, at the lipid bilayer in various liposomes in water are studied and described in Chapter 6. This work presented here is important for understanding stimuli responsive drug and gene delivery allowing for an unprecedented understanding of the surface chemistry of liposomes for future developments in drug delivery applications. Appendices A.1, A.2, and A.3 provide additional information corresponding to work presented in Chapters 2, 4, and 6, respectively. Overall, second harmonic generation is found to be a very sensitive technique to investigate the surface chemistry, surface charge density and molecular interactions at colloidal nanoparticle interfaces.

1.6 References

1. Mody, V. V.; Siwale, R.; Singh, A.; Mody, H. R. Introduction to metallic nanoparticles. *J. Pharm. Bioall. Sci.* **2010,** *2*, 282.

2. Eustis, S.; El-Sayed, M. A. Why Gold Nanoparticles are More Precious Than Pretty Gold: Noble Metal Surface Plasmon Resonance and its Enhancement of the Radiative and Nonradiative Properties of Nanocrystals of Different Shapes. *Chem. Soc. Rev.* **2006,** *35*, 209-217.

3. Chanana, M.; Liz-Marzan, L. M. Coating Matters: the Influence of Coating Materials on the Optical Properties of Gold Nanoparticles. *Nanophotonics* **2012,** *1*, 199-220.

4. Haber, L. H.; Kwok, S. J. J.; Semeraro, M.; Eisenthal, K. B. Probing the Colloidal Gold Nanoparticle/Aqueous Interface With Second Harmonic Generation. *Chem. Phys. Lett.* **2011,** *507*, 11-14.

5. Kamat, P. V. Photophysical, Photochemical and Photocatalytic Aspects of Metal Nanoparticles. *J. Phys. Chem. B* **2002,** *106*, 7729-7744.

6. Boisselier, E.; Astruc, D. Gold Nanoparticles in anomedicine: Preparations, Imaging, Diagnostics, Therapies and Toxicity. *Chem. Soc. Rev.* **2009,** *38*, 1759-1782.

7. Ghosh, P.; Han, G.; De, M.; Kim, C. K.; Rotello, V. M. Gold Nanoparticles in Delivery Applications. *Adv. Drug Deliv. Rev.* **2008,** *60*, 1307-1315.

8. Giljohann, D. A.; Seferos, D. S.; Daniel, W. L.; Massich, M. D.; Patel, P. C.; Mirkin, C. A. Gold Nanoparticles for Biology and Medicine. *Angew. Chem. Int. Ed.* **2010,** *49*, 3280-3294.

9. Skrabalak, S. E.; Chen, J.; Sun, Y.; Lu, X.; Au, L.; Cobley, C. M.; Xia, Y. Gold Nanocages: Synthesis, Properties, and Applications. *Acc. Chem. Res.* **2008,** *41*, 1587-1595.

10. Barhoumi, A.; Huschka, R.; Bardhan, R.; Knight, M. W.; Halas, N. J. Light-Induced Release of DNA From Plasmon-Resonant Nanoparticles: Towards Light-Controlled Gene Therapy. *Chem. Phys. Lett.* **2009,** *482*, 171-179.

11. Dreaden, E. C.; Alkilany, A. M.; Huang, X. H.; Murphy, C. J.; El-Sayed, M. A. The Golden Age: Gold Nanoparticles for Biomedicine. *Chem. Soc. Rev.* **2012,** *41*, 2740-2779.

12. Skrabalak, S. E.; Chen, J. Y.; Sun, Y. G.; Lu, X. M.; Au, L.; Cobley, C. M.; Xia, Y. N. Gold Nanocages: Synthesis, Properties, and Applications. *Acc. Chem. Res.* **2008,** *41*, 1587-1595.

13. Oldenburg, S. J.; Averitt, R. D.; Westcott, S. L.; Halas, N. J. Nanoengineering of Optical Resonances. *Chem. Phys. Lett.* **1998,** *288*, 243-247.

14. Ghosh Chaudhuri, R.; Paria, S. Core/shell nanoparticles: classes, properties, synthesis mechanisms, characterization, and applications. *Chem. Rev.* **2011,** *112* (4), 2373-2433.

15. Cao, Y.; Jin, R.; Mirkin, C. A. DNA-Modified Core− Shell Ag/Au Nanoparticles. *J. Am. Chem. Soc.* **2001,** *123,* 7961-7962.

16. Lim, D.-K.; Kim, I.-J.; Nam, J.-M. DNA-embedded Au/Ag core–shell nanoparticles. *Chem. Commun.* **2008,** 42, 5312-5314.

17. Zhong, C.-J.; Maye, M. M. Core–shell assembled nanoparticles as catalysts. *Adv. Mater.* **2001,** *13*, 1507-1511.

18. Jackson, J.; Halas, N. Silver nanoshells: variations in morphologies and optical properties. *J. Phys. Chem. B* **2001,** *105*, 2743-2746.

19. Karam, T. E.; Smith, H. T.; Haber, L. H. Enhanced Photothermal Effects and Excited-State Dynamics of Plasmonic Size-Controlled Gold–Silver–Gold Core–Shell–Shell Nanoparticles. *J. Phys. Chem. C* **2015,** *119*, 18573-18580.

20. Olson, J.; Dominguez-Medina, S.; Hoggard, A.; Wang, L.-Y.; Chang, W.-S.; Link, S. Optical characterization of single plasmonic nanoparticles. *Chem. Soc. Rev.* **2015,** *44*, 40-57.

21. El-Sayed, I. H.; Huang, X.; El-Sayed, M. A. Surface plasmon resonance scattering and absorption of anti-EGFR antibody conjugated gold nanoparticles in cancer diagnostics: applications in oral cancer. *Nano Lett.* **2005,** *5*, 829-834.

22. Jensen, T. R.; Malinsky, M. D.; Haynes, C. L.; Van Duyne, R. P. Nanosphere lithography: tunable localized surface plasmon resonance spectra of silver nanoparticles. *J. Phys. Chem. B* **2000,** *104*, 10549-10556.

23. Pattnaik, P. Surface plasmon resonance. *App. Biochem. Biotech.* **2005,** *126*, 79-92.

24. Homola, J.; Yee, S. S.; Gauglitz, G. Surface plasmon resonance sensors: review. *Sensors and Actuators B: Chemical* **1999,** *54*, 3-15.

25. Nikoobakht, B.; Wang, J.; El-Sayed, M. A. Surface-enhanced Raman scattering of molecules adsorbed on gold nanorods: off-surface plasmon resonance condition. *Chem. Phys. Lett.* **2002,** *366*, 17-23.

26. Alvarez-Puebla, R.; Cui, B.; Bravo-Vasquez, J.-P.; Veres, T.; Fenniri, H. Nanoimprinted SERS-active substrates with tunable surface plasmon resonances. *J. Phys. Chem. C* **2007,** *111*, 6720-6723.

27. Nie, S.; Emory, S. R. Probing single molecules and single nanoparticles by surface-enhanced Raman scattering. *Science* **1997,** *275*, 1102-1106.

28. Meyer, S. A.; Le Ru, E. C.; Etchegoin, P. G. Combining surface plasmon resonance (SPR) spectroscopy with surface-enhanced Raman scattering (SERS). *Anal. Chem.* **2011,** *83*, 2337-2344.

29. Hu, M.; Chen, J.; Li, Z.-Y.; Au, L.; Hartland, G. V.; Li, X.; Marquez, M.; Xia, Y. Gold nanostructures: engineering their plasmonic properties for biomedical applications. *Chem. Soc. Rev.* **2006,** *35*, 1084-1094.

30. Englebienne, P.; Hoonacker, A. V.; Verhas, M. Surface plasmon resonance: principles, methods and applications in biomedical sciences. *J. Spec.* **2003,** *17*, 255-273.

31. Liao, H.; Nehl, C. L.; Hafner, J. H. Biomedical applications of plasmon resonant metal nanoparticles. *Future med.* **2006**, 1, 201-208.

32. Mayer, K. M.; Hafner, J. H. Localized surface plasmon resonance sensors. *Chem. Rev.* **2011,** *111*, 3828-3857.

33. Willets, K. A.; Van Duyne, R. P. Localized surface plasmon resonance spectroscopy and sensing. *Annu. Rev. Phys. Chem.* **2007,** *58*, 267-297.

34. Haes, A. J.; Hall, W. P.; Chang, L.; Klein, W. L.; Van Duyne, R. P. A localized surface plasmon resonance biosensor: First steps toward an assay for Alzheimer's disease. *Nano Lett.* **2004,** *4*, 1029-1034.

35. McFarland, A. D.; Van Duyne, R. P. Single silver nanoparticles as real-time optical sensors with zeptomole sensitivity. *Nano Lett.* **2003,** *3*, 1057-1062.

36. Yonzon, C. R.; Jeoung, E.; Zou, S.; Schatz, G. C.; Mrksich, M.; Van Duyne, R. P. A comparative analysis of localized and propagating surface plasmon resonance sensors: the binding of concanavalin A to a monosaccharide functionalized self-assembled monolayer. *J. Am. Chem. Soc.* **2004,** *126*, 12669-12676.

37. Homola, J. Surface plasmon resonance sensors for detection of chemical and biological species. *Chem. Rev.* **2008,** *108*, 462-493.

38. Eustis, S.; El-Sayed, M. A. Why gold nanoparticles are more precious than pretty gold: noble metal surface plasmon resonance and its enhancement of the radiative and nonradiative properties of nanocrystals of different shapes. *Chem. Soc. Rev.* **2006,** *35*, 209-217.

39. Hou, W.; Cronin, S. B. A review of surface plasmon resonance-enhanced photocatalysis. *Advanced Functional Materials* **2013,** *23* (13), 1612-1619.

40. Ghosh, S. K.; Pal, T. Interparticle coupling effect on the surface plasmon resonance of gold nanoparticles: from theory to applications. *Chem. Rev.* **2007,** *107*, 4797-4862.

41. Hutter, E.; Fendler, J. H. Exploitation of localized surface plasmon resonance. *Adv. Mater.* **2004,** *16*, 1685-1706.

42. Jen, S.-H.; Dai, H.-L.; Gonella, G. The Effect of Particle Size in Second Harmonic Generation From the Surface of Spherical Colloidal Particles. II: The Nonlinear Rayleigh−Gans−Debye Model. *J. Phys. Chem. C* **2010,** *114*, 4302-4308.

43. Gonella, G.; Gan, W.; Xu, B.; Dai, H.-L. The Effect of Composition, Morphology, and Susceptibility on Nonlinear Light Scattering From Metallic and Dielectric Nanoparticles. *J. Phys. Chem. Lett.* **2012,** *3*, 2877-2881.

44. Boyd, R. W. *Nonlinear Optics*. 3rd ed.; Academic Press: New York, USA, 2003.

45. Yan, E. C. Y.; Liu, Y.; Eisenthal, K. B. New Method for Determination of Surface Potential of Microscopic Particles by Second Harmonic Generation. *J. Phys. Chem. B* **1998,** *102*, 6331-6336.

CHAPTER 2
DETERMINATION OF THE SURFACE CHARGE DENSITY OF COLLOIDAL GOLD NANOPARTICLES USING SECONDHARMONIC GENERATION*

2.1 Introduction

Gold nanoparticles have attracted considerable attention due to their unique physical, chemical, and optical properties,[1-3] making them well suited for many biological applications such as molecular sensing,[4,5] labeling,[6,7] drug delivery,[8-10] and photothermal cancer therapy.[11-14] Gold nanoparticles have localized surface plasmon resonances, which are characterized by the coherent oscillations of free elections under incident light and depend on the nanoparticle size, shape, composition, and surrounding medium.[1-3] The plasmon resonances can cause significant optical field enhancements leading to processes such as surface enhanced Raman spectroscopy (SERS),[15,16] surface enhanced fluorescence,[17-19] and plasmon-exciton polariton resonant coupling.[20,21] Functionalization of gold nanoparticles with biologically-relevant molecules such as proteins, DNA, and pharmaceuticals is readily accessible through thiolation.[2,22] In order to develop and optimize potential applications of gold nanoparticles, it is important to more fully understand the surface chemistry and surface charge density of colloidal gold nanoparticles in water.

Second harmonic generation (SHG) is a powerful, noninvasive, surface-sensitive technique that is useful for the investigation of colloidal nanoparticles.[21,23-28] SHG is a nonlinear optical process in which two incident photons of frequency ω add coherently to generate a photon of frequency 2ω.[29-31] SHG is typically forbidden in bulk media that have inversion symmetry but it can be generated at the surface of nanoparticles where the inversion symmetry is broken. The SHG

signal from an interface has contributions from the second-order and third-order nonlinear susceptibilities, $\chi^{(2)}$ and $\chi^{(3)}$, respectively.[23,32-34] The $\chi^{(2)}$ term originates from the two-photon spectroscopy of the surface, whereas the $\chi^{(3)}$ term is a consequence of the electric field of the surface inducing a polarization of bulk molecules in the solvent. The surface charge density and the electrostatic surface potential of colloidal nanoparticles can be obtained by fitting experimental SHG measurements as a function of added electrolyte concentrations to theoretical models, such as the Gouy-Chapman model.[33-36] Several different colloidal nanoparticle samples have been investigated using this SHG $\chi^{(3)}$ method, also called the electric field induced second harmonic (EFISH) technique, including polystyrene nanoparticles,[32,34,37,38] clay nanodisks,[23,39] liposomes,[40] and biologically conjugated nanoparticles.[41] Additional $\chi^{(3)}$ studies have been conducted on planar interfaces including electrolytes near solid/water interfaces,[33,42,43] DNA at surfaces in solution[44-46] and hot electron transfer dynamics from colloidal lead selenide nanocrystals to a titanium oxide surface.[47] For colloidal particles with nanoscale size, consideration of the surface curvature is crucial for an accurate determination of the surface charge density and the electrostatic surface potential, especially in the limit where the Gouy-Chapman model is no longer valid.[36,48-50]

Existing techniques for obtaining the electrostatic surface potential of colloids based on electrophoretic mobility measurements are challenging due to the lack of information regarding the surface structure and its interaction with the solution.[35,51] For example, problems can arise from accurately accounting for the position of the slipping plane, the double layer distortion, the viscoelectric constant of the solution, and the electroosmosis effect.[35,51] The relationship between the colloidal surface potential and the corresponding surface charge density depends on several interconnected factors including the nanoparticle size and electrolyte adsorption to the Stern-layer interface.[35,36,49,50] Previous investigations using electrophoretic mobility measurements on

colloidal gold nanoparticles[49,50] have several inherent experimental limitations and may not correctly account for effects due to nanoparticle aggregation. The direct comparison between results obtained by the SHG $\chi^{(3)}$ method and electrophoretic mobility measurements with careful considerations of nanoparticle size and ion adsorption can provide for the most accurate determination of the surface charge density of colloidal nanoparticles.

In this chapter, second harmonic generation measurements are used to determine the surface charge density of 50 nm colloidal gold nanoparticles functionalized with mercaptosuccinic acid (MSA) in water. The SHG signal is measured as a function of added NaCl and $MgCl_2$ electrolyte concentrations and the results are fit to numerical solutions to the Poisson-Boltzmann equation to account for the nanoparticle surface curvature, the different salts valences, and ion adsorption, with excellent agreement to corresponding electrophoretic mobility measurements. To the best of our knowledge, this is the first time the SHG $\chi^{(3)}$ technique has been successfully integrated with numerical solutions that account for corrections due to the colloidal nanoparticle surface curvature. The findings indicate that a significant Stern layer of counterions is present at the nanoparticle surface and is an important contribution for understanding the surface chemistry of colloidal gold nanoparticles in water.

2.2 Experimental Section

2.2.1 Synthesis and Characterization of Nanoparticles: The colloidal gold nanoparticle sample is prepared using a technique described previously, which includes seeded growth, thiolation, and dialysis.[21,52] In the gold nanoparticle seed synthesis, 900 μL of 34 mM sodium citrate is added to 30 mL of 290 μM gold chloride in ultrapure water under boiling conditions and vigorous stirring. The solution changes color to a bright red after 10 minutes and is then cooled to room temperature. In a separate flask, 250 μL of the seed solution is added to 2.9 mM of gold chloride in 9.8 mL of

ultrapure water, followed by the addition of 100 μL of 0.03 M hydroquinone and 22 μL of 34 mM sodium citrate. The solution is left to stir at room temperature for 60 min to produce the 50 nm colloidal gold nanoparticles.[21,52] This synthesis procedure is repeated several times until a sufficient sample volume is prepared. The colloidal gold nanoparticles are then dialyzed against a 22 mM solution of MSA in ultrapure water for three consecutive days, followed by dialysis against ultrapure water for two additional days, where the outer solution or water is replaced several times a day. The MSA replaces the citrate as the capping agent due to the relatively strong gold-thiol bond. The final dialysis in ultrapure water removes excess salts and reactants from the gold nanoparticle solution.

The gold nanoparticles are characterized using transmission electron microscopy (TEM), dynamic light scattering, ultraviolet-visible extinction spectroscopy, and zeta potential measurements. A representative TEM image of the gold nanoparticle sample is shown in Figure 2.1. From a survey of 190 TEM images, the average nanoparticle size is determined to be 50 ± 6 nm in diameter. Figure 2.2 displays the experimental extinction spectrum of the colloidal gold nanoparticle sample (red line) compared to the spectrum derived using Mie theory[25] for 50 ± 6 nm gold nanoparticles in water (grey line) at a concentration of 2.9×10^9 nanoparticles per mL, showing good agreement. The localized surface plasmon peak is observed at 534 nm. Dynamic light scattering measurements of the nanoparticle sample give a hydrodynamic diameter of 50.5 ± 9.6 nm, in agreement with the TEM and extinction spectroscopy results. The zeta potential ζ of the colloidal gold nanoparticle sample is obtained from electrophoretic mobility measurements using a Malvern Zetasizer (ZEN 3600). The electrophoretic mobility plot showing the average of measurements and the experimental uncertainty is displayed in Figure 2.3. The relationship between the zeta potential and the electrophoretic motility is given by $U_E = 2\,\varepsilon\,\zeta\,f(\kappa a)\,/\,3\eta$

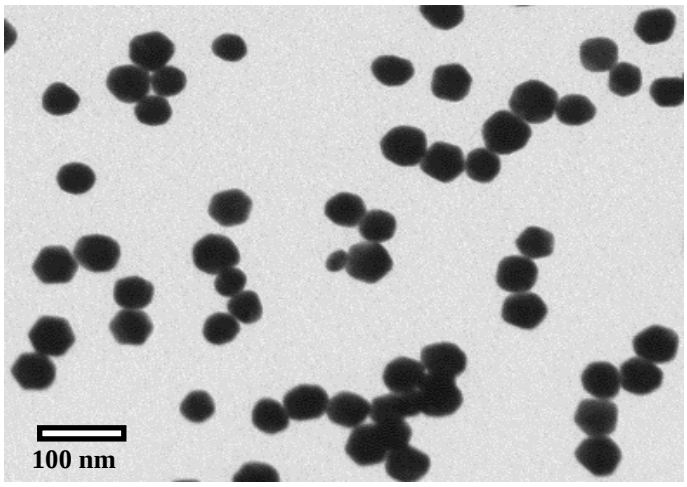

Figure 2.1. Transmission electron microscopy image of the gold nanoparticle sample. The nanoparticle diameter is determined to be 50 ± 6 nm from a survey of 190 mages.

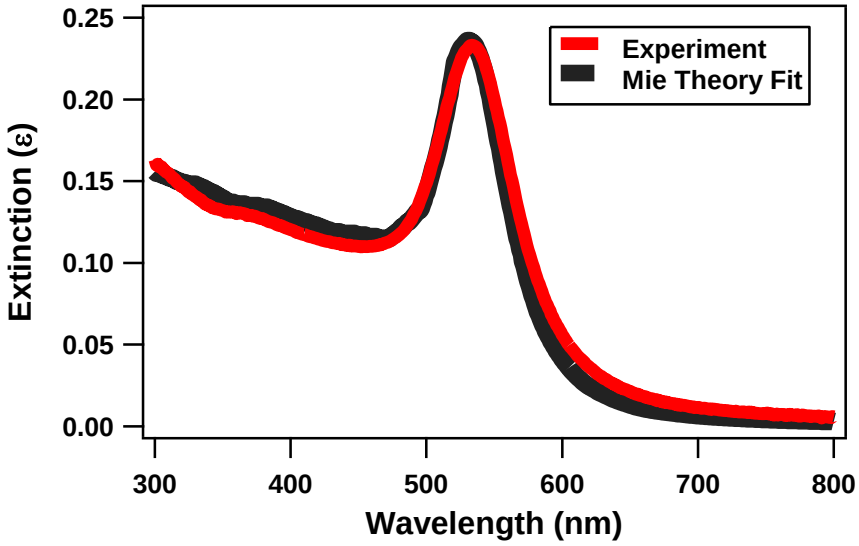

Figure 2.2. Extinction spectrum of the 50 nm colloidal gold nanoparticle sample in water (red line) compared with the best fit from Mie theory (grey line). The concentration is calculated to be 2.9 x 10^9 nanoparticles/mL.

where, U_E is the electrophoretic mobility, ε is the dielectric constant of the bulk solution, η is the coefficient of viscosity of the solvent, $f(\kappa a)$ is Henry's function, κ is the inverse of the Debye length, and a is the nanoparticle radius. For $\kappa a \ll 1$, Huckel's approximation gives $f(\kappa a) = 1$.[50,53] For our experimental conditions, before adding any salts, $\kappa a \ll 1$, so Huckel's approximation is used. For the colloidal gold nanoparticle sample in water, with a diameter of 50 ± 6 nm, the average

electrophoretic mobility is measured to be −2.96 ± 0.89 μm cm/Vs, giving a zeta potential of −57 ± 17 mV.

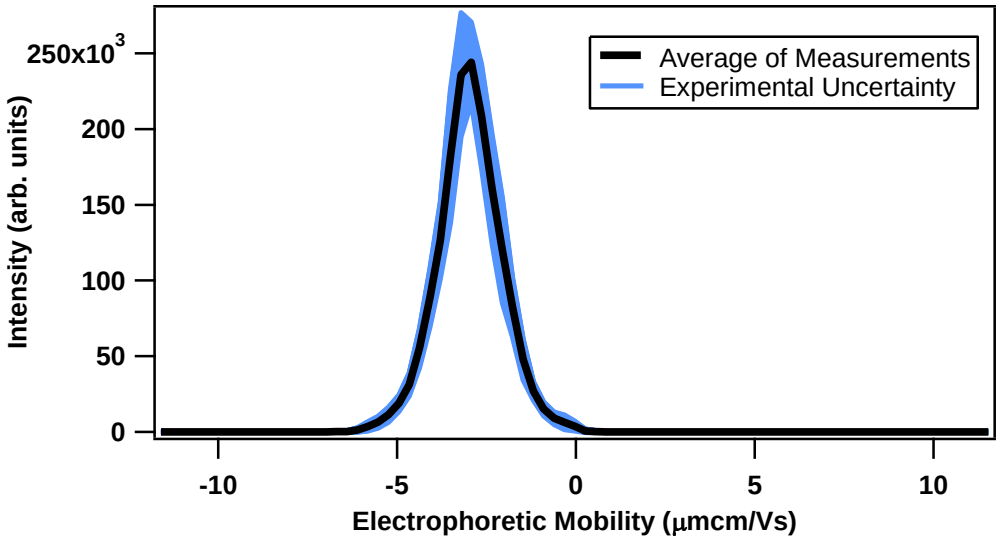

Figure 2.3. Electrophoretic mobility plot showing the average of measurements (black line) and the experimental uncertainty (blue error bars).

2.2.2 Experimental Setup: The experimental setup for the second harmonic generation studies has been described previously.[21,25] Briefly, the setup consists of an ultrafast laser system, an optical setup, and a high-sensitivity charge-coupled device spectroscopy detector connected to a monochromator-spectrograph. A titanium:sapphire oscillator laser with 2.6 W average power and 70 fs pulses centered at 800 nm with a repetition rate of 80 MHz is attenuated to 1.2 W and is focused to the gold nanoparticle sample at an initial concentration of 4.4 x 10^9 nanoparticles per mL in a 1 cm quartz cuvette. Optical filters are used to remove any residual SHG signal from the laser beam before hitting the sample and to remove the fundamental 800 nm light after the sample. The SHG signal is acquired in the forward direction from the nanoparticle sample. An integrated computer program controls a beam block, a magnetic stir bar, and a burette to add the salt solutions to the sample under stirring in synchronization with automated data acquisition for background-subtracted concentration-dependent SHG measurements. Multiple spectra are acquired with 1

second acquisitions for the laser blocked and unblocked for 1 minute for each salt concentration for statistical analysis.

2.3 Results and Discussion

The background-subtracted concentration-dependent SHG spectra are analyzed in order to obtain the SHG electric field as a function of the added salt concentration for both NaCl and $MgCl_2$. Representative SHG spectra of colloidal gold nanoparticles with added NaCl and $MgCl_2$ are shown in Figures 2.4 (a) and (b), respectively. The large SHG peak is centered at 400 nm and has a full width half maximum of 4.5 nm. The rise in intensity at longer wavelengths is attributed to two-photon fluorescence from the colloidal gold nanoparticles. The SHG signal is observed to decrease with added salt concentrations due, in part, to the changing electrostatic potential at the gold nanoparticle surface and the corresponding $\chi^{(3)}$ effect. The SHG electric field E_{SHG} is proportional to the square root of the SHG signal, where

$$E_{SHG} = A + B\Phi_0. \tag{2.1}$$

Here, A and B are constants that include the second-order and third-order nonlinear susceptibilities, $\chi^{(2)}$ and $\chi^{(3)}$, respectively, as well as the incident electric field E_ω from the laser at frequency ω. As the electrolyte concentration is increased, the ions distribute around the charged surface and screen the electrostatic potential Φ_0 at the nanoparticle surface to decrease its magnitude, which leads to a decrease in the measured SHG signal.

In order to distinguish between the SHG decrease from the $\chi^{(3)}$ effect with the SHG decrease due to nanoparticle dilution, the results are compared to a control where ultrapure water is added to the nanoparticle sample instead of the salt solutions. The SHG signal from the sample at different concentrations is obtained by integrating the background-subtracted spectrum over the wavelength range from 395 and 405 nm and subtracting a two-photon fluorescence linear offset

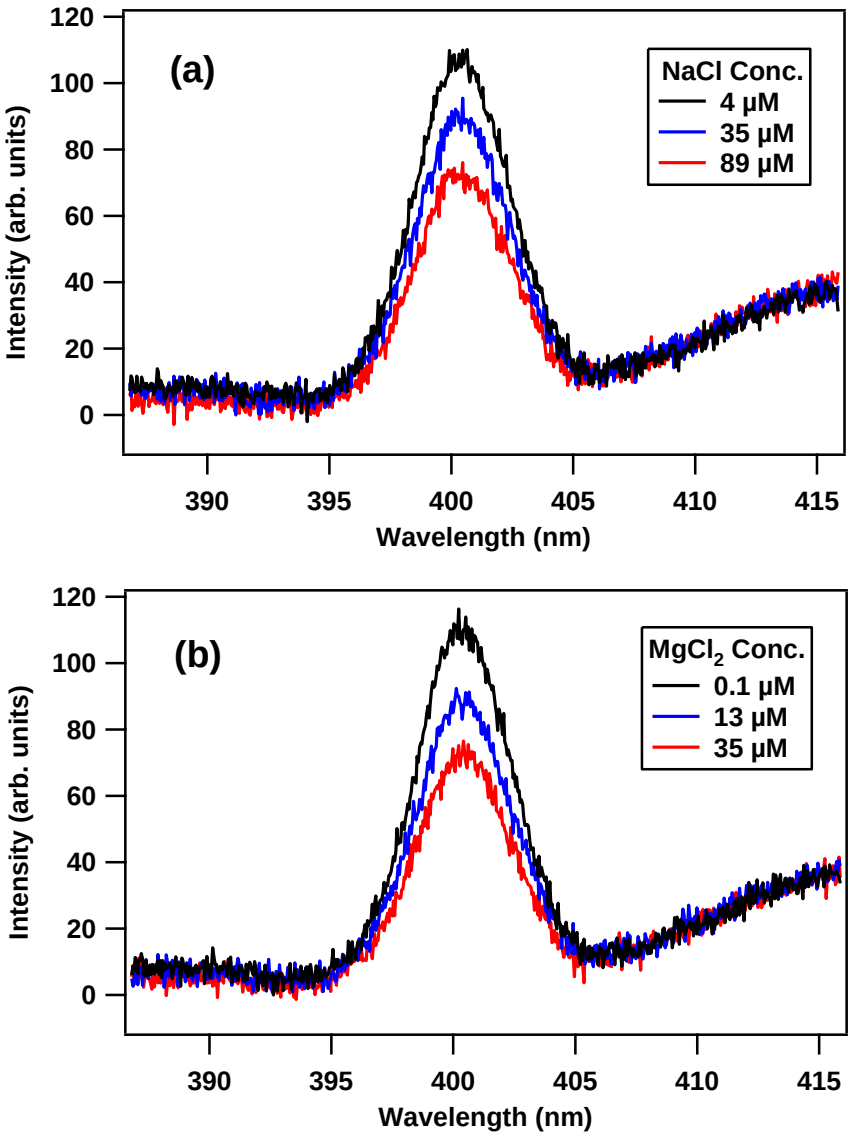

Figure 2.4. SHG spectra of the colloidal gold nanoparticle sample at different (a) NaCl and (b) $MgCl_2$ concentrations using 800 nm incident light.

connecting the spectra from 394 to 395 nm and 405 to 406 nm using a linear least squares fit. The background-corrected SHG signal of the gold nanoparticle sample as a function of the added volume of water, 0.25 mM NaCl, and 0.10 mM of $MgCl_2$ is shown in Figure 2.5. Error bars represent the standard deviation of the SHG signal. The SHG signal is observed to decrease when adding water alone due to nanoparticle dilution. The SHG signal is observed to decrease much more, especially at first, when adding the NaCl and $MgCl_2$ solutions due to a combination of

nanoparticle dilution and the $\chi^{(3)}$ effect. When adding water to the gold nanoparticle sample, the SHG signal is observed to vary linearly with the nanoparticle concentration, as expected for this concentration range. Figure 2.6 shows these results, with the best fit (red line) given by a slope of (1.72 ± 0.02) x 10^{-10} mL/nanoparticle and a y-intercept of 0.246 ± 0.008 in arbitrary units where the SHG signal is normalized for the initial sample concentration. The non-zero y-intercept is due to SHG signal from water alone in the quartz cuvette. The corrected SHG signal due the $\chi^{(3)}$ effect is determined by dividing the measured SHG signal as a function of the added salt solution volume by the linear decrease obtained from the added water measurements. The square root of the corrected SHG signal is denoted as the SHG electric field E_{SHG}, which is used to compare to theoretical model best fits. Complementary SHG and extinction spectroscopy measurements of the gold nanoparticle sample as a function of higher salt concentrations are shown in Appendix 1 and demonstrate that nanoparticle aggregation and plasmonic spectral shifts do not occur in the concentration range studied in Figures 2.4, 2.5, and 2.7.[54] The SHG signal is observed to increase significantly for nanoparticle aggregation, in contrast to the decrease in SHG signal from the $\chi^{(3)}$ effect, measured here.

The surface charge density and the electrostatic surface potential of the colloidal gold nanoparticles capped with MSA is obtained by fitting the concentration-dependent experimental measurements of E_{SHG} to three different models. The first model is the Gouy-Chapman model,[34,35] which is expected to be extremely inaccurate for the nanoparticle sizes studied here. The second and third models use numerical solutions to the spherical Poisson-Boltzmann equation,[34-36,48] and either neglect ion adsorption or include ion adsorption, respectively. The Poisson-Boltzmann is given by

$$\nabla^2\Phi = -\frac{eN_A}{\varepsilon}\sum_i C_i z_i \, e^{-z_i e\Phi/kT} \qquad (2.2)$$

where Φ is the electrostatic potential as a function of the distance from the surface, e is the

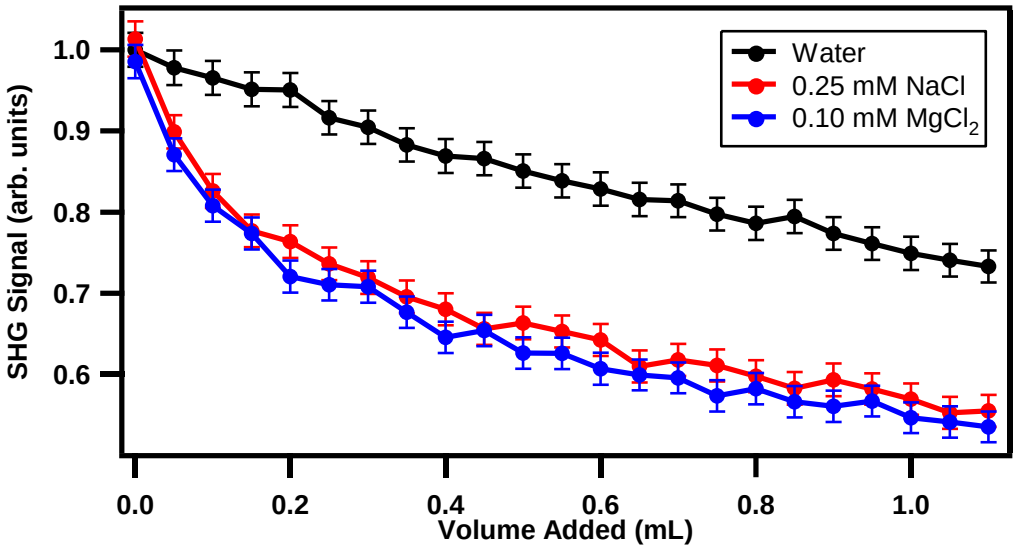

Figure 2.5. The SHG signal of the gold nanoparticle sample as a function of the added volume of ultrapure water (black line), 0.25 mM NaCl (red line), and 0.10 mM $MgCl_2$ (blue line).

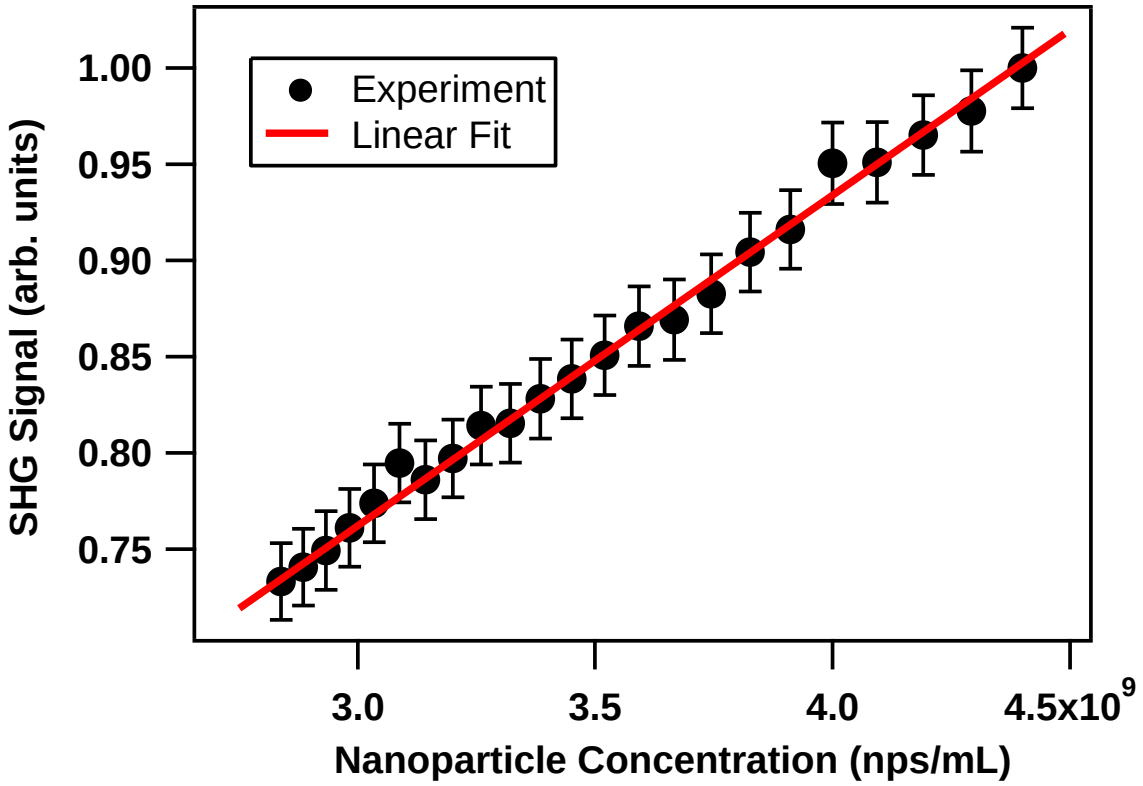

Figure 2.6. The SHG signal intensity as a function of the concentration of the gold nanoparticle sample in water.

elementary charge, N_A is the Avogadro constant, C_i is the bulk electrolyte concentration of the i^{th} ion, z_i is the charge of the i^{th} ion, k is the Boltzmann constant, and T is the temperature. The Gouy-Chapman model is the analytical solution to the Poisson-Boltzmann equation for describing the distributions of ions near a planar, charged surface in a symmetric electrolyte solution. The surface potential, according to the Gouy-Chapman model, is given by

$$\Phi_0 = \frac{2kT}{ze}\sinh^{-1}\left(\frac{\sigma}{\sqrt{8\varepsilon kTC}}\right) \tag{2.3}$$

where σ is the surface charge density in SI units, and C is the salt concentration. NaCl is a symmetric electrolyte with $z = 1$. $MgCl_2$ is an asymmetric electrolyte so the GC model is an inaccurate description of the electrostatic surface potential under varying $MgCl_2$ concentration, especially under certain conditions. For a negatively-charged planar surface at relatively low concentrations, the Mg^{2+} ion dominates the interaction and the GC equation with $z = 2$ is sufficiently accurate for modeling the surface potential in the $MgCl_2$ electrolyte solution. However, for nanoparticles smaller than about 100 nm, the significant surface curvature requires a numerical solution to the Poisson-Boltzmann equation in spherical coordinates in order to accurately determine the relationship between the surface charge density and the electrostatic surface potential in an electrolyte.[49,50] In addition, ion adsorption to the colloidal nanoparticle surface can be included by expressing the surface charge density as the sum of the initial surface charge density σ_0 and the charge density created by adsorbed ions, given by[33,55]

$$\sigma = \sigma_0 + \sigma_m\left(\frac{K_m\,C}{1+K_m\,C}\right) \tag{2.4}$$

where σ_m is the maximum surface charge density due to adsorbed ions m at saturation and K_m is equilibrium constant of ion adsorption. In this case, the surface potential corresponds to the outer edge of the Stern layer, including the adsorbed ions.

The three different models are applied to fit the experimental E_{SHG} measurements of the gold nanoparticle sample under varying NaCl and $MgCl_2$ concentrations. Since the data are taken under the same laser and nanoparticle sample conditions, the values for A, B, and σ from equation (1) are expected to remain constant for both the NaCl and $MgCl_2$ concentration-dependent measurements for each separate fit. The experimental results of the SHG electric field measurements with the corresponding fits as a function of NaCl and $MgCl_2$ concentrations are shown in Figure 2.7. The first fit uses equation (3) from the Gouy-Chapman model for $z = 1$ for NaCl and $z = 2$ for $MgCl_2$ resulting in the green curves for Figures 2.7 (a) and (b), with A, B, and σ given by 0.810 ± 0.004, -2.11 ± 0.08 V^{-1}, and (-6.08 ± 0.57) x 10^{-4} C/m^2, respectively. However, it is important to point out again that the Gouy-Chapman model is not expected to be valid for the nanoparticle size and salt concentrations in these studies. The second fit incorporates numerical calculations for the Poisson-Boltzmann equation and neglects ion adsorption. The numerical calculations include effects from the nanoparticle surface curvature and the symmetric and asymmetric NaCl and $MgCl_2$ electrolytes. More details about the procedure used for the numerical solutions to the spherical Poisson-Boltzmann equation and the corresponding fits are described in Appendix 1. The second fit using the numerical solutions to the Poisson-Boltzmann equation without including ion adsorption is shown by the red curves in Figures 2.7 (a) and (b), with A, B, and σ given by 0.659 ± 0.008, -7.49 ± 0.25 V^{-1}, and (-1.36 ± 0.12) x 10^{-3} C/m^2, respectively. The third fit using the numerical solutions to the Poisson- Boltzmann equation including ion adsorption is shown by the black curves in Figures 2.7 (a) and (b), with A, B, and σ_0 given by 0.706 ± 0.009, -4.59 ± 0.16 V^{-1}, and (-1.95 ± 0.12) x 10^{-3} C/m^2, respectively, with the ion adsorption surface densities and equilibrium constants given by 2.6 ± 0.5 x 10^{-4} C/m^2 and 0.18 μM^{-1}, respectively, for the sodium ion, and 1.3 ± 0.5 x 10^{-4} C/m^2 and 11 μM^{-1}, respectively, for the magnesium ion. The

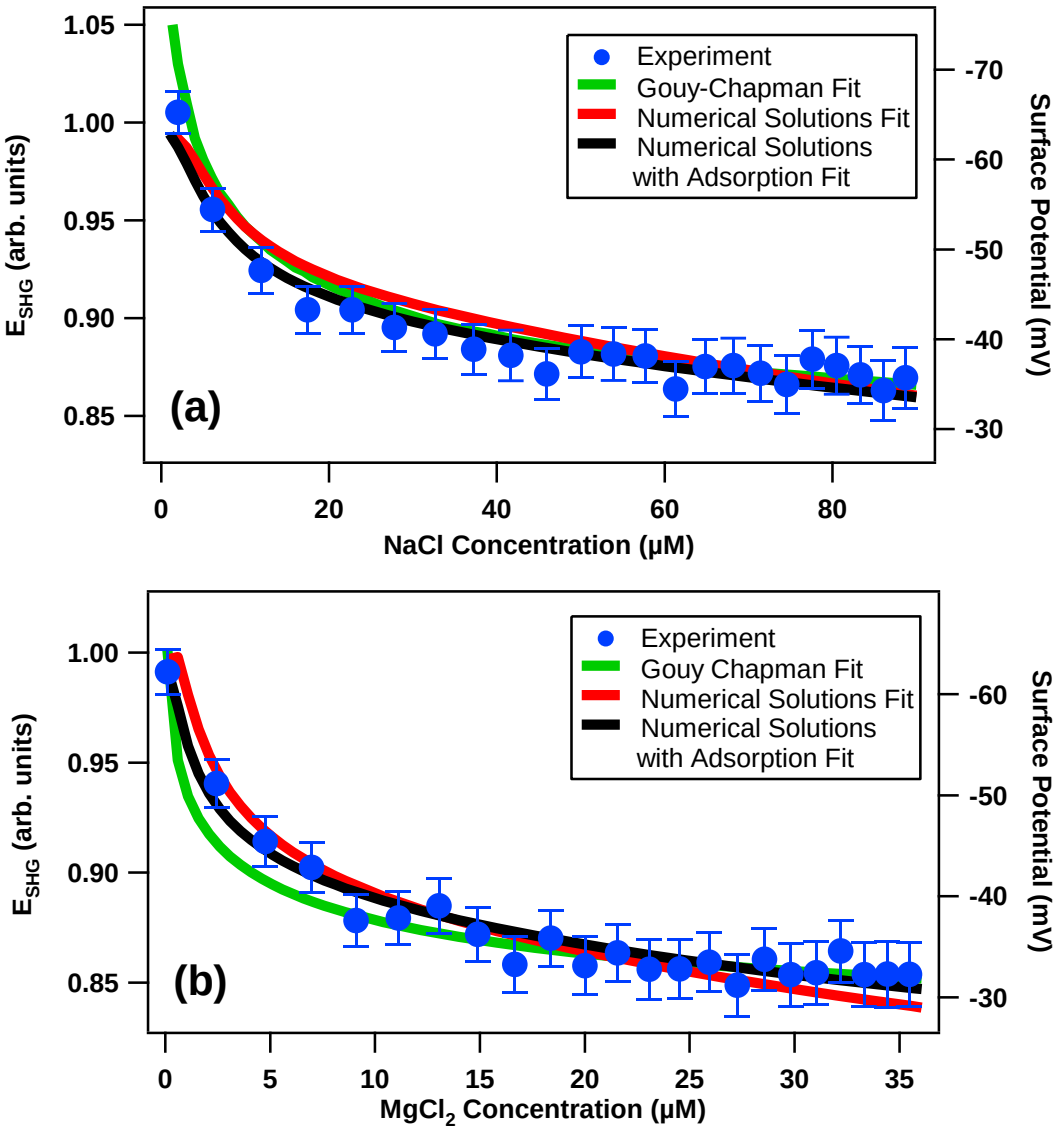

Figure 2.7. Experimental measurements of the SHG electric field (blue circles) as a function of added (a) NaCl and (b) $MgCl_2$ salt concentrations for the colloidal gold nanoparticle sample with corresponding fits using the Gouy-Chapman model (green curves) and numerical solutions to the Poisson-Boltzmann equation without ion adsorption (red curves) and with ion adsorption (black curves).

The fitting results are summarized in Table 1.1. The third fit, using the numerical solutions including ion adsorption, provides the best accuracy to the experimental results, giving an overall R^2 value of 0.95, compared to R^2 values of 0.92 and 0.90 for the first and second fits, respectively. Accordingly, the adjusted $\bar{R}^2$ values are 0.92, 0.90, and 0.94 for the first, second, and third fits, respectively, showing that the third fit is still the most accurate model when considering the

different number of fitting parameters.

The corresponding surface potentials from the best fit using numerical solutions to the spherical Poisson-Boltzmann equation including ion adsorption are labeled on the right-side y-axes of Figures 2.7 (a) and (b). The surface potentials before the addition of salts from this best fit are determined to be −65 ± 2 mV and −62 ± 2 mV for the NaCl and $MgCl_2$ datasets, respectively. In comparison, the corresponding surface potentials from the other fits before the addition of salts are −46 ± 2 mV and −42 ± 2 mV for the NaCl and $MgCl_2$ datasets using the numerical solutions fit without including adsorption, respectively, and −93 ± 6 mV and −86 ± 6 mV for the NaCl and $MgCl_2$ datasets using the Gouy-Chapman fit, respectively. In addition, the low electrolyte concentrations studied here lead to large Debye lengths, so the zeta potential is not expected to deviate by more than about 5% from the surface potential before adding salt, since electroviscosity effects can be neglected and the distance from the surface to the slipping plane can be estimated to be about 1 nm.[56, 57] The zeta potential of the gold nanoparticles obtained from the electrophoretic mobility measurements shown in Figure 2.3 agrees best with the initial surface potentials determined from the numerical solutions including adsorption, further confirming the accuracy of this model. Taking these considerations into account, the σ value of $(-1.95 \pm 0.12) \times 10^{-3}$ C/m^2, obtained from numerical solutions to the Poisson-Boltzmann equation including ion adsorption, is expected to represent the most accurate determination of the surface charge density of this gold nanoparticle sample in water. This corresponds to a total charge of $(-1.53 \pm 0.09) \times 10^{-17}$ C or −95.6 ± 5.9 charges per nanoparticle.

The ion adsorption surface densities and equilibrium constants obtained from the best fit provide interesting insight into the nature of the colloidal gold nanoparticle surface. The higher ion adsorption surface charge density of the sodium ion compared to the magnesium ion can be

Table 2.1. Summary of the fitting results of A, B, and σ for the three models. The resulting initial surface potentials before adding salts are also tabulated.

Models	Fit Parameters			Initial Surface Potential (mV)	
	A	B (V^{-1})	σ (C/m^2)	NaCl	$MgCl_2$
Gouy-Chapman	0.810 ± 0.004	–2.11 ± 0.08	(–6.08 ± 0.57) × 10^{-4}	–93 ± 6	–86 ± 6
Numerical Solutions	0.659 ± 0.008	–7.49 ± 0.25	(–1.36 ± 0.12) × 10^{-3}	–46 ± 2	–42 ± 2
Numerical Solutions with Adsorption	0.706 ± 0.009	–4.59 ± 0.16	(–1.95 ± 0.12) × 10^{-3}	–65 ± 2	–62 ± 2

explained predominantly by the different values of the free energy of solvation, where the Na^+ ion has a solvation free energy of −375 kJ/mol in water and the Mg has a solvation free energy of −1838 kJ/mol.[58] The larger ion adsorption equilibrium constant of magnesium compared to sodium can be explained by the different valences of the ions. Additional factors such as ion polarizabilities, adsorbate-adsorbate repulsions, and image-charge attraction probably also influence these results.

These experimental results provide an important description of the colloidal gold nanoparticle interface. The results indicate that ion adsorption is important at the colloidal gold nanoparticle interface in water. Additionally, previous studies estimate the average area of MSA to be 15 A^2 in a self-assembled monolayer (SAM).[49, 59] The nanoparticles are expected to be covered by a full monolayer of MSA since the nanoparticles are prepared by dialysis in an MSA solution in significant excess of the concentration needed to saturate the gold surface, although additional studies should be done to confirm this. The first and second acid dissociation constants for MSA in water are given by pK_{a1} = 4.19 and pK_{a2} = 5.64.[49] The pH of the gold nanoparticle sample is measured to be 6.0 ± 0.2. Therefore, assuming full coverage, each MSA molecule would have an average charge of $-1.7 \pm 0.1\ e$, assuming the acid dissociation constants are the same

when the molecule is attached to the gold nanoparticle surface. Using the expected MSA molecular density from SAM studies, this would correspond to a surface charge density of −1.7 C/m^2. The significant discrepancy between this estimated surface charge density and the measured value using the $\chi^{(3)}$ method can be explained by several factors. The pK_a of MSA is likely to be very different at the nanoparticle surface than in bulk water, leading to a lower surface charge density. The MSA may not form a full monolayer at the nanoparticle surface. Gold atoms near the surface may be positively charged, offsetting the total charge of the nanoparticle. Additionally, adsorbed counterions may be present on the gold nanoparticle surface even before adding any salt concentration. Theoretical modeling of metal surfaces in electrolytes indicates that image-charge attraction can significantly increase Stern layer concentrations of counterions.[60] This contrasts with surfaces of materials with lower dielectric constants than water, which are characterized by image-charge repulsion in aqueous electrolyte solutions.[61] The organic monolayer will also alter any image-charge effects. More work is needed to fully characterize the surface chemistry of the colloidal gold nanoparticles for improving the functionality for applications such as molecular sensing, nanomedicine, and catalysis.

2.4 Conclusion

Second harmonic generation is used to obtain the surface charge density of 50 nm gold nanoparticles functionalized with MSA in aqueous colloidal suspension. The experimental results of the SHG electric field as a function of added NaCl and $MgCl_2$ concentrations are most accurately described using the $\chi^{(3)}$ technique with a model based on numerical solutions to the spherical Poisson-Boltzmann which account for the nanoparticle surface curvature, salt valences, and ion adsorption. The best fit of the SHG data determines that the surface charge density of the gold nanoparticles is (−2.0 ±0.1) x 10^{-3} C/m^2, which corresponds to a total charge of −96 ± 6 per

nanoparticle. These results agree with corresponding electrophoretic mobility measurements. In addition, the sodium ion is observed to adsorb with a higher saturated surface charge density compared to the magnesium ion, even though the magnesium ion is observed to have a larger equilibrium constant of adsorption, which is likely the consequence of the different cation valences and solvation free energies. These measurements help to provide an important characterization of the colloidal gold nanoparticle interface for improving potential applications in molecular sensing, nanomedicine, and catalysis.

2.5 References

1. Eustis, S.; El-Sayed, M. A. Why Gold Nanoparticles are More Precious Than Pretty Gold: Noble Metal Surface Plasmon Resonance and its Enhancement of the Radiative and Nonradiative Properties of Nanocrystals of Different Shapes. *Chem. Soc. Rev.* **2006,** *35*, 209-217.

2. Daniel, M.-C.; Astruc, D. Gold Nanoparticles: Assembly, Supramolecular Chemistry, Quantum-Size-Related Properties, and Applications Toward Biology, Catalysis, and Nanotechnology. *Chem. Rev.* **2004,** *104*, 293-346.

3. Link, S.; El-Sayed, M. A. Shape and Size Dependence of Radiative, Non-radiative and Photothermal Properties of Gold Nanocrystals. *Int. Rev. Phys. Chem.* **2000,** *19*, 409-453.

4. Mayer, K. M.; Hafner, J. H. Localized Surface Plasmon Resonance Sensors. *Chem. Rev.* **2011,** *111*, 3828-3857.

5. Saha, K.; Agasti, S. S.; Kim, C.; Li, X.; Rotello, V. M. Gold Nanoparticles in Chemical and Biological Sensing. *Chem. Rev.* **2012,** *112*, 2739-2779.

6. Cao, Y. C.; Jin, R.; Mirkin, C. A. Nanoparticles With Raman Spectroscopic Fingerprints for DNA and RNA Detection. *Science* **2002,** *297*, 1536-1540.

7. Eck, W.; Craig, G.; Sigdel, A.; Ritter, G.; Old, L. J.; Tang, L.; Brennan, M. F.; Allen, P. J.; Mason, M. D. PEGylated Gold Nanoparticles Conjugated to Monoclonal F19 Antibodies as Targeted Labeling Agents for Human Pancreatic Carcinoma Tissue. *Acs Nano* **2008,** *2*, 2263-2272.

8. Casal-Dujat, L.; Rodrigues, M.; Yagüe, A.; Calpena, A. C.; Amabilino, D. B.; González-Linares, J.; Borràs, M.; Pérez-García, L. Gemini Imidazolium Amphiphiles for the Synthesis, Stabilization, and Drug Delivery From Gold Nanoparticles. *Langmuir* **2012,** *28*, 2368-2381.

9. Giljohann, D. A.; Seferos, D. S.; Daniel, W. L.; Massich, M. D.; Patel, P. C.; Mirkin, C. A. Gold Nanoparticles for Biology and Medicine. *Angew. Chem. Int. Ed.* **2010,** *49*, 3280-3294.

10. Von Maltzahn, G.; Park, J.-H.; Lin, K. Y.; Singh, N.; Schwöppe, C.; Mesters, R.; Berdel, W. E.; Ruoslahti, E.; Sailor, M. J.; Bhatia, S. N. Nanoparticles that Communicate in Vivo to Amplify Tumour Targeting. *Nat. Mater.* **2011,** *10*, 545-552.

11. Gao, J.; Huang, X.; Liu, H.; Zan, F.; Ren, J. Colloidal Stability of Gold Nanoparticles Modified With Thiol Compounds: Bioconjugation and Application in Cancer Cell Imaging. *Langmuir* **2012,** *28*, 4464-4471.

12. Chen, J.; Wang, D.; Xi, J.; Au, L.; Siekkinen, A.; Warsen, A.; Li, Z.-Y.; Zhang, H.; Xia, Y.; Li, X. Immuno Gold Nanocages With Tailored Optical Properties for Targeted Photothermal Destruction of Cancer Cells. *Nano Lett.* **2007,** *7*, 1318-1322.

13. El-Sayed, I. H.; Huang, X.; El-Sayed, M. A. Surface Plasmon Resonance Scattering and Absorption of anti-EGFR Antibody Conjugated Gold Nanoparticles in Cancer Diagnostics: Applications in Oral Cancer. *Nano Lett.* **2005,** *5*, 829-834.

14. Clarke, M. L.; Chou, S. G.; Hwang, J. Monitoring Photothermally Excited Nanoparticles via Multimodal Microscopy. *J. Phys. Chem. Lett.* **2010,** *1*, 1743-1748.

15. Qian, X.; Peng, X.-H.; Ansari, D. O.; Yin-Goen, Q.; Chen, G. Z.; Shin, D. M.; Yang, L.; Young, A. N.; Wang, M. D.; Nie, S. In Vivo Tumor Targeting and Spectroscopic Detection With Surface-Enhanced Raman Nanoparticle Tags. *Nat. Biotechnol.* **2007,** *26*, 83-90.

16. Wustholz, K. L.; Henry, A.-I.; McMahon, J. M.; Freeman, R. G.; Valley, N.; Piotti, M. E.; Natan, M. J.; Schatz, G. C.; Duyne, R. P. V. Structure−Activity Relationships in Gold Nanoparticle Dimers and Trimers for Surface-Enhanced Raman Spectroscopy. *J. Am. Chem. Soc.* **2010,** *132*, 10903-10910.

17. Fu, Y.; Zhang, J.; Lakowicz, J. R. Plasmon-Enhanced Fluorescence From Single Fluorophores End-Linked to Gold Nanorods. *J. Am. Chem. Soc.* **2010,** *132*, 5540-5541.

18. Bardhan, R.; Grady, N. K.; Cole, J. R.; Joshi, A.; Halas, N. J. Fluorescence Enhancement by Au Nanostructures: Nanoshells and Nanorods. *Acs Nano* **2009,** *3*, 744-752.

19. Tam, F.; Goodrich, G. P.; Johnson, B. R.; Halas, N. J. Plasmonic Enhancement of Molecular Fluorescence. *Nano Lett.* **2007,** *7*, 496-501.

20. Cade, N.; Ritman-Meer, T.; Richards, D. Strong Coupling of Localized Plasmons and Molecular Excitons in Nanostructured Silver Films. *Phys. Rev. B* **2009,** *79*, 241404.

21. Karam, T. E.; Haber, L. H. Molecular Adsorption and Resonance Coupling at the Colloidal Gold Nanoparticle Interface. *J. Phys. Chem. C* **2013,** *118*, 642-649.

22. Sperling, R. A.; Rivera gil, P.; Zhang, F.; Zanella, M.; Parak, W. J. Biological Applications of Gold Nanoparticles. *Chem. Soc. Rev.* **2008,** *37*, 1896-1908.

23. Eisenthal, K. B. Second Harmonic Spectroscopy of Aqueous Nano-and Microparticle Interfaces. *Chem. Rev.* **2006,** *106*, 1462-1477.

24. Haber, L. H.; Eisenthal, K. B. Molecular Excited-State Relaxation Dynamics at the Colloidal Microparticle Interface Monitored with Pump-Probe Second Harmonic Generation. *J. Phys. Chem. B* **2013,** *117*, 4249-4253.

25. Haber, L. H.; Kwok, S. J. J.; Semeraro, M.; Eisenthal, K. B. Probing the Colloidal Gold Nanoparticle/Aqueous Interface With Second Harmonic Generation. *Chem. Phys. Lett.* **2011,** *507*, 11-14.

26. Jen, S.-H.; Dai, H.-L.; Gonella, G. The Effect of Particle Size in Second Harmonic Generation From the Surface of Spherical Colloidal Particles. II: The Nonlinear Rayleigh−Gans−Debye Model. *J. Phys. Chem. C* **2010,** *114*, 4302-4308.

27. Gonella, G.; Gan, W.; Xu, B.; Dai, H.-L. The Effect of Composition, Morphology, and Susceptibility on Nonlinear Light Scattering From Metallic and Dielectric Nanoparticles. *J. Phys. Chem. Lett.* **2012,** *3*, 2877-2881.

28. Gonella, G.; Dai, H.-L. Second Harmonic Light Scattering from the Surface of Colloidal Objects: Theory and Applications. *Langmuir* **2013,** *30*, 2588-2599.

29. Boyd, R. W. *Nonlinear Optics*. 3rd ed.; Academic Press: New York, USA, 2003.

30. Eisenthal, K. B. Liquid Interfaces Probed by Second-Harmonic and Sum-Frequency Spectroscopy. *Chem. Rev.* **1996,** *96*, 1343-1360.

31. Shen, Y. R. *The Principles of Nonlinear Optics*. Wiley: Hoboken, USA, 2003.

32. Schurer, B.; Wunderlich, S.; Sauerbeck, C.; Peschel, U.; Peukert, W. Probing Colloidal Interfaces by Angle-Resolved Second Harmonic Light Scattering. *Phys. Rev. B* **2010,** *82*, 2414041-2414044.

33. Malin, J. N.; Hayes, P. L.; Geiger, F. M. Interactions of Ca, Zn, and Cd Ions at Buried Solid/Water Interfaces Studied by Second Harmonic Generation. *J. Phys. Chem. C* **2009,** *113*, 2041-2052.

34. Yan, E. C. Y.; Liu, Y.; Eisenthal, K. B. New Method for Determination of Surface Potential of Microscopic Particles by Second Harmonic Generation. *J. Phys. Chem. B* **1998,** *102*, 6331-6336.

35. Hiemenz, P. C.; Rajagopalan, R. *Principles of Colloid and Surface Chemistry, Revised and Expanded*. 3rd ed.; CRC Press: New York, USA, 1997.

36. Ohshima, H.; Healy, T. W.; White, L. R. Accurate Analytic Expressions for the Surface

Charge Density/Surface Potential Relationship and Double-Layer Potential Distribution for a Spherical Colloidal Particle. *J. Colloid Interface Sci.* **1982,** *90*, 17-26.

37. Subir, M.; Liu, J.; Eisenthal, K. B. Protonation at the Aqueous Interface of Polymer Nanoparticles With Second Harmonic Generation. *J. Phys. Chem. C* **2009,** *113*, 20772-20772.

38. Wang, H.-f.; Borguet, E.; Yan, E.; Zhang, D.; Gutow, J.; Eisenthal, K. Molecules at Liquid and Solid Surfaces. *Langmuir* **1998,** *14*, 1472-1477.

39. Yan, E. C.; Eisenthal, K. B. Probing the Interface of Microscopic Clay Particles in Aqueous Solution by Second Harmonic Generation. *J. Phys. Chem. B* **1999,** *103*, 6056-6060.

40. Liu, Y.; Yan, C. Y.; Zhao, X. L.; Eisenthal, K. B. Surface Potential of Charged Liposomes Determined by Second Harmonic Generation. *Langmuir* **2001,** *17*, 2063-2066.

41. Doughty, B.; Rao, Y.; Kazer, S. W.; Kwok, S. J.; Turro, N. J.; Eisenthal, K. B. Binding of the Anti-Cancer Drug Daunomycin to DNA Probed by Second Harmonic Generation. *J. Phys. Chem. B* **2013,** *117*, 15285-15289.

42. Chen, E. H.; Saslow, S. A.; Nguyen, S. T.; Geiger, F. M. Zinc Ion–Hydroxyl Interactions at Undecanol-Functionalized Fused Silica/Water Interfaces Using the Eisenthal χ (3) Technique. *J. Phys. Chem. C* **2012,** *116*, 7016-7020.

43. Malin, J. N.; Holland, J. G.; Saslow, S. A.; Geiger, F. M. U(VI) Adsorption and Speciation at the Acidic Silica/Water Interface Studied by Resonant and Nonresonant Second Harmonic Generation. *J. Phys. Chem. C* **2011,** *115*, 13353-13360.

44. Boman, F. C.; Gibbs-Davis, J. M.; Heckman, L. M.; Stepp, B. R.; Nguyen, S. T.; Geiger, F. M. DNA at Aqueous/Solid Interfaces: Chirality-Based Detection via Second Harmonic Generation Activity. *J. Am. Chem. Soc.* **2008,** *131*, 844-848.

45. Holland, J. G.; Jordan, D. S.; Geiger, F. M. Divalent Metal Cation Speciation and Binding to Surface-Bound Oligonucleotide Single Strands Studied by Second Harmonic Generation. *J. Phys. Chem. B* **2011,** *115*, 8338-8345.

46. Walter, S. R.; Geiger, F. M. DNA on Stage: Showcasing Oligonucleotides at Surfaces and Interfaces With Second Harmonic and Vibrational Sum Frequency Generation. *J. Phys. Chem. Lett.* **2009,** *1*, 9-15.

47. Tisdale, W. A.; Williams, K. J.; Timp, B. A.; Norris, D. J.; Aydil, E. S.; Zhu, X.-Y. Hot-Electron Transfer From Semiconductor Nanocrystals. *Science* **2010,** *328*, 1543-1547.

48. Tuinier, R. Approximate Solutions to the Poisson–Boltzmann Equation in Spherical and Cylindrical Geometry. *J. Colloid Interface Sci.* **2003,** *258*, 45-49.

49. Kimura, K.; Takashima, S.; Ohshima, H. Molecular Approach to the Surface Potential

Estimate of Thiolate-Modified Gold Nanoparticles. *J. Phys. Chem. B* **2002,** *106*, 7260-7266.

50. Makino, K.; Ohshima, H. Electrophoretic Mobility of a Colloidal Particle with Constant Surface Charge Density. *Langmuir* **2010,** *26*, 18016-18019.

51. Dukhin, S.; Zimmermann, R.; Werner, C. A Concept for the Generalization of the Standard Electrokinetic Model. *Colloids Surf., A* **2001,** *195*, 103-112.

52. Perrault, S. D.; Chan, W. C. W. Synthesis and Surface Modification of Highly Monodispersed, Spherical Gold Nanoparticles of 50-200 nm. *J. Am. Chem. Soc.* **2009,** *131*, 17042-17043.

53. Evans, D. F.; Wennerström, H. *The Colloidal Domain: Where Physics, Chemistry, Biology, and Technology Meet*. Wiley-VCH: New York, 1999.

54. Vance, F. W.; Lemon, B. I.; Hupp, J. T. Enormous Hyper-Rayleigh Scattering From Nanocrystalline Gold Particle Suspensions. *J. Phys. Chem. B* **1998,** *102*, 10091-10093.

55. Salafsky, J.; Eisenthal, K. Protein Adsorption at Interfaces Detected by Second Harmonic Generation. *J. Phys. Chem. B* **2000,** *104*, 7752-7755.

56. Lyklema, J.; Overbeek, J. T. G., On the Interpretation of Electrokinetic Potentials. *J. Colloid Sci.* **1961,** *16*, 501-512.

57. Lyklema, J., Molecular Interpretation of Electrokinetic Potentials. *Curr. Opin. Colloid Interface Sci.* **2010,** *15*, 125-130.

58. Marcus, Y., *Ion Properties*, Marcel Dekker Inc., New York, USA, 1997.

59. Chen, S.; Kimura, K. Synthesis and Characterization of Carboxylate-Modified Gold Nanoparticle Powders Dispersible in Water. *Langmuir* **1999,** *15*, 1075-1082.

60. Brüesch, P.; Christen, T. The Electric Double Layer at a Metal Electrode in Pure Water. *J. Appl. Phys.* **2004,** *95*, 2846-2856.

61. Hatlo, M. M.; Lue, L. The Role of Image Charges in the Interactions Between Colloidal Particles. *Soft Matter* **2008,** *4*, 1582-1596.

CHAPTER 3

MONITORING THE PHOTOCLEAVING DYNAMICS OF COLLOIDAL MICRORNA-FUNCTIONALIZED GOLD NANOPARTICLES USING SECOND HARMONIC GENERATION*

3.1 Introduction

Short oligonucleotides including small interfering RNA (siRNA) and microRNA (miRNA) are involved in the post-translational control of gene expression and have become increasingly important in basic and applied biology.[1-6] Because systemically administered siRNA and miRNA are rapidly degraded by RNases in the bloodstream before reaching their cellular targets, methods of protecting and delivering these oligonucleotides are important to the development of RNA-based therapeutics.[7-10] Thiolation of synthetic oligonucleotide strands and attachment to metal nanoparticles has become an important method to protect the oligonucleotide from enzymatic degradation and to facilitate transport into the cell.[11, 12] Our previous work has demonstrated that short nucleotide strands of antisense DNA[13] and osteogenic miRNA-148b[14] are able to be attached to silver nanoparticles through thiol functionalization and then transported into mammalian cells, altering their fate after being released from the particle by photoactivation. Light activation presents a method with a greater potential for spatiotemporally controlled release than alternate methods based on chemical stimuli, pH, or ionic strength.[14-18]

The unique optical properties of gold nanoparticles (GNPs), especially their activity in the visible and near-infrared regions, along with their biocompatibility and ease of synthesis, enable a number of applications including molecular sensing, labeling, drug delivery, and photothermal cancer treatment.[15-19] The optical properties of GNPs are derived from the surface plasmon

resonances which are characterized by the coherent oscillation of free electrons under incident light.[20-23] The plasmon resonances can cause significant optical field enhancements leading to processes such as surface enhanced Raman spectroscopy (SERS),[24, 25] surface enhanced fluorescence,[26, 27] and plasmon-exciton polariton resonant coupling.[28] Gold nanoparticles having various geometries such as nanorods, nanocages, and nanoshells are attractive nanomaterials for optical contrast enhancement agents, cancer diagnosis, and therapeutics.[29-31] Recent *in vivo* studies of oligonucleotide-functionalized GNPs have demonstrated their powerful ability for cancer gene therapy through controlled release.[32, 33] GNPs can be functionalized with miRNA using the same thiolization method as silver nanoparticles and many other metallic nanoparticles.[13, 14] To date, several groups have investigated light-activated nucleic acid delivery using GNPs to demonstrate the controlled release of DNA,[16, 17] the selective release of multiple DNAs,[18] and light-activated gene silencing.[15]

Here, we report the use of nonlinear spectroscopy to probe the nanoparticle surface during the process of oligonucleotide photorelease. Nonlinear laser spectroscopies such as second harmonic generation (SHG) and sum frequency generation are powerful, noninvasive, surface-sensitive techniques that are useful for the investigation of colloidal nanoparticles.[28, 34-36] In SHG spectroscopy, two incident photons of frequency ω add coherently to generate a photon of frequency 2ω. SHG is dipole forbidden in bulk media with inversion symmetry, but it can be generated from the surface and interfaces of nanoparticles where the inversion symmetry is broken.[37-39] The release of highly negatively charged miRNA from the surface of GNPs is an ideal candidate for SHG spectroscopy investigations. The SHG signal from this charged interface has two components given by the second-order susceptibility $\chi^{(2)}$, which is based on the two-photon spectroscopy, and the third-order susceptibility $\chi^{(3)}$, which is based on the electrostatic potential

from the nanoparticle surface.[40-43] The SHG electric field E_{SHG} is proportional to the square root of SHG signal and is given by

$$E_{SHG} = \chi^{(2)} E_\omega E_\omega + \chi^{(3)} E_\omega E_\omega \, \Phi_0 \qquad (3.1)$$

where E_ω is the incident electric field of the fundamental laser at frequency ω and Φ_0 is the electrostatic surface potential. The $\chi^{(2)}$ term can be sensitive to any chemical change on the nanoparticle surface that causes a spectroscopic change at either ω or 2ω. The $\chi^{(3)}$ term depends on the net polarization of bulk molecules in the solvent which are induced by the electric field of the nanoparticle surface.[44, 45]

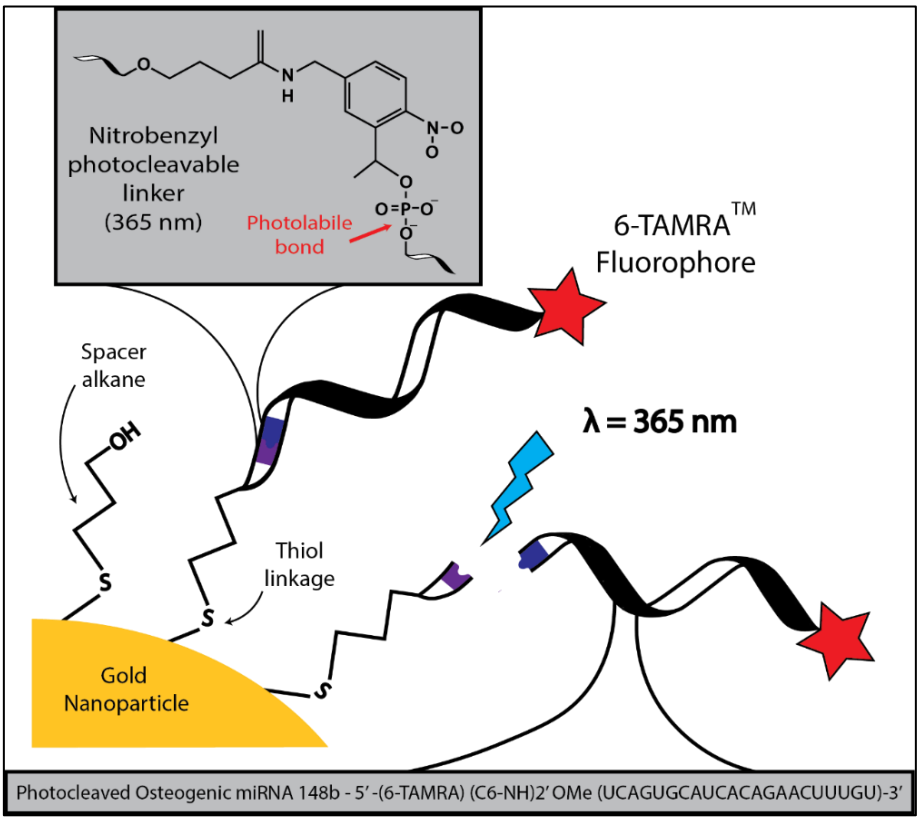

Figure 3.1. Schematic representation of the PC-miRNA-148b functionalized gold nanoparticle attached with fluorophore 6-TAMRA. The nitrobenzyl photocleaveable group, between the spacer linker and the oligonucleotide, absorbs UV radiation centered at 365 nm to release the miRNA from the surface of the gold nanoparticle.

In this study, we demonstrate the applicability of SHG spectroscopy to light-activated gene delivery by measuring the wavelength and power dependence of the kinetics associated with miRNA release from GNPs using nitrobenzyl photocleavable (PC) chemistry. The experimental setup uses a probe laser at 800 nm to generate SHG signals for real-time monitoring of the miRNA photorelease from the GNP surface. A second laser is used to induce the photocleaving under varying wavelengths and powers. GNPs of 68 nm diameter are functionalized by a synthetic miRNA-148b that has been thiolated and modified with an ultraviolet-active nitrobenzyl photocleavable group,[14, 46] as shown schematically in Figure 3.1. SHG measurements as a function of irradiation time using different photocleaving laser wavelengths are conducted and compared to corresponding fluorescence quantification measurements and extinction spectra to investigate photocleaving efficiencies. Additionally, analysis of the photocleaving dynamics are monitored using time-dependent SHG measurements under different ultraviolet (UV) irradiation powers to better understand the kinetics of the photocleaving process.

3.2 Synthesis and Characterization of Gold Nanoparticles

The colloidal gold nanoparticle sample of 68 nm diameter is prepared using a seeded-growth method where citrate is first used as a reducing agent and capping agent for the gold nanoparticle seeds followed by the addition of a stronger reducing agent, hydroquinone, to produce larger GNPs with low polydispersity. During the gold nanoparticle seed synthesis, 900 μL of 34 mM sodium citrate is added to 30 mL of 290 μM gold chloride in ultrapure water under boiling conditions with vigorous stirring. The solution changes color to a bright red after 10 minutes and is then cooled to room temperature. In the second step, 150 μL of the seed solution is added to 2.9 mM of gold chloride in 10 mL of ultrapure water, followed by the addition of 100 μL of 0.03 M hydroquinone and 22 μL of 34 mM sodium citrate. The solution is left to stir at room temperature

for 60 min to produce the 68 nm colloidal gold nanoparticles.

The surface of the gold nanoparticles are functionalized with fluorophore-labeled miRNA via a 'salt-ageing' technique as described previously.[14] Here, 2.5 µL of 0.8 µg/µL of the miRNA-148b (PC-miR-148b) modified with the thiolated photocleavable nitrobenzyl group and labeled with a 6-TAMRA fluorophore group is added to 1 mL of the gold nanoparticles at a concentration of 8.25 x 10^9 nanoparticles/mL. The mixed samples are left to incubate for 24 h under gentle agitation conditions. Following the incubation period, 10 µL of 0.035 M sodium dodecyl sulfate (SDS) solution and 20 µL of 0.01 M phosphate buffer saline solution (PBS) solution are added to each sample. After an additional 3 h of incubation, a 10 µL solution of 2 M tris(hydroxymethyl) aminomethane (Tris) and 2 M NaCl is added three times, with 3 h of incubation between each salting step. The miRNA-functionalized nanoparticles are purified via centrifugation three consecutive times at 7000 rpm for 20 min each. During the first two centrifugation cycles, the precipitate obtained from 1 mL of sample is resuspended in 1 mL of solution containing 0.035 M SDS, 0.1 M Tris, 0.103 M NaCl, and 0.0005 M disodium diphosphate, and finally in 1 mL of deionized water after the third centrifugation.

The gold nanoparticles are characterized using transmission electron microscopy (TEM), dynamic light scattering, extinction spectroscopy, and zeta potential measurements. The average nanoparticle diameter is determined to be 68 ± 7 nm diameter from TEM measurements, with representative TEM images shown in Figure 3.2 (a). Figure 3.2 (b) shows TEM images of GNPs after functionalization with miRNA, where a very thin layer of approximately 2 nm in thickness is observed around the nanoparticles, showing the added functionalized miRNA. Figure 3.3 displays the experimental extinction spectrum of the 68 nm GNPs in water (red line) with a localized surface plasmon peak centered on 543 nm, compared to the best fit from Mie theory

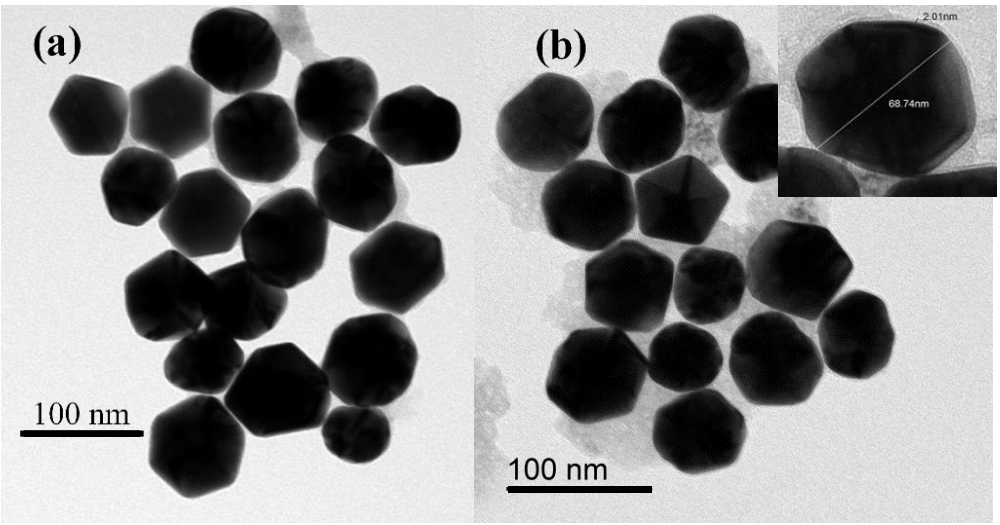

Figure 3.2. Representative TEM images of (a) gold nanoparticles and (b) gold nanoparticles functionalized with PC-miRNA-148b.

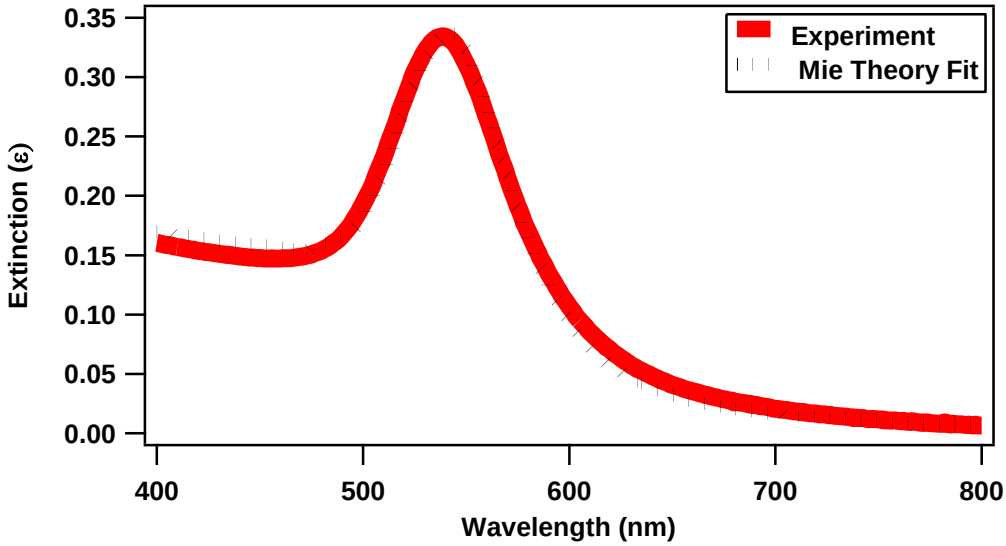

Figure 3.3. Extinction spectrum of the 68 nm colloidal gold nanoparticle sample in water (red line) compared with the best fit from Mie theory (dotted black line).

(dashed gray line) at a concentration of 8.25×10^9 nanoparticles/mL. Dynamic light scattering measurements determine the hydrodynamic diameter of the GNP sample to be 68 ± 15 nm, in agreement with the TEM and extinction spectroscopy results. The hydrodynamic diameter of the GNPs after functionalizing with miRNA increases to 140 ± 20 nm, due to the attached miRNA in solution.

The zeta potential of the colloidal GNP sample before and after functionalization with miRNA is obtained from electrophoretic mobility measurements using the Huckel approximation.[47] The electrophoretic mobility for the GNPs and the GNPs functionalized with miRNA is shown in Figure 3.4. The electrophoretic mobility of GNPs is measured to be $(-2.65 \pm 0.8) \times 10^{-8}$ m^2/Vs with a corresponding zeta potential -50 ± 17 mV. The electrophoretic mobility of miRNA-functionalized GNPs is measured to be $(-3.98 \pm 0.9) \times 10^{-8}$ m^2/Vs with a corresponding zeta potential -76 ± 18 mV, where the highly-charged miRNA attached to the surface in aqueous solution increases the negative zeta potential.

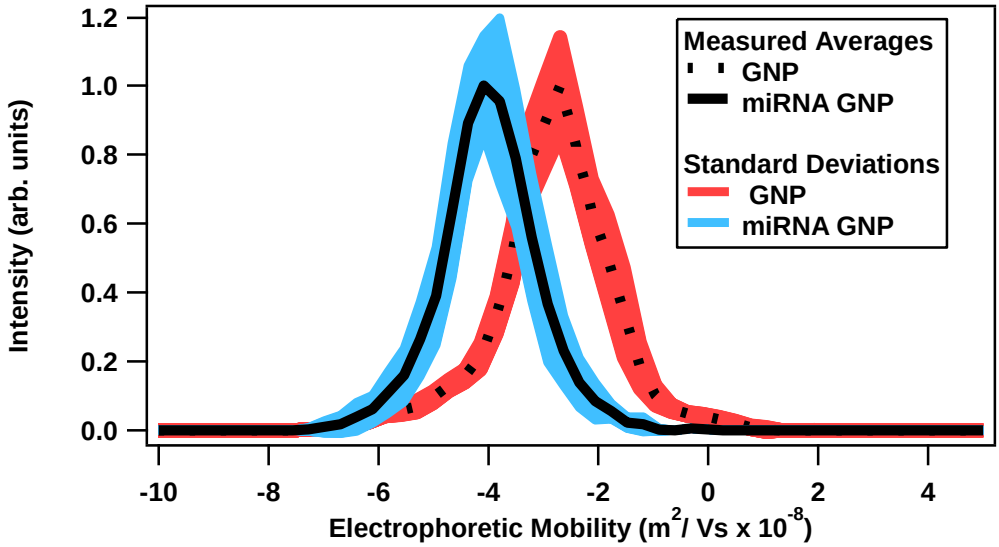

Figure 3.4. Electrophoretic mobility plot of gold nanoparticles and miRNA-functionalized gold nanoparticles showing the measured averages (dashed and solid black lines, respectively) and corresponding standard deviations (red and blue areas, respectively).

3.3 Experimental Setup

The experimental setup for the second harmonic generation studies, shown schematically in Figure 3.5, is modified from a previously reported version.[28, 45] The setup uses a titanium:sapphire oscillator laser, a titanium:sapphire amplifier laser, an optical parametric amplifier (OPA) laser, an optical setup, and a high-sensitivity CCD spectroscopy detector. The oscillator laser operates

at a center wavelength of 800 nm with 75 fs pulses at a repetition rate of 80 MHz and an average power of 2.5 W. A beamsplitter separates the oscillator laser beam into one path that is used as the probe laser for the SHG measurements and another path that is used to seed the amplifier.

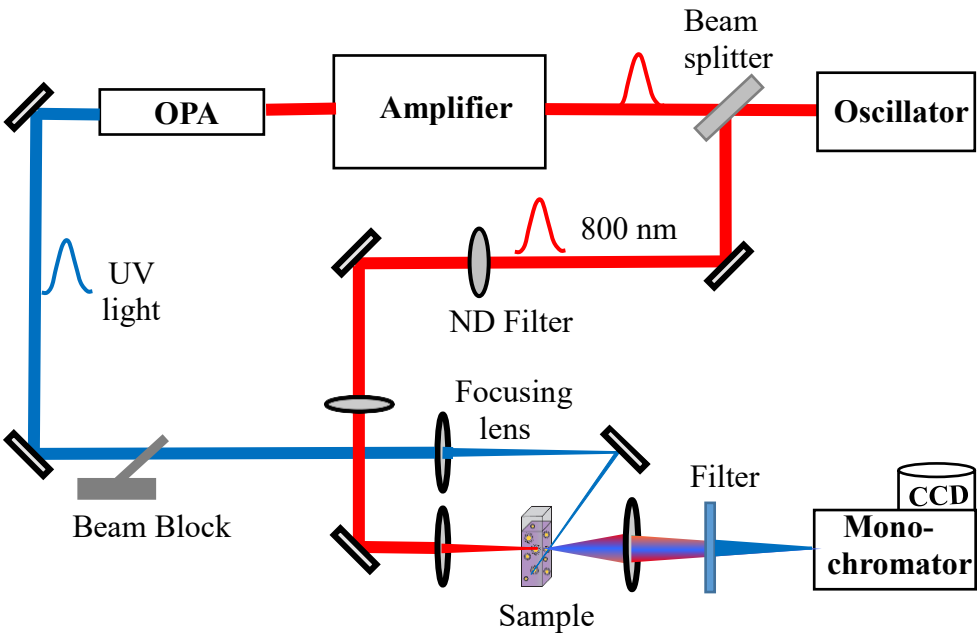

Figure 3.5. Experimental setup showing the UV beam (blue) and 800 nm probe (red) beam, which are focused to the colloidal nanoparticle sample in a 1 cm quartz cuvette, with the SHG signal detected using a spectroscopy CCD detector.

A portion of the amplifier laser is sent through the OPA to generate the tunable UV or visible wavelengths with 100 fs pulses at a repetition rate of 10 kHz. The 800 nm probe laser beam for SHG measurements is attenuated to an average power of 790 mW and focused to the 1.5 mL colloidal sample, which is contained in a 1 cm by 1 cm quartz cuvette at a concentration of 8.25 $\times 10^9$ nanoparticles/mL in water with the SHG collected in the forward direction. The wavelength-tunable visible or UV beam for photoactivation is directed to the nanoparticle sample at 90° with respect to the 800 nm beam. The SHG from the nanoparticle sample is measured as a function of the UV laser irradiation time for investigating photocleaving reaction dynamics from the miRNA-functionalized GNPs. A beam block opens and shuts on the photocleaving UV beam every 30

seconds in synchronization with an automated file-saving program so that the SHG can be measured in real time to monitor the photoactivated drug-delivery reaction. A variable neutral density filter is used to control the power of the UV laser. Automated stirring is initiated during the UV laser irradiation and is stopped when the UV laser is blocked for stable SHG measurements, which are collected at multiple 1 second acquisitions for statistical analysis.

3.4 Results and Discussion

The light-activated controlled release of oligonucleotides from the surface of gold nanoparticles is monitored in real time using second harmonic generation. Representative SHG spectra of the GNPs and the miRNA-functionalized GNPs are shown in Figure 3.6 (a) under the same 800 nm laser conditions and nanoparticle concentrations. The SHG peak is centered at 400 nm with a full width half maximum of 4.5 nm. The slight rise in signal at longer wavelengths is due to the two-photon fluorescence from the GNPs. The larger SHG signal from the miRNA-functionalized GNP sample compared to the GNP sample arises primarily as a consequence of the highly-charged miRNA leading to a higher electrostatic surface potential magnitude and a larger $\chi^{(3)}$ term in equation (1), although some added contribution may also result from an increased $\chi^{(2)}$ term. The 6-TAMRA fluorophore label attached to the miRNA is chosen for corresponding fluorescence quantization measurements, while having minimal absorption at either 800 nm or 400 nm, where no added fluorescence is observed in the SHG spectra so the fluorophore is expected to have negligible SHG contribution. Figure 3.6 (b) displays the SHG spectra of the miRNA-functionalized GNPs exposed to different UV irradiation times of 0 s, 30 s, and 90 s using 365 nm at 85 mW. As the UV irradiation time increases, the SHG intensity decreases and asymptotically approaches a minimum value. The decrease in SHG intensity as a function of UV laser irradiation time is due to the change in the surface structure and surface charge leading to a change in the

corresponding $\chi^{(2)}$ and $\chi^{(3)}$ terms upon photocleaving. The change in the $\chi^{(3)}$ term is expected to be the dominant contribution to the change in the SHG signal due to the loss of the highly-charged miRNA upon photocleaving.

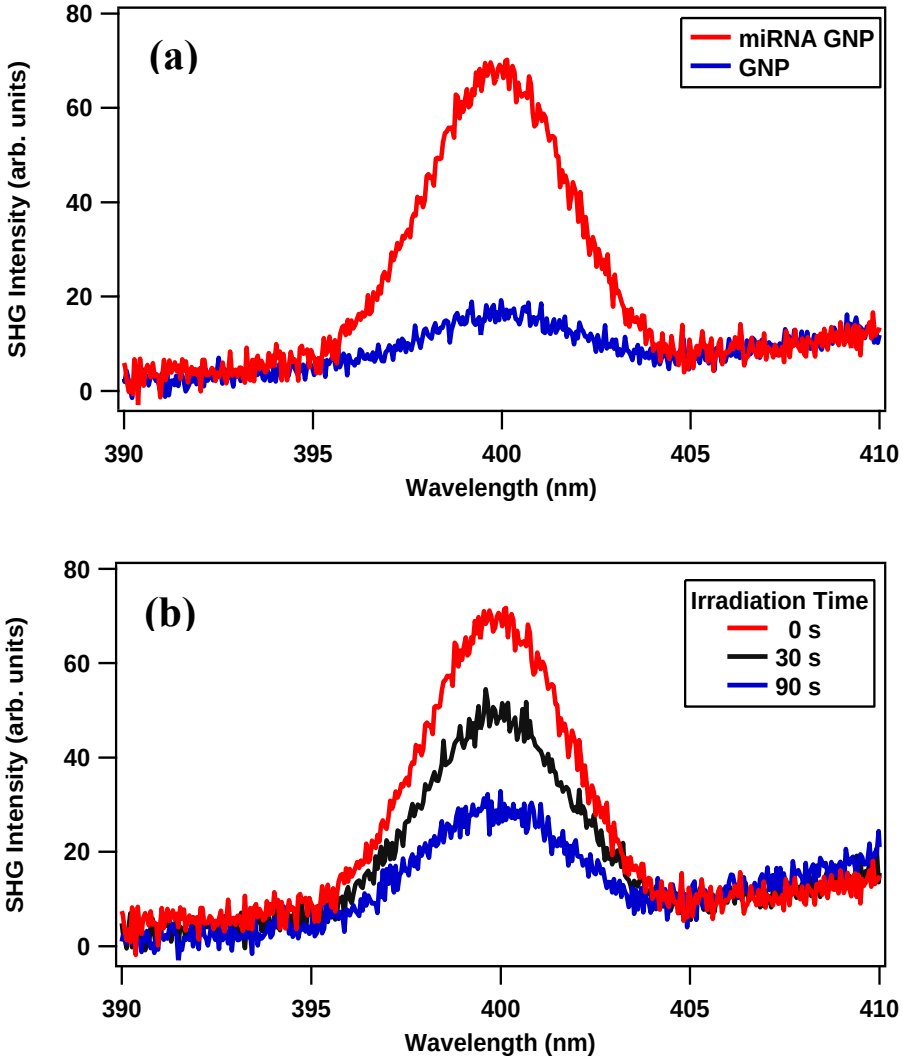

Figure 3.6. (a) SHG spectrum of colloidal miRNA-functionalized gold nanoparticle sample compared with SHG spectrum of gold nanoparticles only. (b) SHG spectra of miRNA-functionalized colloidal gold nanoparticle sample after different UV irradiation times using 365 nm with 85 mW average power. The probe laser is fixed at 800 nm.

Figure 3.7 (a) displays results from control experiments which show the SHG signal from GNPs and miRNA-functionalized GNPs as a function of time. The SHG signal for the miRNA-functionalized GNPs is shown to remain constant over time when using the 800 nm probe laser

only (blue data points). Additionally, the SHG signal from the GNPs is shown to remain constant over time when using both the 800 nm probe laser and the UV laser at 365 nm and 20 mW average power (black data points), while maintaining a much lower SHG signal than the miRNA-functionalized GNPs. However, the SHG signal from the miRNA-functionalized GNPs decreases as a function of time and asymptotically approaches a minimum value when using both the 800 nm probe laser and the UV laser at 365 nm and 20 mW average power (red data points) due to the photocleaving dynamics. The asymptotic minimum value of the miRNA-functionalized GNPs after UV irradiation is approximately equal to the SHG signal of the GNPs, indicating the miRNA-functionalized GNPs has the roughly same SHG signal as the GNPs after photocleaving is complete. This real-time monitoring of photocleaving dynamics is investigated under varying UV laser wavelengths and powers, and the photocleaving results are verified using extinction spectroscopy and fluorimetry measurements.

Figure 3.7 (b) shows a wavelength-dependent study on the photocleaving dynamics of miRNA from the nanoparticle surface. When the sample is irradiated with the UV laser at 365 nm, which is on resonance with the PC linker, there is a fast decay of the SHG signal, corresponding to a fast rate of photocleaving and a large release of miRNA. The decay rate of the SHG signal decreases when the UV wavelength is off resonance compared to the PC linker, resulting in a slower rate of photocleaving and nucleotides release. The time-dependent SHG intensity under the UV irradiation wavelengths of 330 nm, 375 nm, and 415 nm results in slower rates of photocleaving in comparison to the 365 nm results, while irradiation at 500 nm and 300 nm does not produce any measurable photocleaving. The UV laser power is kept constant at 20 mW for direct comparison of the photocleaving rate at all of these wavelengths.

In order to quantify the photocleaving dynamics, a simple model is described. SHG is

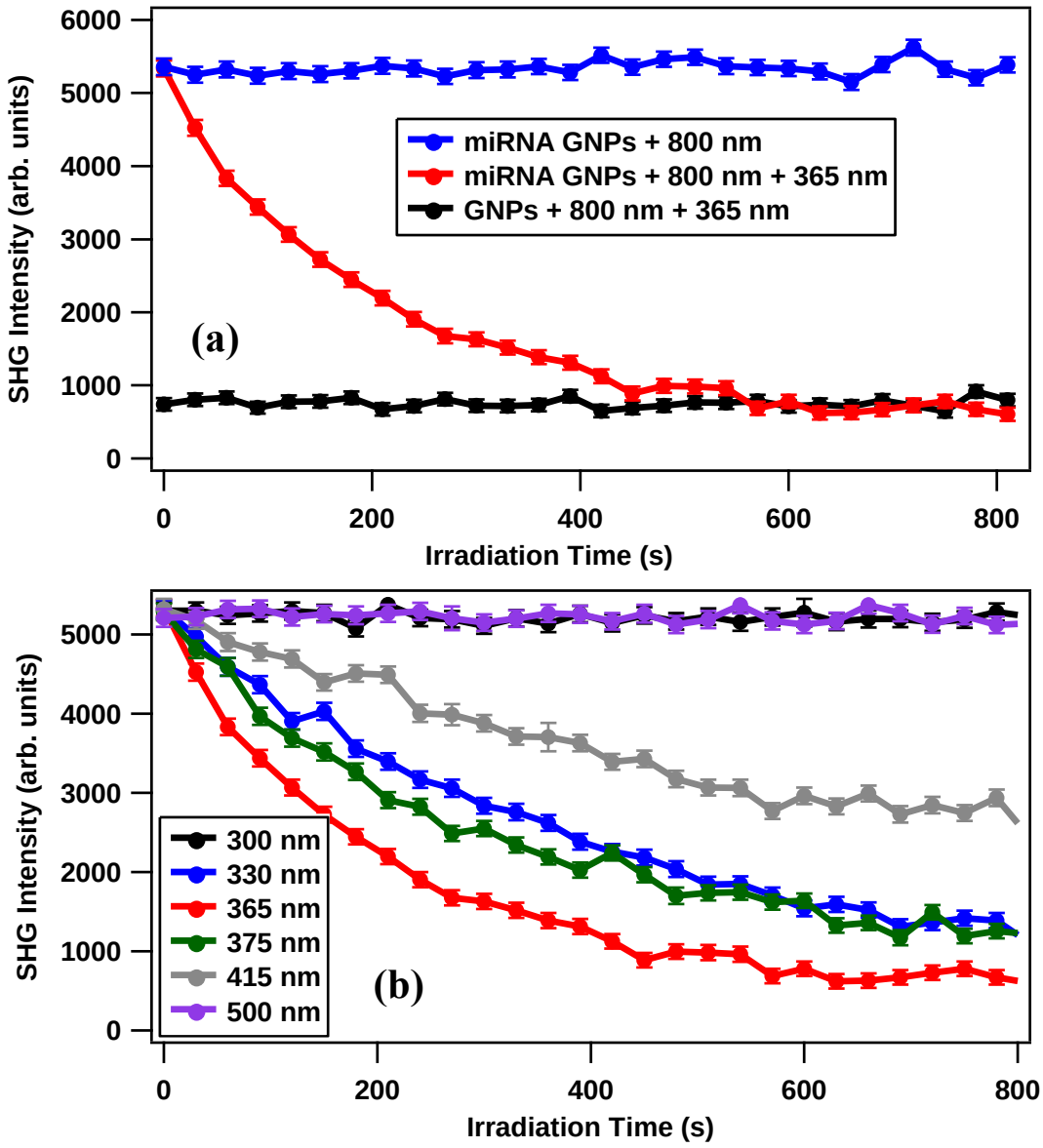

Figure 3.7. (a) The SHG signal remains constant in time for both the miRNA-functionalized GNPs using the 800 nm probe laser only (blue data) and the GNPs using the 800 nm probe and the UV laser at 365 nm (black data). The SHG decreases as a function of time when the miRNA-functionalized GNPs are irradiated with the UV laser at 365 nm (red data). (b) Time-dependent SHG measurements show the photocleaving dynamics of miRNA from the surface of gold nanoparticles using different UV and visible laser wavelengths at 20 mW average power.

understood to be a coherent process from the surface of each individual colloidal nanoparticle, while the overall SHG signal is the incoherent sum of the SHG signal from each nanoparticle in the probe laser focus such that the SHG signal is linearly proportional to the nanoparticle

concentration.[34, 38] Therefore, using the results from Figure 3.7 (a), the SHG electric field can be expressed using the equation $E_{SHG} = A + B[C]$, where A is an offset that includes background signal and the SHG from GNPs, $[C]$ is the cumulative concentration of attached miRNA on the GNP surface, and B is a proportionality constant. If we assume a single UV photon causes photocleaving from a single miRNA attached to the GNP surface with an associated equilibrium constant k, then the change in $[C]$ with respect to time $d[C]/dt$ is equal to $-k[C][h\nu]$, where $[h\nu]$ is the concentration or intensity of UV light. Under constant UV irradiation intensity, the time dependence of $[C]$ should follow an exponential decay given by $[C](t) = [C]_0 e^{-k't}$ where $[C]_0$ is the initial concentration of attached miRNA on the GNP surface and $k' = k[h\nu]$. Notice that the pseudo first-order rate constant k' is linearly proportional to the UV light intensity. Under this simple model, assuming the photocleaving occurs through a one-photon process, the SHG electric field, which is proportional to the square root of the SHG signal, is expected to decay exponentially as a function of UV irradiation time, with a rate constant that is linearly proportional to the UV laser power.

In order the test the accuracy of this model, the kinetics of the photocleaving process for miRNA-functionalized GNPs are studied using different UV laser powers centered at 365 nm. The measured time-dependent SHG electric field from colloidal miRNA-functionalized GNP sample under varying UV laser powers is shown in Figure 3.8 (a). Each set of results are fit to a pseudo first-order exponential decay, as explained above, for UV laser powers of 35 mW, 45 mW, 55 mW, 75 mW, and 85 mW, respectively, to obtain the rate constants k' of $(4.57 \pm 0.4) \times 10^{-3}$ S^{-1}, $(6.44 \pm 0.4) \times 10^{-3}$ S^{-1}, $(7.6 \pm 0.8) \times 10^{-3}$ S^{-1}, $(9.71 \pm 0.6) \times 10^{-3}$ S^{-1}, and $(11.2 \pm 0.7) \times 10^{-3}$ S^{-1}, respectively. Figure 3.8 (b) displays these measured rate constants as a function of UV laser power. The linear best fit is given by a slope of $(1.26 \pm 0.07) \times 10^{-4}$ $S^{-1}mW^{-1}$ and a y-intercept of is (4.7

± 4.5) × 10^{-4} S^{-1} and is in excellent agreement with the data, verifying that the photocleaving associated with the miRNA-functionalized GNPs is a one-photon process.

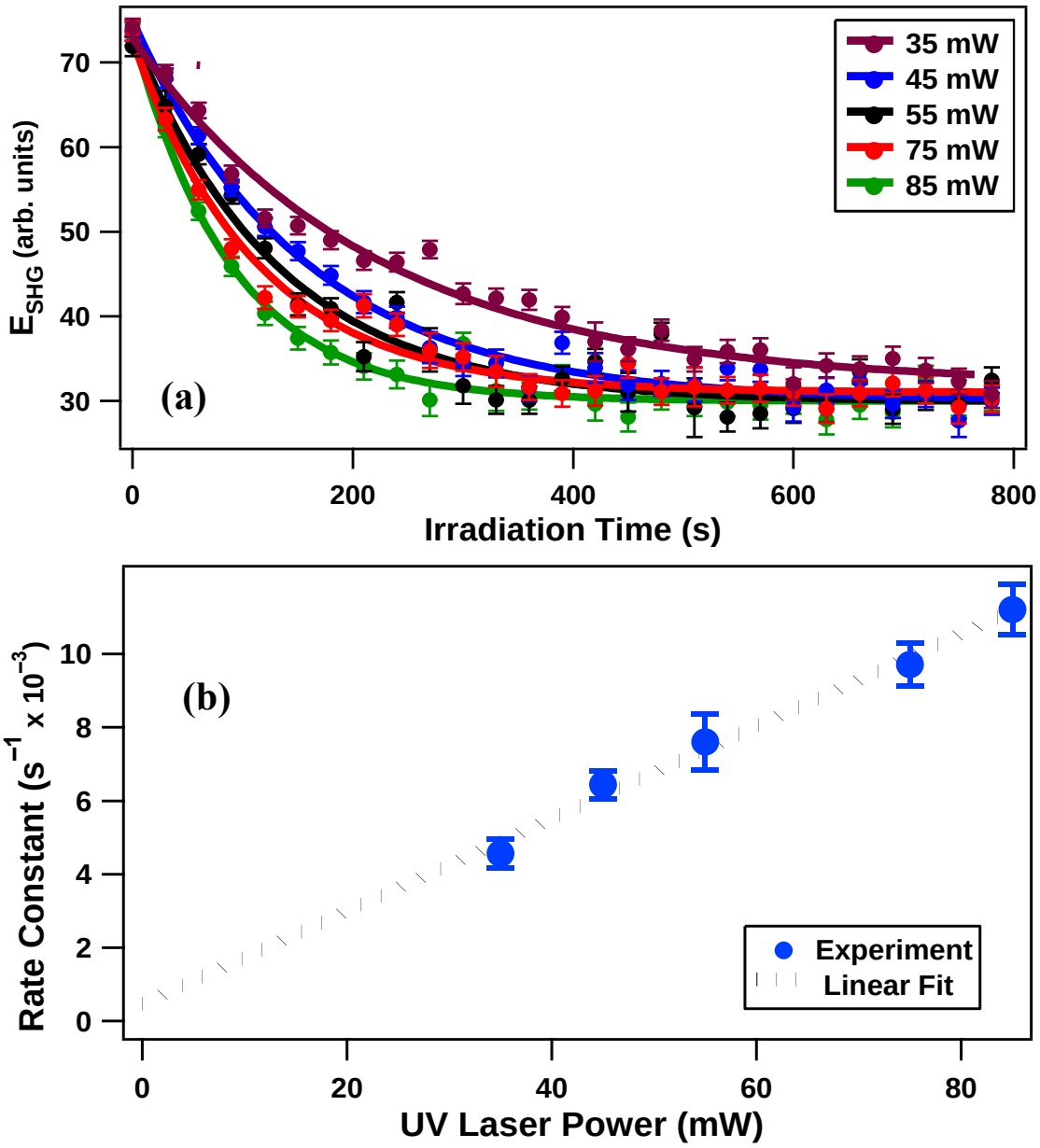

Figure 3.8. (a) Measured SHG electric field from miRNA-functionalized GNPs as a function of irradiation time with 365 nm at different UV laser average powers with corresponding exponential fits. (b) The obtained rate constants are plotted as a function of UV laser power. The linear variation as a function of laser power indicates a one-photon process.

The laser-assisted controlled release of miRNA from the surface of GNPs is further analyzed using extinction spectroscopy measurements. Figure 3.9 shows a significant shift in plasmon peak of the GNPs from 543 nm to 553 nm after functionalization with nucleotides. The extinction spectra is blueshifted after UV laser irradiation of the sample compared to the original miRNA-functionalized GNP sample. These results further indicate that the oligonucleotides are releasing from the surface of GNP upon the UV laser irradiation. Analysis of these

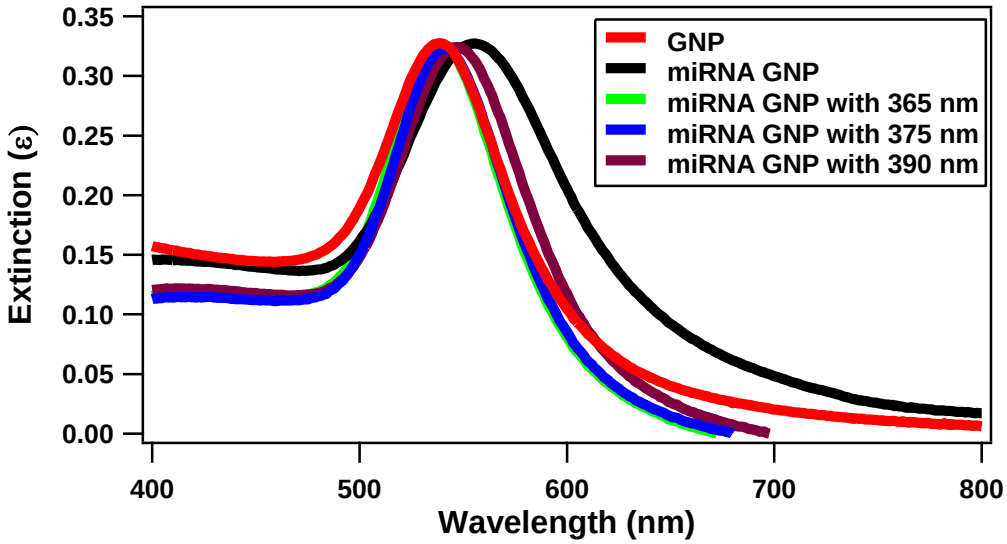

Figure 3.9. The extinction spectra of colloidal miRNA-functionalized gold nanoparticles after irradiating at different UV laser wavelengths. The extinction spectrum of the miRNA-functionalized GNPs is redshifted with respect to the spectrum of GNPs only. After photocleavage with UV laser irradiation, all spectra are blueshifted compared to the miRNA-functionalized GNPs.

measurements demonstrates that the extinction spectrum of colloidal GNPs closely matches the extinction spectrum of the miRNA functionalized GNP sample after irradiation at 20 mW of 365 nm for 13 min, with the plasmon peak blueshifting back to 543 nm. At longer UV irradiation wavelengths of 375 nm and 390 nm, under 20 mW for 13 min there is less blueshifting in the extinction spectra compared to the miRNA-GNPs, going back to plasmon peaks of 545 nm and 548 nm, respectively, indicating incomplete photocleaving of the miRNA from the gold nanoparticle surface. However, the extinction coefficients at 800 nm and 400 nm change only

slightly upon photocleaving, giving more evidence that the large change in the SHG signal is predominantly caused by the change in the electrostatic surface potential.

The amount of miRNA released from the surface of the nanoparticles is quantified using fluorescence measurements. For comparison, the concentration of miRNA molecules on the surface of the GNPs are first quantified using fluorescent-plate readings after chemical detachment of the miRNA. A volume of 10 µL of 65 mM of dithiothreitol (DTT) is added to 1 mL of the gold nanoparticles to reduce the miRNA, followed by agitation and 20 min of incubation at 37 °C for complete chemical cleavage of the oligonucleotides. The samples are then centrifuged at 7000 rpm and three separate 100 uL aliquots of the supernatant are transferred to a 96-well plate for each sample. The concentration is then determined from a constructed standardized curve of the 6-TAMRA fluoro group that is attached to the end of the miRNA.[14] The oligonucleotide coverage for nanoparticles is determined to be 92 ± 21 oligo/nanoparticle, yielding a surface density of (6.30 ± 1.48) x 10^{-3} oligo/nm^2. The fluorescent signal after DTT reduction and after irradiation with 20 mW average power for the different laser wavelengths of 365 nm, 375 nm, 390 nm, and 500 nm, respectively, for 13 min is shown in Fig. 10. Photocleaving is shown to be most efficient at 365 nm on resonance with the nitrobenyl group, in agreement with the time-dependent SHG measurements. The corresponding extinction spectroscopy and fluorimetry measurements all agree with the general description provided by the SHG results, demonstrating a consistent interpretation of the photoactivated controlled release of oligonucleotides from the gold nanoparticle surface. Future research will work to investigate the role of plasmon enchancement on the photocleaving kinetics and extend the photocleaving wavelength to near infrared energies for improved drug-delivery applications.

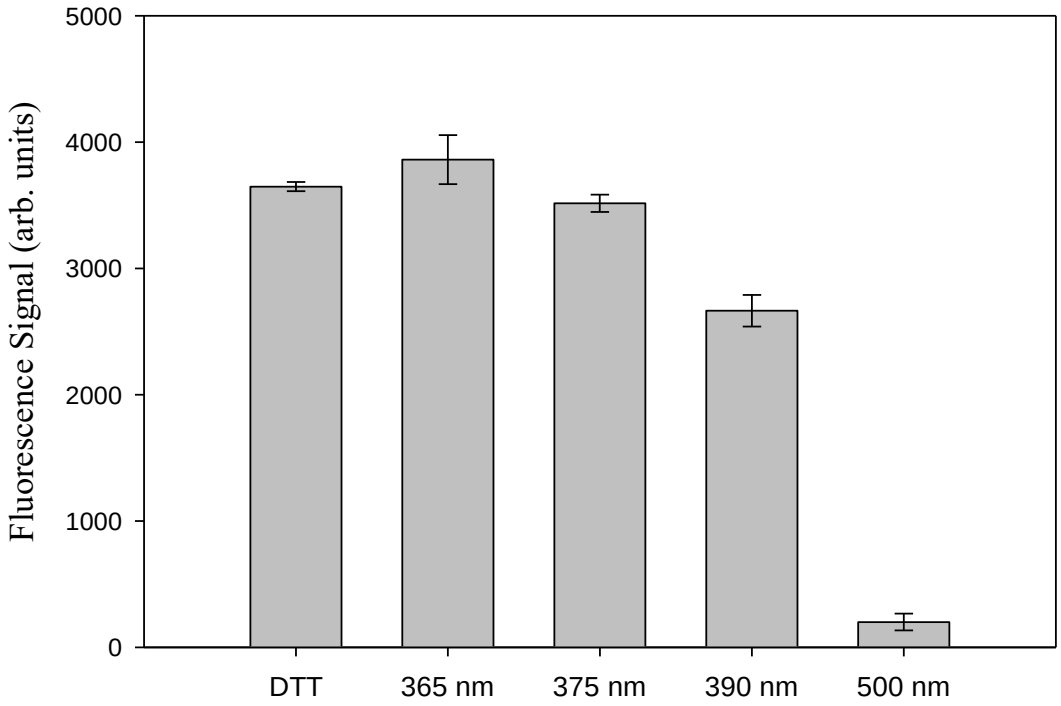

Figure 3.10. Fluorescence measurements of the supernatants of the miRNA-functionalized GNPs after chemical reduction with DTT and after 13 min of irradiation using 20 mW of 365 nm, 375 nm, 390 nm, and 500 nm wavelengths, respectively.

3.5 Conclusion

Second harmonic generation is used to monitor the photo-activated controlled release of miRNA from the surface of colloidal gold nanoparticles. The SHG signal is seen to significantly decrease as a function of UV laser irradiation time, with larger photocleaving rates occurring at higher UV laser powers on resonance with the nitrobenzyl linker, according to a single-photon photocleaving process. The photocleaving dynamics are in excellent agreement with a model using a pseudo first-order rate equation. Corresponding extinction spectroscopy shows a redshift in the plasmon resonance peak after functionalizing the GNPs with miRNA and a blueshift after illumination with the UV laser, supporting the interpretation from the time-dependent SHG results. Fluorescent measurements also indicate that the miRNA is completely removed following UV laser irradiation. These results demonstrate the successful application of sensitive real-time

measurements of photo-activated drug delivery using a model system of colloidal miRNA-functionalized gold nanoparticles in water.

3.6 References

1. Davis, M. E.; Zuckerman, J. E.; Choi, C. H. J.; Seligson, D.; Tolcher, A.; Alabi, C. A.; Yen, Y.; Heidel, J. D.; Ribas, A. Evidence of RNAi in Humans From Systemically Administered siRNA via Targeted Nanoparticles. *Nature* **2010,** *464*, 1067-1070.

2. Ivey, K. N.; Muth, A.; Arnold, J.; King, F. W.; Yeh, R.-F.; Fish, J. E.; Hsiao, E. C.; Schwartz, R. J.; Conklin, B. R.; Bernstein, H. S. MicroRNA Regulation of Cell Lineages in Mouse and Human Embryonic Stem Cells. *Cell Stem Cell* **2008,** *2*, 219-229.

3. Marson, A.; Levine, S. S.; Cole, M. F.; Frampton, G. M.; Brambrink, T.; Johnstone, S.; Guenther, M. G.; Johnston, W. K.; Wernig, M.; Newman, J. Connecting MicroRNA Genes to the Core Transcriptional Regulatory Circuitry of Embryonic Stem Cells. *Cell* **2008,** *134*, 521-533.

4. Reynolds, A.; Leake, D.; Boese, Q.; Scaringe, S.; Marshall, W. S.; Khvorova, A. Rational siRNA Design for RNA Interference. *Nat. Biotechnol.* **2004,** *22*, 326-330.

5. Lu, J.; Getz, G.; Miska, E. A.; Alvarez-Saavedra, E.; Lamb, J.; Peck, D.; Sweet-Cordero, A.; Ebert, B. L.; Mak, R. H.; Ferrando, A. A. MicroRNA Expression Profiles Classify Human Cancers. *Nature* **2005,** *435*, 834-838.

6. Volinia, S.; Calin, G. A.; Liu, C.-G.; Ambs, S.; Cimmino, A.; Petrocca, F.; Visone, R.; Iorio, M.; Roldo, C.; Ferracin, M. A MicroRNA Expression Signature of Human Solid Tumors Defines Cancer Gene Targets. *Proc. Natl. Acad. Sci. U.S.A.* **2006,** *103*, 2257-2261.

7. Schiffelers, R. M.; Ansari, A.; Xu, J.; Zhou, Q.; Tang, Q.; Storm, G.; Molema, G.; Lu, P. Y.; Scaria, P. V.; Woodle, M. C. Cancer siRNA Therapy by Tumor Selective Delivery With Ligand-Targeted Sterically Stabilized Nanoparticle. *Nucleic Acids Res.* **2004,** *32*, e149-e149.

8. Turner, J. J.; Jones, S. W.; Moschos, S. A.; Lindsay, M. A.; Gait, M. J. MALDI-TOF Mass Spectral Analysis of siRNA Degradation in Serum Confirms an RNAse A-like Activity. *Mol. Biosyst.* **2006,** *3*, 43-50.

9. Zhou, J.; Wu, J.; Hafdi, N.; Behr, J.-P.; Erbacher, P.; Peng, L. PAMAM Dendrimers for Efficient siRNA Delivery and Potent Gene Silencing. *Chem. Commun.* **2006**, 2362-2364.

10. Katas, H.; Alpar, H. O. Development and Characterisation of Chitosan Nanoparticles for siRNA Delivery. *J. Control. Release* **2006,** *115*, 216-225.

11. Hurst, S. J.; Lytton-Jean, A. K.; Mirkin, C. A. Maximizing DNA Loading on a Range of Gold Nanoparticle Sizes. *Anal. Chem.* **2006,** *78*, 8313-8318.

12. Zhang, J.; Malicka, J.; Gryczynski, I.; Lakowicz, J. R. Surface-Enhanced Fluorescence of Fluorescein-Labeled Oligonucleotides Capped on Silver Nanoparticles. *J. Phys. Chem. B* **2005,** *109,* 7643-7648.

13. Brown, P. K.; Qureshi, A. T.; Moll, A. N.; Hayes, D. J.; Monroe, W. T. Silver Nanoscale Antisense Drug Delivery System for Photoactivated Gene Silencing. *ACS Nano* **2013,** *7,* 2948-2959.

14. Qureshi, A. T.; Monroe, W. T.; Dasa, V.; Gimble, J. M.; Hayes, D. J. miR-148b–Nanoparticle Conjugates for Light Mediated Osteogenesis of Human Adipose Stromal/Stem Cells. *Biomaterials* **2013,** *34,* 7799-7810.

15. Braun, G. B.; Pallaoro, A.; Wu, G.; Missirlis, D.; Zasadzinski, J. A.; Tirrell, M.; Reich, N. O. Laser-Activated Gene Silencing via Gold Nanoshell− siRNA Conjugates. *ACS Nano* **2009,** *3,* 2007-2015.

16. Takahashi, H.; Niidome, Y.; Yamada, S. Controlled Release of Plasmid DNA From Gold Nanorods Induced by Pulsed Near-Infrared Light. *Chem. Commun.* **2005**, 2247-2249.

17. Vivero-Escoto, J. L.; Slowing, I. I.; Wu, C.-W.; Lin, V. S.-Y. Photoinduced Intracellular Controlled Release Drug Delivery in Human Cells by Gold-Capped Mesoporous Silica Nanosphere. *J. Am. Chem. Soc.* **2009,** *131,* 3462-3463.

18. Wijaya, A.; Schaffer, S. B.; Pallares, I. G.; Hamad-Schifferli, K. Selective Release of Multiple DNA Oligonucleotides From Gold Nanorods. *ACS Nano* **2008,** *3,* 80-86.

19. Ghosh, P.; Han, G.; De, M.; Kim, C. K.; Rotello, V. M. Gold Nanoparticles in Delivery Applications. *Adv. Drug Deliv. Rev.* **2008,** *60,* 1307-1315.

20. Chanana, M.; Liz-Marzan, L. M. Coating Matters: the Influence of Coating Materials on the Optical Properties of Gold Nanoparticles. *Nanophotonics* **2012,** *1,* 199-220.

21. Eustis, S.; El-Sayed, M. A. Why Gold Nanoparticles are More Precious Than Pretty Gold: Noble Metal Surface Plasmon Resonance and its Enhancement of the Radiative and Nonradiative Properties of Nanocrystals of Different Shapes. *Chem. Soc. Rev.* **2006,** *35,* 209-217.

22. Haber, L. H.; Kwok, S. J. J.; Semeraro, M.; Eisenthal, K. B. Probing the Colloidal Gold Nanoparticle/Aqueous Interface With Second Harmonic Generation. *Chem. Phys. Lett.* **2011,** *507,* 11-14.

23. Kamat, P. V. Photophysical, Photochemical and Photocatalytic Aspects of Metal Nanoparticles. *J. Phys. Chem. B* **2002,** *106,* 7729-7744.

24. Qian, X.; Peng, X.-H.; Ansari, D. O.; Yin-Goen, Q.; Chen, G. Z.; Shin, D. M.; Yang, L.; Young, A. N.; Wang, M. D.; Nie, S. In Vivo Tumor Targeting and Spectroscopic Detection With Surface-Enhanced Raman Nanoparticle Tags. *Nat. Biotechnol.* **2007,** *26,* 83-90.

25. Wustholz, K. L.; Henry, A.-I.; McMahon, J. M.; Freeman, R. G.; Valley, N.; Piotti, M. E.; Natan, M. J.; Schatz, G. C.; Duyne, R. P. V. Structure−Activity Relationships in Gold Nanoparticle Dimers and Trimers for Surface-Enhanced Raman Spectroscopy. *J. Am. Chem. Soc.* **2010,** *132*, 10903-10910.

26. Bardhan, R.; Grady, N. K.; Cole, J. R.; Joshi, A.; Halas, N. J. Fluorescence Enhancement by Au Nanostructures: Nanoshells and Nanorods. *ACS Nano* **2009,** *3*, 744-752.

27. Tam, F.; Goodrich, G. P.; Johnson, B. R.; Halas, N. J. Plasmonic Enhancement of Molecular Fluorescence. *Nano Lett.* **2007,** *7*, 496-501.

28. Karam, T. E.; Haber, L. H. Molecular Adsorption and Resonance Coupling at the Colloidal Gold Nanoparticle Interface. *J. Phys. Chem. C* **2013,** *118*, 642-649.

29. Dreaden, E. C.; Alkilany, A. M.; Huang, X. H.; Murphy, C. J.; El-Sayed, M. A. The Golden Age: Gold Nanoparticles for Biomedicine. *Chem. Soc. Rev.* **2012,** *41*, 2740-2779.

30. Oldenburg, S. J.; Averitt, R. D.; Westcott, S. L.; Halas, N. J. Nanoengineering of Optical Resonances. *Chem. Phys. Lett.* **1998,** *288*, 243-247.

31. Skrabalak, S. E.; Chen, J.; Sun, Y.; Lu, X.; Au, L.; Cobley, C. M.; Xia, Y. Gold Nanocages: Synthesis, Properties, and Applications. *Acc. Chem. Res.* **2008,** *41*, 1587-1595.

32. Ghosh, P. S.; Kim, C.-K.; Han, G.; Forbes, N. S.; Rotello, V. M. Efficient Gene Delivery Vectors by Tuning the Surface Charge Density of Amino Acid-Functionalized Gold Nanoparticles. *ACS Nano* **2008,** *2*, 2213-2218.

33. Lee, S. E.; Lee, L. P. Nanoplasmonic Gene Regulation. *Curr. Opin. Chem. Biol.* **2010,** *14*, 623-633.

34. Eisenthal, K. B. Second Harmonic Spectroscopy of Aqueous Nano-and Microparticle Interfaces. *Chem. Rev.* **2006,** *106*, 1462-1477.

35. Gonella, G.; Dai, H.-L. Second Harmonic Light Scattering from the Surface of Colloidal Objects: Theory and Applications. *Langmuir* **2013,** *30*, 2588-2599.

36. Yan, E. C. Y.; Liu, Y.; Eisenthal, K. B. New Method for Determination of Surface Potential of Microscopic Particles by Second Harmonic Generation. *J. Phys. Chem. B* **1998,** *102*, 6331-6336.

37. Knappenberger Jr, K. L.; Dowgiallo, A.-M.; Chandra, M.; Jarrett, J. W. Probing the Structure–Property Interplay of Plasmonic Nanoparticle Transducers Using Femtosecond Laser Spectroscopy. *J. Phys. Chem. Lett.* **2013,** *4*, 1109-1119.

38. Doughty, B.; Kazer, S. W.; Eisenthal, K. B. Binding and Cleavage of DNA With the Restriction Enzyme EcoR1 Using Time-Resolved Second Harmonic Generation. *Proc. Natl. Acad. Sci. U.S.A.* **2011,** *108*, 19979-19984.

39. Malin, J. N.; Holland, J. G.; Saslow, S. A.; Geiger, F. M. U(VI) Adsorption and Speciation at the Acidic Silica/Water Interface Studied by Resonant and Nonresonant Second Harmonic Generation. *J. Phys. Chem. C* **2011,** *115*, 13353-13360.

40. Walter, S. R.; Young, K. L.; Holland, J. G.; Gieseck, R. L.; Mirkin, C. A.; Geiger, F. M. Counting the Number of Magnesium Ions Bound to the Surface-Immobilized Thymine Oligonucleotides That Comprise Spherical Nucleic Acids. *J. Am. Chem. Soc.* **2013,** *135*, 17339-17348.

41. Roke, S.; Gonella, G. Nonlinear Light Scattering and Spectroscopy of Particles and Droplets in Liquids. *Annu. Rev. Phys. Chem.* **2012,** *63*, 353-378.

42. Gonella, G.; Gan, W.; Xu, B.; Dai, H.-L. The Effect of Composition, Morphology, and Susceptibility on Nonlinear Light Scattering From Metallic and Dielectric Nanoparticles. *J. Phys. Chem. Lett.* **2012,** *3*, 2877-2881.

43. Doughty, B.; Ma, Y.-Z.; Shaw, R. W. Probing Interfacial Electronic States in CdSe Quantum Dots using Second Harmonic Generation Spectroscopy. *J. Phys. Chem. C* **2015,** *119*, 2752-2760.

44. Schurer, B.; Wunderlich, S.; Sauerbeck, C.; Peschel, U.; Peukert, W. Probing Colloidal Interfaces by Angle-Resolved Second Harmonic Light Scattering. *Phys. Rev. B* **2010,** *82*, 2414041-2414044.

45. Kumal, R. R.; Karam, T. E.; Haber, L. H. Determination of the Surface Charge Density of Colloidal Gold Nanoparticles Using Second Harmonic Generation. *J. Phys. Chem. C* **2015,** *119*, 16200-16207.

46. Bai, X.; Li, Z.; Jockusch, S.; Turro, N. J.; Ju, J. Photocleavage of a 2-Nitrobenzyl Linker Bridging a Fluorophore to the 5′ end of DNA. *Proc. Natl. Acad. Sci.* **2003,** *100*, 409-413.

47. Hiemenz, P. C.; Rajagopalan, R. *Principles of Colloid and Surface Chemistry, Revised and Expanded. 3rd* ed.; CRC Press: New York, USA, 1997.

CHAPTER 4

PLASMON-ENHANCED PHOTOCLEAVING DYNAMICS IN COLLOIDAL MICRORNA FUNCTIONALIZED SILVER NANOPARTICLES USING SECOND HARMONIC GENERATION*

4.1 Introduction

Short nucleic acids such as microRNA (miRNA) and small interfering RNA (siRNA) play a significant role in post-transcriptional gene regulation, silencing and profiling.[1-3] These short RNA molecules are important in classifying and controlling tumor growth and cell differentiation, as well as other biological processes.[4-6] In order to use miRNA or siRNA as a therapeutic, it is important that the oligonucleotides are protected before entering the bloodstream to avoid degradation.[7-9] One approach for oligonucleotide protection involves modification with a bifunctional photolinker that connects to a colloidal metallic nanoparticle through a thiol bond.[10,11] Photocleaving of the photolinker then releases the active oligonucleotide from the nanoparticle surface, leading to the corresponding regulation of gene expression.[12] Although similar systems have been developed for programmed release, light activation is especially desirable because it provides a high degree of spatial and temporal control of miRNA delivery.[10,13]

Metallic nanoparticles such as gold nanoparticles (GNPs) and silver nanoparticles (SNPs) are promising for biological applications due to their biocompatibility, ease of synthesis, and convenient chemical functionalization with drug, oligonucleotide and protein molecules.[14-16] Gold and silver nanoparticles have surface plasmon resonances characterized by the coherent

oscillation of free electrons upon interaction with incident light leading to the enhancement of optical scattering and absorption processes.[17-21] These nanoparticles are also ideally suited for contrasting agents, cellular imaging and exothermic reactors.[22,23] Additionally, silver nanoparticles have wound healing antimicrobial activities,[24] demonstrate negligible cytotoxicities in small doses,[25,26] and can be utilized for drug-delivery applications in photoactivated gene silencing.[27,28] Plasmonic release of oligonucleotides has been studied from the surface of colloidal gold nanoparticles.[29-32] Previously, we have investigated the kinetics of photoactivated controlled-release of miRNA from the surface of colloidal gold nanoparticles using time-resolved second harmonic generation (SHG).[33]

Nonlinear optical spectroscopy is a powerful surface-sensitive method for probing phenomena in biology and nanotechnology.[34-40] Second harmonic generation is a nonlinear spectroscopy that is especially useful for probing the surface of colloidal nanoparticles.[41-49] In SHG, two incident photons of frequency ω combine to produce a photon of frequency 2ω . Second harmonic generation is dipole forbidden in centrosymmetric bulk media but it can be generated from the colloidal nanoparticle surface where the inversion symmetry is broken. The SHG signal from a charged interface has contributions from the second-order and third-order nonlinear susceptibilities, $\chi^{(2)}$ and $\chi^{(3)}$, respectively. The $\chi^{(2)}$ term originates from the surface-specific two-photon spectroscopy of the nanoparticle while the $\chi^{(3)}$ term depends upon the polarization of the bulk solvent molecules induced by the electric field of the nanoparticle surface. The SHG electric field E_{SHG} is proportional to the square root of the intensity of the SHG signal, with[50-58]

$$E_{SHG} = \chi^{(2)} E_\omega E_\omega + \chi^{(3)} E_\omega E_\omega \phi_0 \qquad (4.1)$$

where E_ω is the electric field of the incident laser beam with frequency ω and ϕ_0 electrostatic surface potential of nanoparticle.

In this chapter, the efficiency of light-activated release of oligonucleotides from the surface of silver, gold and polystyrene nanoparticles are compared by using SHG spectroscopy. The size of the nanoparticles are all roughly 65 nm diameter and are functionalized with miRNA-148b and a nitrobenzyl PC linker. Additional information on the miRNA functionalization of the colloidal nanoparticles is described in Appendix 2. The functionalized nanoparticles are irradiated with varying laser powers and wavelengths and are simultaneously probed by SHG from 800 nm laser pulses to study the kinetics of the photocleaving process. The probe laser itself shows no photoreleasing effect on the sample. Careful analysis of the power and wavelength dependent data shows that the photolysis is a one-photon process. By comparing the releasing rates of oligonucleotides from three different nanoparticles, it is found that the photolysis is enhanced by the plasmon of the silver nanoparticle. The SHG studies at different laser powers and wavelengths are directly compared to corresponding fluorescence quantification measurements and extinction spectra for each sample and experimental condition.

4.2 Synthesis and Characterization of Nanoparticles

The colloidal silver nanoparticles are prepared in water by reduction of silver nitrate using citrate and ascorbic acid in the presence of potassium iodide,[59] followed by miRNA functionalization. Briefly, an aqueous solution of 2.54 mL containing 5.91 mM silver nitrate, 13.4 mM sodium citrate, and 1.54 μM potassium iodide is added to 47.5 mL of 210 μM ascorbic acid in nanopure water under boiling and vigorous stirring conditions. The solution is boiled for an hour during which the color changes from colorless to light yellow resulting in relatively monodisperse, spherical, colloidal silver nanoparticles. MiRNA is functionalized to the surface of nanoparticles via a 'salt-ageing' technique as described previously,[10,33] where 2.5 μL of 0.8 μg/μL of miRNA (PC-miR-148b) labeled with a 6-TAMRA fluorophore group and modified with a thiolized

photocleaveable (PC) spacer is added to 1 mL of the silver nanoparticle solution. The samples are then left to incubate under gentle agitation conditions for a 24 h period. After incubation, 10 µL of 0.035 M sodium dodecyl sulfate (SDS) solution and 20 µL of 0.01 M phosphate-buffered saline (PBS) solution are added to each sample of colloidal nanoparticles, followed by an additional 3 h of incubation. Afterwards, three rounds of the addition of 10 µL of 2 M Tris-sodium chloride solution with 4 h of incubation between each salting step is applied. The miRNA-functionalized nanoparticles are purified via centrifugation and finally resuspended in nanopure water.

For the polystyrene sulfate nanoparticles (PSNPs), a thiol-amine cross-linker succinimidyl 4-(N-maleimidomethyl) cyclohexane-1-carboxylate (SMCC) is used to functionalize the thiolated oligo to the nanoparticle surface.[60] Here, 70 µL of 1 mg/mL SMCC in dimethyl sulfoxide solvent is added to 1 mL of the 1% amine-functionalized 60 ± 5 nm PSNPs aqueous solution. The SMCC PSNP mixture is allowed to rock overnight at room temperature, then is centrifuged and resuspended in nanopure water before adding the miRNA. The same procedure for the miRNA functionalization as described above is then followed for the PSNP sample.

The nanoparticles are characterized using dynamic light scattering (DLS), transmission electron microscopy (TEM), zeta potential, fluorimetry and extinction spectroscopy measurements. Representative TEM images of the silver nanoparticles before and after miRNA functionalization are shown in Figures 4.1 (a) and (b), respectively. From a survey of nanoparticle images, the average nanoparticle diameter is determined to be 65 ± 7.5 nm. Using dynamic light scattering, the hydrodynamic diameter of the SNPs before miRNA functionalization is measured to be 66 ± 18 nm, and the hydrodynamic diameter increases to 127 ± 25 nm after miRNA functionalization. Figure 4.2 shows the experimental extinction spectrum of the colloidal silver nanoparticles (red solid line) when compared with a Mie theory fit (black dotted line) using a

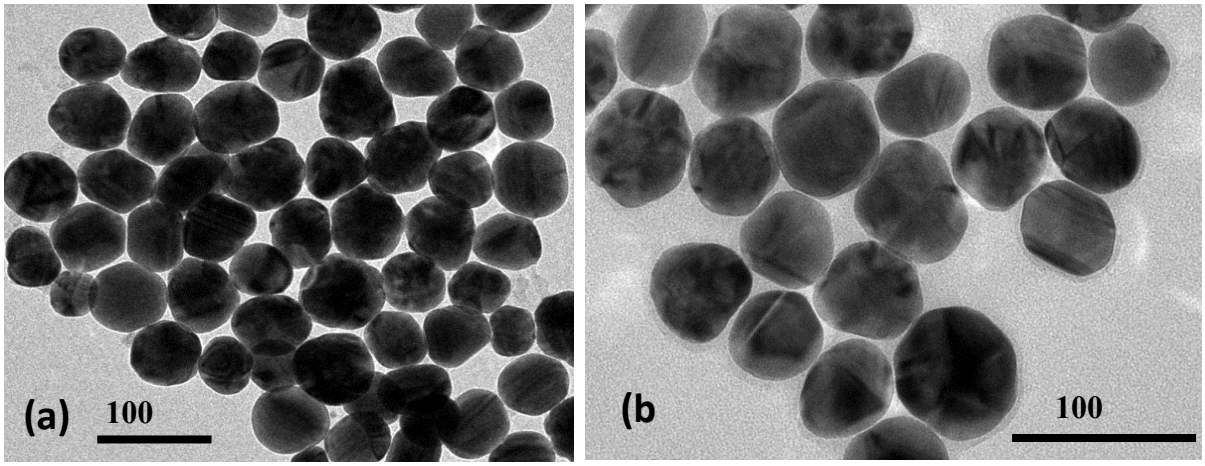

Figure 4.1. Representative TEM images of (a) silver nanoparticles having size 65 ± 7.5 nm and (b) miRNA-functionalized silver nanoparticles

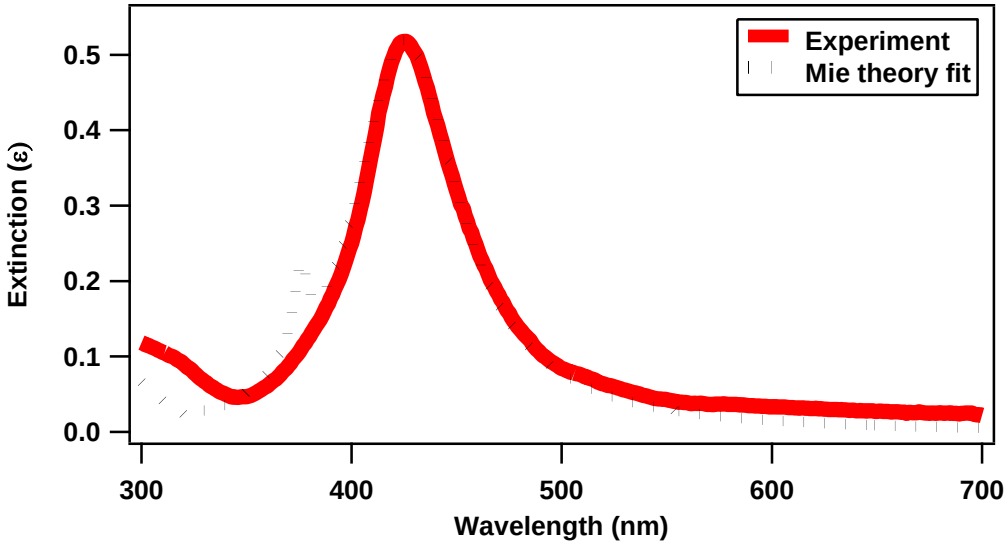

Figure 4.2. Extinction spectra of 65 ± 7.5 nm colloidal silver nanoparticles in water (red line) compared with Mie theory (dotted black line).

concentration of 9.55 x 10^9 nanoparticles/mL. The localized surface plasmon peak for silver nanoparticles is observed at 424 nm. Figure 4.3 displays the electrophoretic mobility of nanoparticles before and after miRNA functionalization. The electrophoretic mobility of the SNPs is measured to be (−2.60 ± 0.53) x 10^{-8} m^2/Vs with a corresponding zeta potential of −49.80 ± 10.17 mV using Huckel's approximation.[33,61] The electrophoretic mobility of the miRNA-

functionalized PSNPs is measured to be (−3.86 ± 0.60) x 10^{-8} m^2/Vs with a corresponding zeta potential of −74.80 ± 11.40 mV.

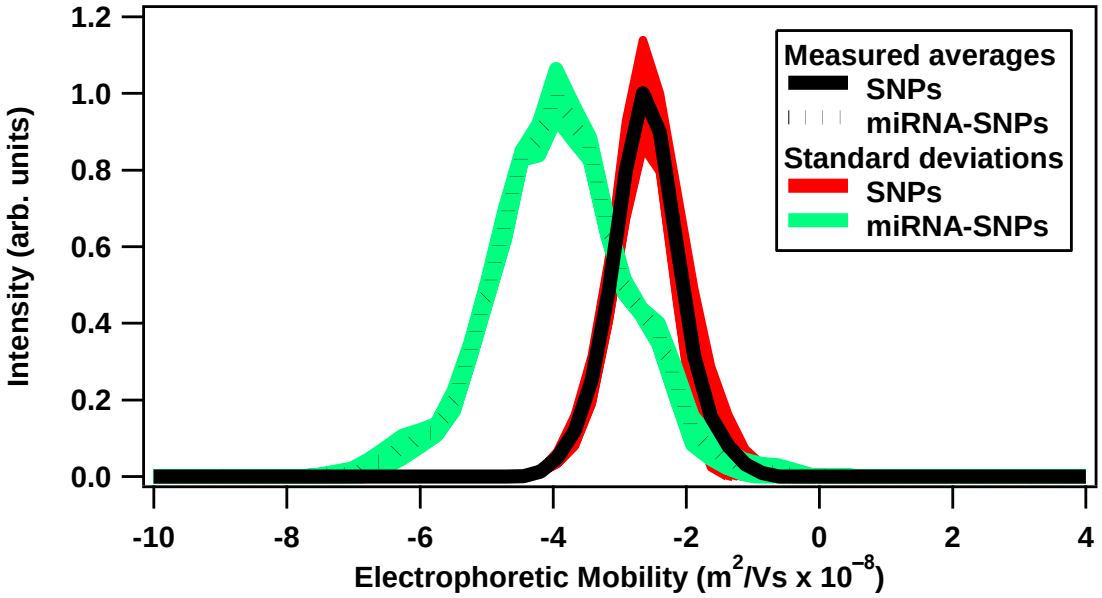

Figure 4.3. Electrophoretic mobility plot of silver nanoparticles before and after miRNA functionalization showing the measured averages (solid and dotted black lines, respectively) and corresponding standard deviations (red and green areas, respectively).

4.3 Experimental Setup

The controlled release of miRNAs from the surface of colloidal nanoparticles is performed using an experimental setup which has been previously described.[39] Briefly, the experimental setup consists of an ultrafast laser system, an optical setup and a high sensitive charged-coupled device (CCD) detector connected to a monochromator. A Titanium:sapphire oscillator laser with 70 fs pulses centered at 800 nm at an 80 MHz repetition rate and an average power of 2.6 W is used. A portion of the oscillator beam passes through a beam splitter to seed the amplifier laser and the remaining portion is used for the SHG measurements. An amplified laser (75 fs, 800 nm, 10 kHz, 7W) pumps an optical parametric amplifier (OPA) to generate the wavelength-tunable photocleaving irradiation beam with 100 fs pulses at a 10 kHz repetition rate. For SHG

measurements, the 800 nm probe laser from the oscillator is attenuated to an average power of 790 mW before being focused to a 1 cm x 1 cm quartz cuvette containing the sample at a concentration of 8.3 x 10^9 nanoparticles/mL. The photocleaving irradiation beam at the desired wavelength and power is directed to the sample at 90° with respect to the SHG probe laser. The SHG from the nanoparticle sample is measured as of function of time using different photocleaving irradiation wavelengths and average powers. An integrated Labview program controls a magnetic stir bar and a beam block to open and shut every 30 s in synchronization with automated data acquisition for background-subtracted time-dependent SHG measurements.

4.4 Results and Discussion

The photocleaving controlled release of miRNA from the surface of silver nanoparticles and polystyrene nanoparticles are measured in real time using second harmonic generation. The obtained results are compared with our previous studies on miRNA-functionalized gold nanoparticles.[33] Representative SHG spectra of SNPs and miRNA-functionalized SNPs are shown in Figure 4.4a. The SHG peak from the 800 nm probe laser is located at 400 nm, as expected, with full width half maximum of 4.5 nm. The small signal at longer wavelengths is due to the two-photon fluorescence from the SNPs. The SHG signal intensity from miRNA-functionalized SNPs is approximately four times higher than the corresponding SHG signal from the SNPs using the same laser conditions and nanoparticle concentrations. The higher SHG signal in the miRNA-functionalized SNPs is mainly attributed to the negatively-charged phosphate groups of the oligonucleotides which increase the surface charge density magnitude and the corresponding surface potential, resulting in a larger $\chi^{(3)}$ term. This interpretation is consistent with previous work and with our earlier results on miRNA-functionalized GNPs.[10,33,58,62] The 6-TAMRA fluorophore has negligible contribution to the SHG signal because it has negligible absorption near the 800 nm

probe and 400 nm SHG wavelengths. Figure 4.4b shows representative SHG spectra from the miRNA-functionalized SNPs at different UV-irradiation times of 0, 90 and 800 s using 365 nm irradiation with a 20 mW average power.

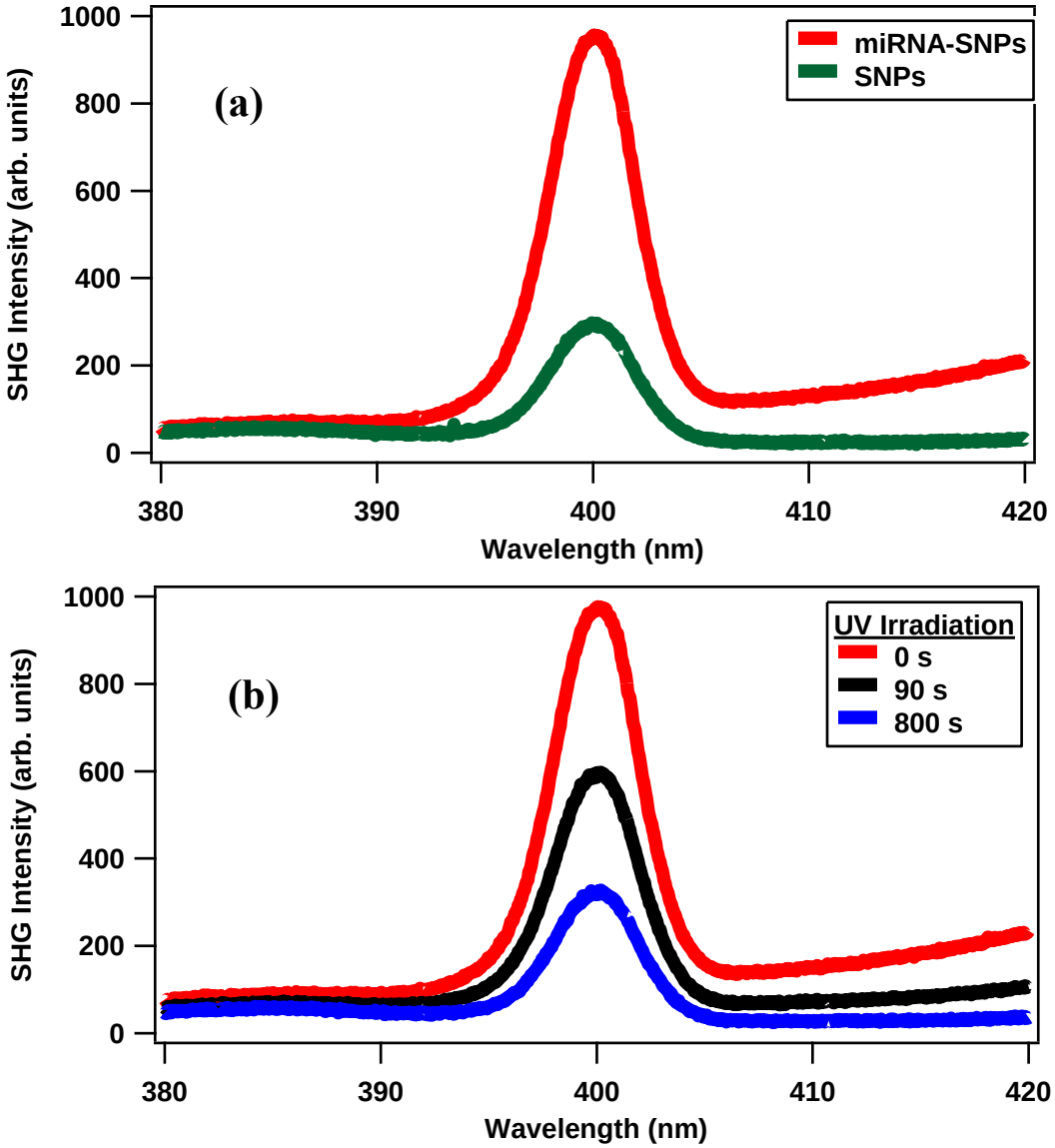

Figure 4.4. (a) SHG spectra of the colloidal silver nanoparticles and the miRNA-functionalized silver nanoparticles. (b) SHG spectra of miRNA-functionalized colloidal silver nanoparticle sample after different UV irradiation times using 365 nm with 20 mW average power. The probe laser is fixed at 800 nm.

The decrease in SHG intensity under increasing UV-irradiation time is due to the photocleaving of miRNA from the colloidal SNP surface, resulting in a decrease of the nanoparticle surface charge density magnitude and a smaller $\chi^{(3)}$ term.

The results from control experiments are shown in Figure 4.5a where the variation of the SHG intensity as a function of the UV-irradiation time is displayed for the SNPs and the

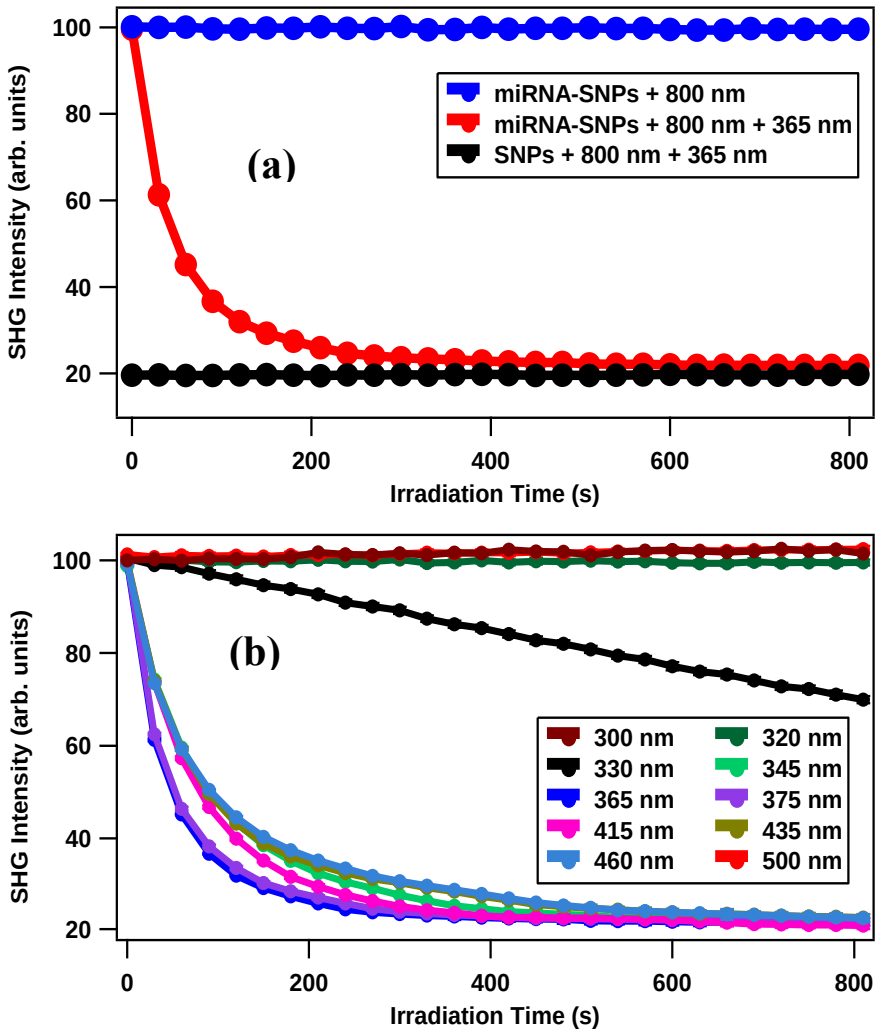

Figure 4.5. (a) For control experiments, the time-dependent SHG signal remains constant for both the miRNA-functionalized SNPs using the 800 nm probe laser only (blue data) and the SNPs using the 800 nm probe and the UV laser at 365 nm (black data). The SHG of the miRNA-functionalized SNPs decreases as a function of time under irradiation with the UV laser at 365 nm (red data). (b) Time-dependent SHG measurements of the miRNA-functionalized SNPs using different UV and visible laser wavelengths at 20 mW average power to determine the photocleaving dynamics.

miRNA-functionalized SNPs. The SHG signal from the miRNA-functionalized SNP sample remains constant over time using the 800 nm probe laser, indicating that no photocleaving occurs from the probe laser alone. Similarly, the SHG signal from the SNP sample remains constant over time when both the 800 nm probe laser and the UV laser at 365 nm with an average power of 20 mW are used. However, the SHG intensity from the miRNA-functionalized SNP sample decreases and asymptotically reaches a minimum value when using both the probe laser and the UV laser. The minimum of the time-dependent SHG signal from the miRNA-functionalized under UV irradiation is equal to the corresponding signal of the SNPs, indicating complete photocleaving of oligonucleotides from the surface of nanoparticles.

A wavelength-dependent study on the photocleaving process is shown in Figure 4.5b. The error bars are included in Figures 4.5a and 4.5b, but are mostly smaller than the data points. The irradiation laser wavelength is varied from 320 nm to 500 nm and time-dependence of the SHG signal is measured to determine the photocleaving rate under a constant average irradiation laser power of 20 mW. The fastest decay of the SHG signal is observed at 365 nm irradiation, in agreement with previous measurements on miRNA-functionalized gold nanoparticles,[33] indicating the photocleaving peak resonance. Relatively rapid photocleaving kinetics are also observed at irradiation wavelengths between 345 nm and 460 nm. Much slower photocleaving is observed using irradiation at 330 nm, while almost no photocleaving is observed with irradiation at 500 nm and 320 nm, which are far from the photocleaving resonance.

The wavelength-dependent photocleaving rates in the plasmonic miRNA-functionalized SNPs are compared with corresponding measurements in the non-plasmonic miRNA-functionalized polystyrene nanoparticles in order to determine the role of plasmonic enhancement of the photocleaving process. The time-dependent SHG signals from the miRNA-functionalized

PSNPs are shown in Figure 4.6 under varying irradiation wavelengths from 300 nm to 500 nm at 20 mW. The photocleaving rates from the miRNA-functionalized PSNPs are lower than the corresponding photocleaving rates from the SNP sample.

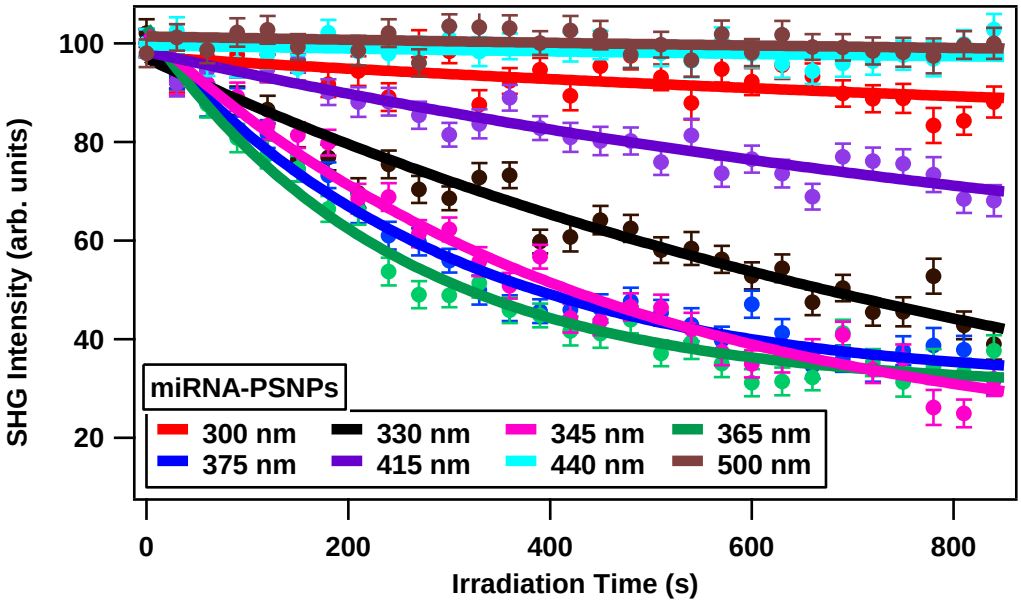

Figure 4.6. Time-dependent SHG signals showing the photocleaving of miRNA-functionalized polystyrene nanoparticles using different irradiation wavelengths.

The photocleaving rate constants at different irradiation wavelengths are determined for the miRNA-functionalized SNPs and PSNPs by fitting the SHG data using a pseudo first-order exponential rate equation, as described previously.[33] The SHG electric field can be described by the equation $E_{SHG} = A + B\,[C]$, where A is an offset, B is a proportionality constant and $[C]$ is the cumulative concentration of miRNA attached to the surface of nanoparticles. As noted earlier, the change in E_{SHG} as a function of attached miRNA at the nanoparticle surface is attributed mainly to the surface charge density and the resulting $\chi^{(3)}$ term.[33,58,62] Under the UV irradiation-induced photocleaving, the attached miRNA concentration should exponentially decay in time t according to the equation, $[C](t) = [C]_0\, e^{-k't}$, where $[C]_0$ is the initial concentration of miRNA attached to the nanoparticle surface and the pseudo first-order rate constant k' is linearly proportional to

the UV laser intensity, assuming that the photocleaving is a single-photon process.

The resulting rate constants for the miRNA-functionalized SNP and PSNP samples determined from the pseudo first-order fits are plotted as a function of the irradiation wavelength in Figure 4.7. Both miRNA-functionalized nanoparticles show a maximum rate of photocleaving at 365 nm due to the characteristic resonance peak of the photocleaving process. The miRNA-functionalized SNPs show greatly enhanced photocleaving rate constants compared to the PSNPs over the irradiation wavelengths from 350 nm to 450 nm due to plasmon enhancement. The plasmon resonance of the SNPs cause enhanced optical fields near the nanoparticle surface leading to plasmon-enhanced photocleaving over the wavelength range of the SNP plasmon resonance, which directly overlaps with the photocleaving resonance of the nitrobenzyl linker. The PSNP sample has no associated plasmon resonance, so its rate constants are attributed to the nitrobenzyl linker alone.

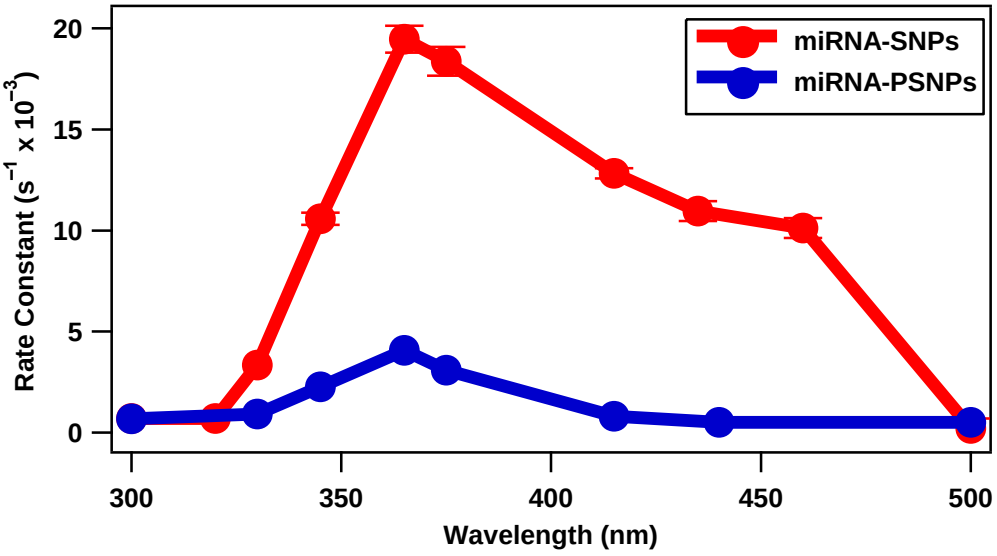

Figure 4.7. The photocleaving rate constants of the miRNA-functionalized SNPs and PSNPs at different irradiation wavelengths using 20 mW average power.

The power-dependent photocleaving of the miRNA-functionalized SNPs and PSNPs is also studied for additional insight. Figure 4.8a shows the SHG electric field from miRNA-functionalized SNPs as a function of UV irradiation time using 365 nm at different UV laser powers. The rate constants from the miRNA-functionalized SNPs obtained at the laser powers of 15, 25, 35, 45, 55 and 75 mW are $(4.9 \pm 0.1) \times 10^{-3}$, $(8.6 \pm 0.2) \times 10^{-3}$, $(12.4 \pm 0.6) \times 10^{-3}$, $(16.1 \pm 0.3) \times 10^{-3}$, $(18.0 \pm 0.2) \times 10^{-3}$ and $(26.3 \pm 0.6) \times 10^{-3}$ s^{-1}, respectively. Corresponding results from the miRNA-functionalized PSNPs are shown in Appendix 2. The photocleaving rate constants for the miRNA-functionalized SNPs and PSNPs are plotted as a function of the UV laser average powers in Figure 4.8b. The error bars are included in Figures 4.8a and 4.8b, but are mostly smaller than the data points. The previously obtained GNP data[33] are included for direct comparison. The linear variation of the rate constants as a function of the UV laser power is consistent with a pseudo first-order kinetics model, indicating that the photocleaving is a one-photon process for all nanoparticle samples investigated. The slopes obtained for miRNA-functionalized SNPs and PSNPs are $(3.48 \pm 0.12) \times 10^{-4}$ s^{-1} mW^{-1} and $(5.45 \pm 0.28) \times 10^{-5}$ s^{-1} mW^{-1}, respectively, with corresponding y-intercepts of $(1.3 \pm 6.0) \times 10^{-4}$ s^{-1} and $(0.2 \pm 1.4) \times 10^{-4}$ s^{-1}, respectively. Here, the y-intercepts are equal to zero to within experimental uncertainty, in agreement with the observation that no photocleaving occurs without UV irradiation. The ratios of the slopes of the change in the rate constants under changing UV laser powers for the SNPs and GNPs compared to the PSNPs provide a direct method for determining the plasmon enhancement factors. Using this method, the plasmon enhancement factors for photocleaving in the SNPs and GNPs are 6.4 ± 0.4 and 2.3 ± 0.2, respectively. The SNP enhancement is much higher because its plasmon resonance directly overlaps with the photocleaving resonance wavelength of the nitrobenzyl linker. The GNP plasmon is centered near 540 nm and its extinction near 365 nm is

dominated by the electronic interband transition,[45, 63] causing a decrease in the relative optical field enhancement.

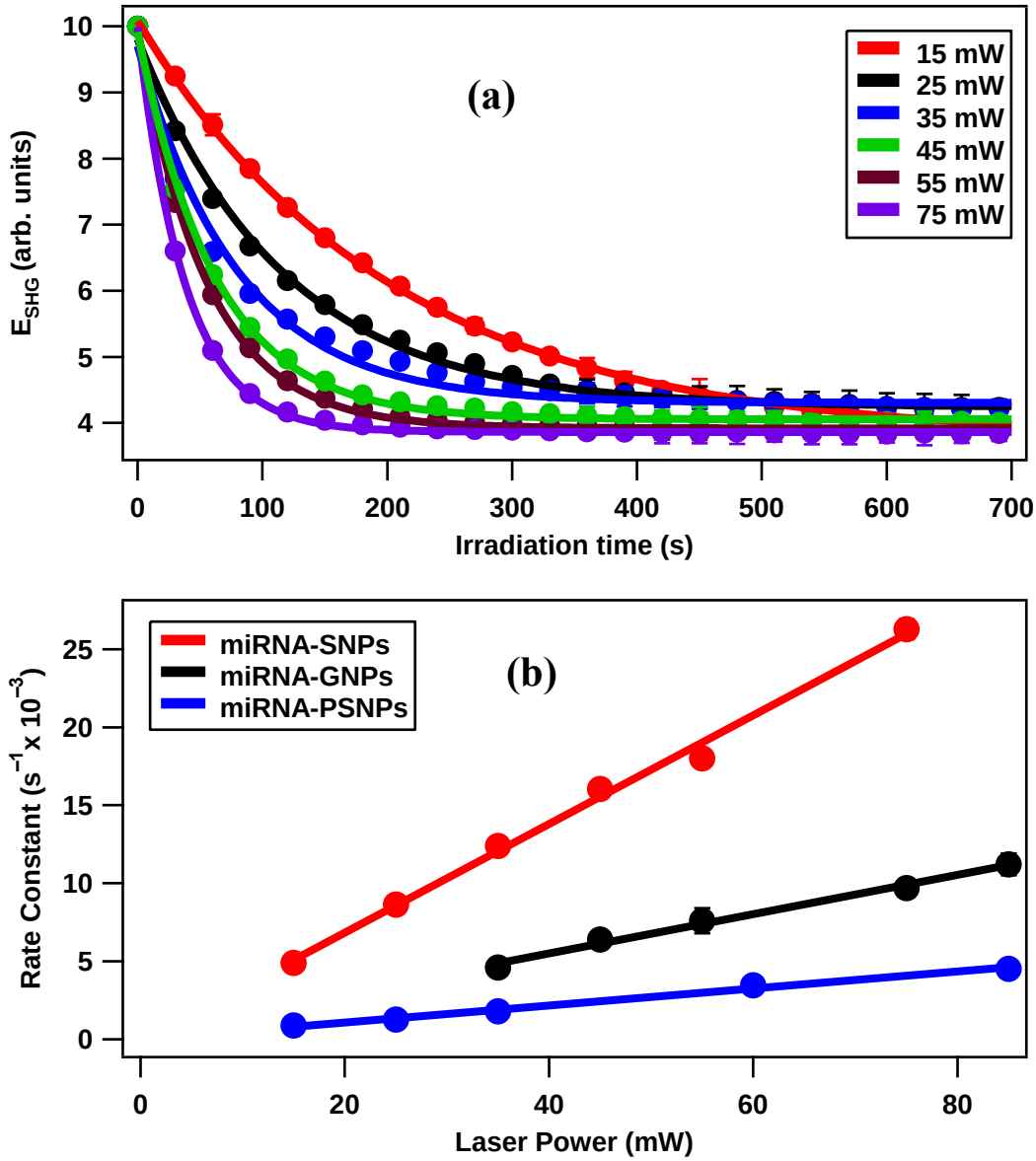

Figure 4.8. (a) Measured SHG electric field from miRNA-functionalized SNPs as a function of irradiation time with 365 nm at different UV laser average powers with corresponding exponential fits. (b) The photocleaving rate constants for the miRNA-functionalized SNPs and PSNPs under varying UV laser powers. The linear variation with laser power indicates a one-photon photocleaving process for all nanoparticle samples. Previous results from GNPs are included for comparison.

Additional characterization measurements are performed to confirm the analysis obtained from the SHG results. Figure 4.9 shows the extinction spectra of the SNPs, the miRNA-functionalized SNPs, and the miRNA-functionalized SNPs after laser irradiation with 330 nm, 365 nm and 435 nm at an average power of 20 mW for 14 min. The plasmon peak of the SNP sample shifts from 424 nm to 435 nm after functionalization with miRNA due to the change in the dielectric constant at the nanoparticle surface. The plasmon peak of the miRNA-functionalized SNPs blue shifts back towards the SNP spectrum under UV laser irradiation. After 365 nm irradiation, the miRNA-functionalized SNPs plasmon spectrum closely matches the SNP spectrum, indicating complete photocleaving. The miRNA- functionalized SNP spectra deviate from the SNP after 330 nm and 435 nm irradiation, indicating incomplete photocleaving.

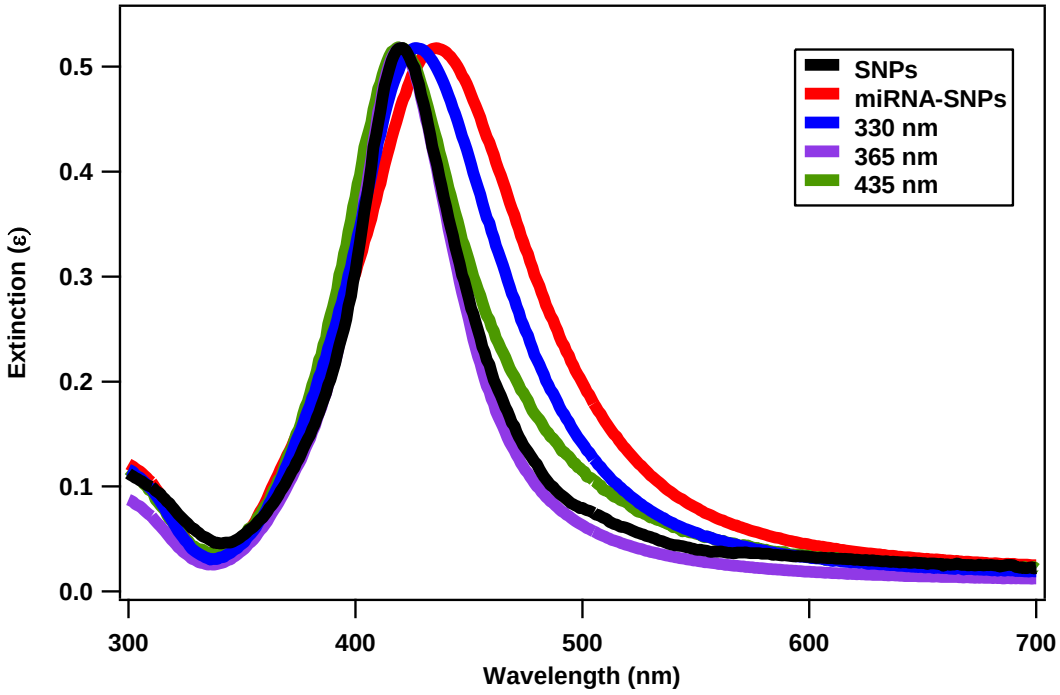

Figure 4.9. Extinction spectra of the SNPs, the miRNA-functionalized SNPs, and the miRNA-functionalized SNPs after laser irradiation with different wavelengths.

Quantification of the miRNA released from the nanoparticle surface is obtained from fluorescence measurements of the 6-TAMARA labeling fluorophore in the centrifuged

supernatants following laser irradiation or chemical reduction according to the procedure described previously.[33] Figure 4.10 shows the fluorescent signal from the miRNA-functionalized SNPs after 14 min irradiation with 20 mW average power for wavelengths ranging from 300 nm to 800 nm. These measurements are compared to the supernatants after the addition of dithiothreitol (DTT) for compete reduction and chemical detachment of the miRNA. Irradiation with 365 nm shows maximum photocleaving corresponding to complete release, to within experimental uncertainty. Irradiation at other wavelengths show partial photocleaving, with negligible photocleaving at 300 nm and 800 nm, in agreement with the SHG measurements. The concentration of the SNPs is determined by inductively coupled plasma optical emission spectroscopy (ICP-OES). When combined with the fluorimetry measurements, the average oligonucleotide surface densities are determined to be $(5.92 \pm 0.76) \times 10^{-3}$ and $(6.18 \pm 0.45) \times 10^{-3}$ oligo/nm^2 for the SNPs and PSNPs, respectively, corresponding to coverages of 79 ± 10 oligo/nanoparticle and 70 ± 5 oligo/nanoparticle, respectively.

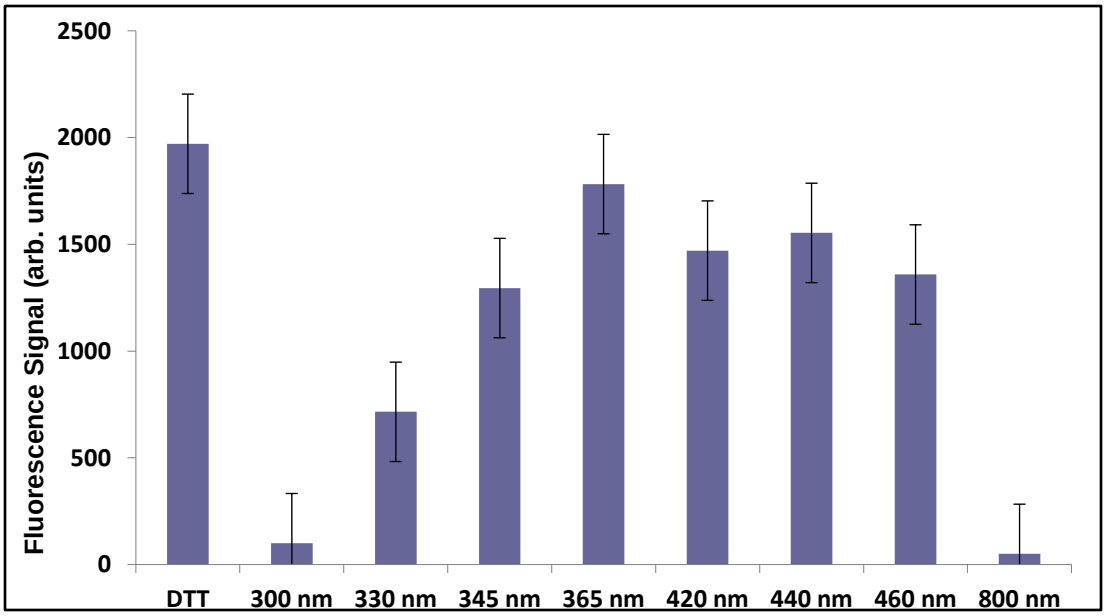

Figure 4.10. Fluorescence measurements of miRNA-functionalized SNPs after DTT reduction and after using laser irradiation at different wavelengths varying from 300 nm to 800 nm.

4.5 Conclusion

The photocleaving dynamics from model oligonucleotide therapeutic delivery systems are studied using time-dependent second harmonic generation measurements. The photocleaving rates from the surface of colloidal miRNA-functionalized silver nanoparticles and polystyrene nanoparticles in water are obtained using different laser irradiation wavelengths and powers. The photocleaving rate is a maximum using the irradiation wavelength of 365 nm, which is on resonance with the nitrobenzyl linker. A linear variation of the photocleaving rate constant under varying irradiation laser powers is observed, demonstrating that the associated kinetics are described by a one-photon process. The miRNA-functionalized silver nanoparticles show a plasmon enhancement factor of 6.4 ± 0.4 when compared to the photocleaving rates from corresponding measurements in the polystyrene nanoparticles. Electrophoretic mobility, extinction spectroscopy and fluorimetry measurements are used to verify the analysis of the SHG results, which are compared to previous investigations on gold nanoparticles. Second harmonic generation is shown to be a very sensitive nonlinear optical technique for investigating real-time plasmon-enhanced photocleaving for potential drug-delivery systems.

4.6 References

1. Bartel, D. P. MicroRNAs: Genomics, Biogenesis, Mechanism, and Function. *Cell* **2004,** *116*, 281-297.

2. Lu, J.; Getz, G.; Miska, E. A.; Alvarez-Saavedra, E.; Lamb, J.; Peck, D.; Sweet-Cordero, A.; Ebert, B. L.; Mak, R. H.; Ferrando, A. A. MicroRNA Expression Profiles Classify Human Cancers. *Nature* **2005,** *435*, 834-838.

3. Macha, M. A.; Seshacharyulu, P.; Krishn, S. R.; Pai, P.; Rachagani, S.; Jain, M.; Batra, S. K. MicroRNAs (miRNAs) as Biomarker (s) for Prognosis and Diagnosis of Gastrointestinal (GI) Cancers. *Curr. Pharm. Des.* **2013,** *20*, 5287-5297.

4. Greene, S. B.; Herschkowitz, J. I.; Rosen, J. M. Small Players With Big Roles: MicroRNAs as Targets to Inhibit Breast Cancer Progression. *Curr. Drug. Targets* **2010,** *11*, 1059-1073.

5. Reynolds, A.; Leake, D.; Boese, Q.; Scaringe, S.; Marshall, W. S.; Khvorova, A. Rational siRNA Design for RNA Interference. *Nat. Biotechnol.* **2004,** *22*, 326-330.

6. Zhang, B.; Pan, X.; Cobb, G. P.; Anderson, T. A. MicroRNAs as Oncogenes and Tumor Suppressors. *Dev. Biol.* **2007,** *302*, 1-12.

7. Muro, S. Challenges in Design and Characterization of Ligand-Targeted Drug Delivery Systems. *J. Control. Release* **2012,** *164*, 125-137.

8. Verma, A.; Uzun, O.; Hu, Y.; Hu, Y.; Han, H.-S.; Watson, N.; Chen, S.; Irvine, D. J.; Stellacci, F. Surface-Structure-Regulated Cell-Membrane Penetration by Monolayer-Protected Nanoparticles. *Nat. Mater.* **2013,** *12*, 376-376.

9. Zhou, J.; Wu, J.; Hafdi, N.; Behr, J.-P.; Erbacher, P.; Peng, L. PAMAM Dendrimers for Efficient siRNA Delivery and Potent Gene Silencing. *Chem. Commun.* **2006,** *22*, 2362-2364.

10. Qureshi, A. T.; Monroe, W. T.; Dasa, V.; Gimble, J. M.; Hayes, D. J. miR-148b–Nanoparticle Conjugates for Light Mediated Osteogenesis of Human Adipose Stromal/Stem Cells. *Biomaterials* **2013,** *34*, 7799-7810.

11. Zhang, J.; Malicka, J.; Gryczynski, I.; Lakowicz, J. R. Surface-Enhanced Fluorescence of Fluorescein-Labeled Oligonucleotides Capped on Silver Nanoparticles. *J. Phys. Chem. B* **2005,** *109*, 7643-7648.

12. Vivero-Escoto, J. L.; Slowing, I. I.; Wu, C.-W.; Lin, V. S.-Y. Photoinduced Intracellular Controlled Release Drug Delivery in Human Cells by Gold-Capped Mesoporous Silica Nanosphere. *J. Am. Chem. Soc.* **2009,** *131*, 3462-3463.

13. Brown, P. K.; Qureshi, A. T.; Moll, A. N.; Hayes, D. J.; Monroe, W. T. Silver Nanoscale Antisense Drug Delivery System for Photoactivated Gene Silencing. *ACS Nano* **2013,** *7*, 2948-2959.

14. Thakor, A. S.; Gambhir, S. S. Nanooncology: the Future of Cancer Diagnosis and Therapy. *CA: a cancer journal for clinicians* **2013,** *63*, 395-418.

15. Couvreur, P. Nanoparticles in drug delivery: past, present and future. *Adv. Drug Deliv. Rev.* **2013,** *65*, 21-23.

16. Dreaden, E. C.; Alkilany, A. M.; Huang, X.; Murphy, C. J.; El-Sayed, M. A. The Golden Age: Gold Nanoparticles for Biomedicine. *Chem. Soc. Rev.* **2012,** *41*, 2740-2779.

17. Thomas, K. G.; Kamat, P. V. Chromophore-Functionalized Gold Nanoparticles. *Acc. Chem. Res.* **2003,** *36*, 888-898.

18. Jain, P. K.; Lee, K. S.; El-Sayed, I. H.; El-Sayed, M. A. Calculated Absorption and Scattering Properties of Gold Nanoparticles of Different Size, Shape, and Composition: Applications in Biological Imaging and Biomedicine. *J. Phys. Chem. B* **2006,** *110*, 7238-7248.

19. Kelly, K. L.; Coronado, E.; Zhao, L. L.; Schatz, G. C. The Optical Properties of Metal Nanoparticles: the Influence of Size, Shape, and Dielectric Environment. *J. Phys. Chem. B* **2003,** *107*, 668-677.

20. Yang, X.; Yang, M.; Pang, B.; Vara, M.; Xia, Y. Gold Nanomaterials at Work in Biomedicine. *Chem. Rev.* **2015,** *115*, 10410-10488.

21. Yguerabide, J.; Yguerabide, E. E. Light-Scattering Submicroscopic Particles as Highly Fluorescent Analogs and Their Use as Tracer Labels in Clinical and Biological Applications: I. Theory. *Anal. Biochem.* **1998,** *262*, 137-156.

22. Hong, R.; Han, G.; Fernández, J. M.; Kim, B.-j.; Forbes, N. S.; Rotello, V. M. Glutathione-Mediated Delivery and Release Using Monolayer Protected Nanoparticle Carriers. *J. Am. Chem. Soc.* **2006,** *128*, 1078-1079.

23. You, J.; Zhang, G.; Li, C. Exceptionally High Payload of Doxorubicin in Hollow Gold Nanospheres for Near-Infrared Light-Triggered Drug Release. *ACS Nano* **2010,** *4*, 1033-1041.

24. Kim, J. S.; Kuk, E.; Yu, K. N.; Kim, J.-H.; Park, S. J.; Lee, H. J.; Kim, S. H.; Park, Y. K.; Park, Y. H.; Hwang, C.-Y. Antimicrobial Effects of Silver Nanoparticles. *Nanomed-Nanotechnol* **2007,** *3*, 95-101.

25. Kim, Y. S.; Kim, J. S.; Cho, H. S.; Rha, D. S.; Kim, J. M.; Park, J. D.; Choi, B. S.; Lim, R.; Chang, H. K.; Chung, Y. H. Twenty-Eight-Day Oral Toxicity, Genotoxicity, and Gender-Related Tissue Distribution of Silver Nanoparticles in Sprague-Dawley Rats. *Inhal. Toxicol.* **2008,** *20*, 575-583.

26. Tiwari, D. K.; Jin, T.; Behari, J. Dose-Dependent In-Vivo Toxicity Assessment of Silver Nanoparticle in Wistar Rats. *Toxicol. Mech. Meth.* **2011,** *21*, 13-24.

27. Qureshi, A. T.; Monroe, W. T.; Lopez, M. J.; Janes, M. E.; Dasa, V.; Park, S.; Amirsadeghi, A.; Hayes, D. J. Biocompatible/Bioabsorbable Silver Nanocomposite Coatings. *J. Appl. Polym. Sci.* **2011,** *120*, 3042-3053.

28. Qureshi, A. T.; Terrell, L.; Monroe, W. T.; Dasa, V.; Janes, M. E.; Gimble, J. M.; Hayes, D. J. Antimicrobial Biocompatible Bioscaffolds for Orthopaedic Implants. *J. Tissue Eng. Regen. Med.* **2014,** *8*, 386-395.

29. Simoncelli, S.; de Alwis Weerasekera, H.; Fasciani, C.; Boddy, C. N.; Aramendia, P. F.; Alarcon, E. I.; Scaiano, J. C. Thermoplasmonic ssDNA Dynamic Release from Gold Nanoparticles Examined with Advanced Fluorescence Microscopy. *J. Phys. Chem. Lett.* **2015,** *6*, 1499-1503.

30. Poon, L.; Zandberg, W.; Hsiao, D.; Erno, Z.; Sen, D.; Gates, B. D.; Branda, N. R. Photothermal Release of Single-Stranded DNA From the Surface of Gold Nanoparticles Through Controlled Denaturating and Au− S Bond Breaking. *ACS Nano* **2010,** *4*, 6395-6403.

31. Huschka, R.; Neumann, O.; Barhoumi, A.; Halas, N. J. Visualizing Light-Triggered Release of Molecules Inside Living Cells. *Nano Lett.* **2010,** *10*, 4117-4122.

32. Thibaudau, F. Ultrafast Photothermal Release of DNA From Gold Nanoparticles. *J. Phys. Chem. Lett.* **2012,** *3*, 902-907.

33. Kumal, R. R.; Landry, C. R.; Abu-Laban, M.; Hayes, D. J.; Haber, L. H. Monitoring the Photocleaving Dynamics of Colloidal MicroRNA-Functionalized Gold Nanoparticles Using Second Harmonic Generation. *Langmuir* **2015,** *31*, 9983-9990.

34. Chase, H. M.; Psciuk, B. T.; Strick, B. L.; Thomson, R. J.; Batista, V. S.; Geiger, F. M. Beyond Local Group Modes in Vibrational Sum Frequency Generation. *J. Phys. Chem. A* **2015,** *119*, 3407-3414.

35. Liu, X.; Biswas, S.; Jarrett, J. W.; Poutrina, E.; Urbas, A.; Knappenberger, K. L.; Vaia, R. A.; Nealey, P. F. Deterministic Construction of Plasmonic Heterostructures in Well-Organized Arrays for Nanophotonic Materials. *Adv. Mater.* **2015,** *27*, 7314-7319.

36. Czaplicki, R.; Mäkitalo, J.; Siikanen, R.; Husu, H.; Lehtolahti, J.; Kuittinen, M.; Kauranen, M. Second-Harmonic Generation from Metal Nanoparticles: Resonance Enhancement versus Particle Geometry. *Nano Lett.* **2014,** *15*, 530-534.

37. Capretti, A.; Pecora, E. F.; Forestiere, C.; Dal Negro, L.; Miano, G. Size-Dependent Second-Harmonic Generation From Gold Nanoparticles. *Phys. Rev. B* **2014,** *89*, 125414.

38. Dadap, J. I.; Eisenthal, K. B. Probing the Relative Orientation of Molecules Bound to DNA by Second-Harmonic Generation. *J. Phys. Chem. B* **2014,** *118*, 14366-14372.

39. Kumal, R. R.; Karam, T. E.; Haber, L. H. Determination of the Surface Charge Density of Colloidal Gold Nanoparticles Using Second Harmonic Generation. *J. Phys. Chem. C* **2015,** *119*, 16200-16207.

40. Leone, S. R.; Voth, G. A.; Dai, H.-L. Experimental and Theoretical Probing of Molecular Dynamics at Catalytic and Ionic Liquid Interfaces; DTIC Document: 2014.

41. Daniel, J.; Bondu, F.; Adamietz, F.; Blanchard-Desce, M.; Rodriguez, V. Interfacial Organization in Dipolar Dye-Based Organic Nanoparticles Probed by Second-Harmonic Scattering. *ACS Photonics* **2015,** *2*, 1209-1216.

42. Doughty, B.; Ma, Y.-Z.; Shaw, R. W. Probing Interfacial Electronic States in CdSe Quantum Dots Using Second Harmonic Generation Spectroscopy. *J. Phys. Chem. C* **2015,** *119*, 2752-2760.

43. Svechkarev, D.; Kolodezny, D.; Mosquera-Vázquez, S.; Vauthey, E. Complementary Surface Second Harmonic Generation and Molecular Dynamics Investigation of the Orientation of Organic Dyes at a Liquid/Liquid Interface. *Langmuir* **2014,** *30*, 13869-13876.

44. Karam, T. E.; Haber, L. H. Molecular Adsorption and Resonance Coupling at the Colloidal Gold Nanoparticle Interface. *J. Phys. Chem. C* **2013,** *118*, 642-649.

45. Karam, T. E.; Smith, H. T.; Haber, L. H. Enhanced Photothermal Effects and Excited-State Dynamics of Plasmonic Size-Controlled Gold–Silver–Gold Core–Shell–Shell Nanoparticles. *J. Phys. Chem. C* **2015,** *119*, 18573-18580.

46. Haber, L. H.; Kwok, S. J. J.; Semeraro, M.; Eisenthal, K. B. Probing the Colloidal Gold Nanoparticle/Aqueous Interface With Second Harmonic Generation. *Chem. Phys. Lett.* **2011,** *507*, 11-14.

47. Haber, L. H.; Eisenthal, K. B. Molecular Excited-State Relaxation Dynamics at the Colloidal Microparticle Interface Monitored with Pump–Probe Second Harmonic Generation. *J. Phys. Chem. B* **2012,** *117*, 4249-4253.

48. Xu, B.; Gonella, G.; DeLacy, B. G.; Dai, H.-L. Adsorption of Anionic Thiols on Silver Nanoparticles. *J. Phys. Chem. C* **2015,** *119*, 5454-5461.

49. Gan, W.; Gonella, G.; Zhang, M.; Dai, H.-L. Communication: Reactions and Adsorption at the Surface of Silver Nanoparticles Probed by Second Harmonic Generation. *J. Chem. Phys* **2011,** *134*, 041104.

50. Shen, Y. R. *The Principles of Nonlinear Optics*. Wiley: Hoboken, USA, 2003.

51. Valev, V. Characterization of Nanostructured Plasmonic Surfaces With Second Harmonic Generation. *Langmuir* **2012,** *28*, 15454-15471.

52. Smirnova, D. A.; Shadrivov, I. V.; Miroshnichenko, A. E.; Smirnov, A. I.; Kivshar, Y. S. Second-Harmonic Generation by a Graphene Nanoparticle. *Phys. Rev. B* **2014,** *90*, 035412.

53. Roke, S.; Gonella, G. Nonlinear Light Scattering and Spectroscopy of Particles and Droplets in Liquids. *Annu. Rev. Phys. Chem.* **2012,** *63*, 353-378.

54. Yan, E. C. Y.; Liu, Y.; Eisenthal, K. B. New Method for Determination of Surface Potential of Microscopic Particles by Second Harmonic Generation. *J. Phys. Chem. B* **1998,** *102*, 6331-6336.

55. Darlington, A. M.; Gibbs-Davis, J. M. Bimodal or Trimodal? The Influence of Starting pH on Site Identity and Distribution at the Low Salt Aqueous/Silica Interface. *J. Phys. Chem. C* **2015,** *119*, 16560-16567.

56. Campen, R. K.; Pymer, A. K.; Nihonyanagi, S.; Borguet, E., Linking Surface Potential and Deprotonation in Nanoporous Silica: Second Harmonic Generation and Acid/Base Titration. *J. Phys. Chem. C* **2010,** *114*, 18465-18473.

57. Schneider, L.; Peukert, W., Second Harmonic Generation Spectroscopy as a Method for in Situ and Online Characterization of Particle Surface Properties. *Part. Part. Syst. Charact.* **2006,** *23*, 351-359.

58. Walter, S. R.; Geiger, F. M., DNA on Stage: Showcasing Oligonucleotides at Surfaces and Interfaces with Second Harmonic and Vibrational Sum Frequency Generation. *J. Phys. Chem. Lett.* **2009,** *1*, 9-15.

59. Li, H.; Xia, H.; Wang, D.; Tao, X. Simple Synthesis of Monodisperse, Quasi-Spherical, Citrate-Stabilized Silver Nanocrystals in Water. *Langmuir* **2013,** *29*, 5074-5079.

60. Pereira, M.; Lai, E. P. Capillary Electrophoresis for the Characterization of Quantum Dots After Non-Selective or Selective Bioconjugation With Antibodies for Immunoassay. *J. Nanobiotechnology* **2008,** *6*, 10.

61. Evans, D. F.; Wennerström, H. *The Colloidal Domain: Where Physics, Chemistry, Biology, and Technology Meet*. WILEY-VCH: New York, 1999.

62. Doughty, B.; Kazer, S. W.; Eisenthal, K. B., Binding and Cleavage of DNA With the Restriction Enzyme EcoR1 Using Time-Resolved Second Harmonic Generation. *Proc. Natl. Acad. Sci.* **2011,** *108*, 19979-19984.

63. Karam, T. E.; Khoury, R. A.; Haber, L. H. Excited-State Dynamics of Size-Dependent Colloidal TiO2-Au Nanocomposites. *J. Chem. Phys* **2016,** *144*, 124704.

CHAPTER 5

NEAR INFRARED PHOTOTHERMAL RELEASE OF MICRORNA FROM THE SURFACE OF COLLOIDAL GOLD-SILVER-GOLD CORE-SHELL-SHELL NANOPARTICLES STUDIED WITH SECOND HARMONIC GENERATION

5.1 Introduction

Plasmonic nanoparticles composed of gold and silver have been widely studied due to their potential applications in nanomedicine, catalysis, photovoltaics, and optoelectronics.[1-10] These nanoparticles have unique properties including localized surface plasmon resonances, large surface area to volume ratios, low toxicities, excellent biocompatibilities, and control over surface functionalities.[11-15] Localized surface plasmon resonances are coherent oscillations of free electrons excited by electromagnetic radiation that can vary under changing the size, shape, composition, and surrounding medium of nanoparticles.[8, 16-18] Additionally, the surface chemistry and synthesis methods of gold and silver nanoparticles are advantageous for producing hybrid and bimetallic core-shell nanoparticles. Bimetallic core-shell nanoparticles have drawn special interest in the scientific community due to their altered optical and electrical properties as compared to the corresponding monometallic nanoparticles. Depending on the size and the ratio of the core and shell dimensions, the properties of the core-shell nanoparticles can therefore be tuned for desired plasmonic applications.[19-20]

In our previous work, we investigated photocleaving kinetics of miRNA from the surface of gold and silver nanoparticles using second harmonic generation (SHG) spectroscopy.[21-22] A nitobenzyl photocleavable linker was used to release the oligonucleotides from the surface of nanoparticle under ultraviolet (UV) irradiation. Plasmon enhanced photocleaving was observed in silver and gold nanoparticles with corresponding rate constants that were approximately six times and two times higher than in the non-plasmonic polystyrene sulfate nanoparticles, respectively. In

order to extend photoactivated drug delivery to near-infrared (NIR) wavelengths that are better suited for the optical window of biological samples, novel gold-silver-gold core-shell-shell (CSS) nanoparticles are used in this current study. The plasmon peak of these core-shell-shell nanoparticle is in the NIR region and the plasmon peak can be controlled by changing the core and shell sizes.[23] MiRNA is attached to the surface of CSS nanoparticle using a photothermal-cleavable linker made through the Diels-Alder reaction of furfuryl mercaptan with 6-maleimidohexanoic acid. Upon photothermal excitation in the NIR, miRNA is released through a retro Diels-Alder reaction above a local temperature of approximately 60 °C. The kinetics of the photothermal release in real time is monitored using second harmonic generation. The Scheme 1 shows the miRNA attached to a CSS nanoparticle using Diels-Alder chemistry. The fluorophore Alexa350 is attached at the end of the miRNA for quantification measurements.

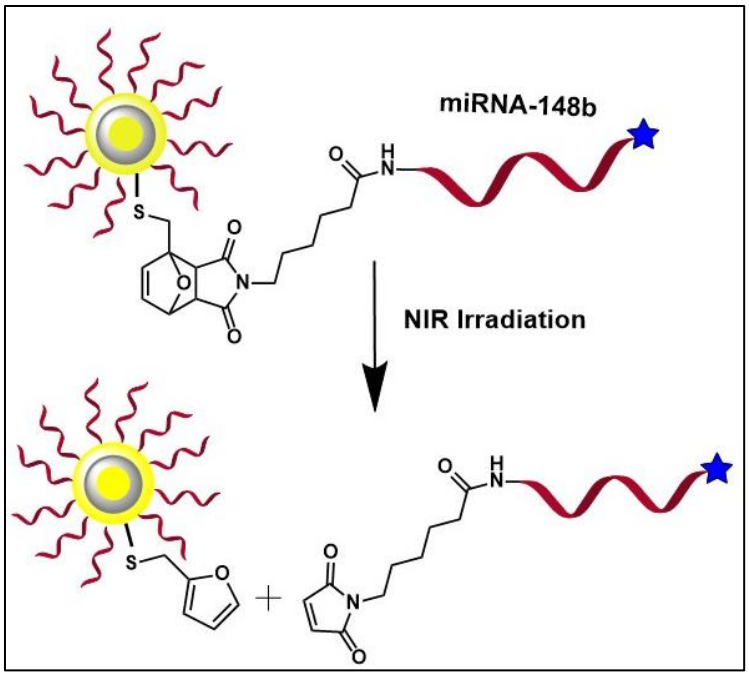

Scheme 5.1. MicroRNA is attached to the surface of gold-silver-gold core-shell-shell nanoparticles using Diels-Alder chemistry.

Second harmonic generation is a powerful, noninvasive, surface sensitive technique that is useful for the investigation of colloidal nanoparticles.[24-31] In SHG spectroscopy, two incident photons of frequency ω add coherently to generate a photon of frequency 2ω. This nonlinear optical process is dipole forbidden in bulk media with inversion symmetry, but SHG can be generated from the surface of nanoparticles where the inversion symmetry is broken. The second harmonic field (E_{SHG}) is proportional to the square root of the SHG intensity,

$$\sqrt{I_{SHG}} = E_{SHG} = \chi^{(2)} E_\omega E_\omega + \chi^{(3)} E_\omega E_\omega \Phi(0) \quad (5.1)$$

where, $\chi^{(2)}$ and $\chi^{(3)}$ are second and third order non-linear susceptibilities, respectively, E_ω is the electric field of the incident laser having frequency ω, and Φ(0) is the electrostatic surface potential.

5.2 Synthesis and Characterization

Gold-silver-gold core-shell-shell nanoparticles are prepared using a procedure which has been described previously.[23, 32] In the first step, gold nanoparticle seeds are synthesized by adding 900 μL of 34 mM sodium citrate to 30 mL of 290 μM gold chloride in ultrapure water under boiling conditions and vigorous stirring. The solution changes color to a bright red after 10 min and the reaction is cooled the room temperature. For the growth of the silver shell, 200 μl of the gold nanoparticle seeds is added to 10 mL ultrapure water followed by the addition of 60 μL of 100 mM ascorbic acid, 15 μL of 100 mM silver nitrate, and 75 μL of 100 mM sodium hydroxide. The obtained gold-silver core-shell nanoparticle is then centrifuged and resuspended in 10 mL ultrapure water. The outer gold shell is grown by the addition of 100 μL of 29 mM chloroauric acid, 100 μL of 0.03 M hydroquinone and 25 μL of 34 mM sodium citrate in 10 mL of gold-silver core-shell. The solution is allowed to stir at room temperature for another 1 hr. The obtained CSS nanoparticles are centrifuged and resuspended in 10 mL ultrapure water.

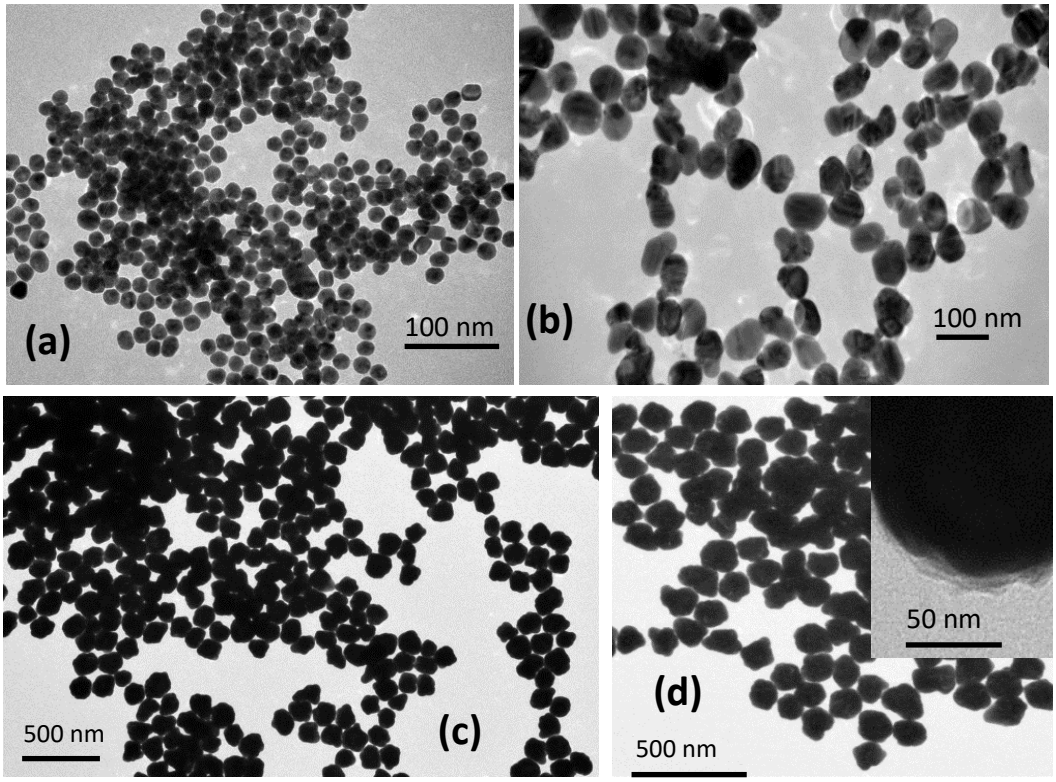

Figure 5.1. Representative TEM images of (a) gold nanoparticle seeds, (b) gold-silver core-shell nanoparticles, (c) gold-silver-gold core-shell-shell nanoparticles and (d) miRNA-functionalized gold-silver-gold core-shell-shell nanoparticles. Inset in Figure (d) shows the miRNA at the surface of nanoparticle.

The gold-silver-gold core-shell-shell nanoparticles are characterized using extinction spectroscopy and transmission electron microscopy (TEM). Figures 5.1 (a), (b), and (c) show representative TEM images of gold nanoparticle seeds (18 ± 1 nm), gold-silver core-shell (60 ± 7 nm), and gold-silver-gold core-shell-shell (120 ± 15 nm) nanoparticles, respectively. Figure 5.1 (d) shows the TEM images of CSS nanoparticle functionalized with miRNA. The inset of Figure 5.1 (d) shows a higher magnification for the CSS nanoparticle surface. Plasmon peaks of the nanoparticles are blue shifted upon the formation of the core-shell structure and are red shifted upon the formation of the core-shell-shell structure, as shown in Figure 5.2. The plasmon peak of the gold nanoparticle (GNP) seeds, the gold-silver core-shell (CS) nanoparticles, and the CSS are centered at 524 nm, 420 nm, and 745 nm, respectively.

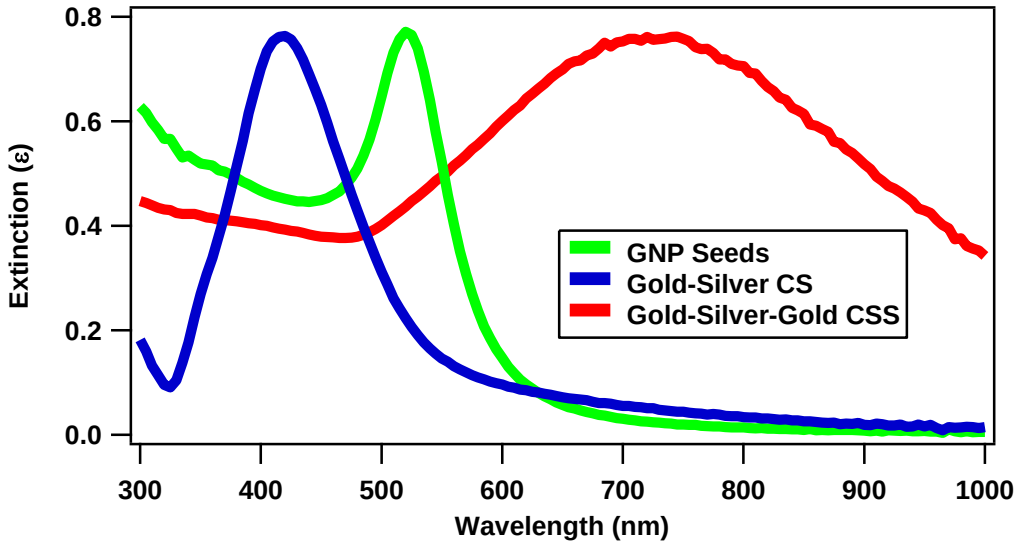

Figure 5.2. Extinction spectra of gold nanoparticle seeds (green line), gold-silver core-shell nanoparticles (blue line), and gold-silver-gold core-shell-shell nanoparticles (red line).

5.3 Experimental Setup

The experimental setup for monitoring the photothermal release of miRNA from the surface of colloidal CSS nanoparticles using SHG has been described previously.[21-22] A Ti:sapphire oscillator laser centered at 800 nm with a 70 fs pulse duration, 80 MHz repetition rate, and 2.6 W average output power is used. A portion of the oscillator laser beam passes through a beam splitter to seed the amplifier laser. The amplifier produces a laser beam centered at 800 nm with a 75 fs pulse duration, a 10 kHz repetition rate, and a 7 W average output power. The amplifier laser is used to irradiate the CSS nanoparticle sample to induce the photothermal cleaving of the miRNA while the remaining portion of the oscillator laser is used to monitor the photothermal cleaving kinetics in real time using SHG spectroscopy. A computer controlled beam block is used to block the amplifier irradiation beam while taking SHG signal with the oscillator laser. For the SHG measurements, the oscillator laser power is attenuated to a constant value of 300 mW in order to minimize photothermal release from the CSS surface while probing the kinetics. A quartz cuvette of 1 cm × 1 cm is used to contain 2 mL of the CSS sample. The amplifier laser power is

varied and the photothermal cleaving kinetics are monitored as a function irradiation time and power.

5.4 Result and Discussion

The photothermal release of miRNA from the surface of gold-silver-gold core-shell-shell nanoparticles is studied in real time using SHG spectroscopy. Representative SHG spectra of miRNA-functionalized CSS nanoparticles at different NIR irradiation times of 0 min, 1.5 min, and 5 min are shown in Figure 5.3. The SHG signal from the miRNA-functionalized CSS sample decreases with time under NIR irradiation due to photothermal release of miRNA from the nanoparticle surface. Oligonucleotides attached to the surface of the nanoparticles cause increased SHG signal due to their high surface charge density through the $\chi^{(3)}$ effect.[21-22] The SHG signal is centered at 400 nm with full width half maximum of 4.5 nm. The rise in SHG intensity at longer wavelength is attributed to two-photon fluorescence taking place in the nanoparticle.

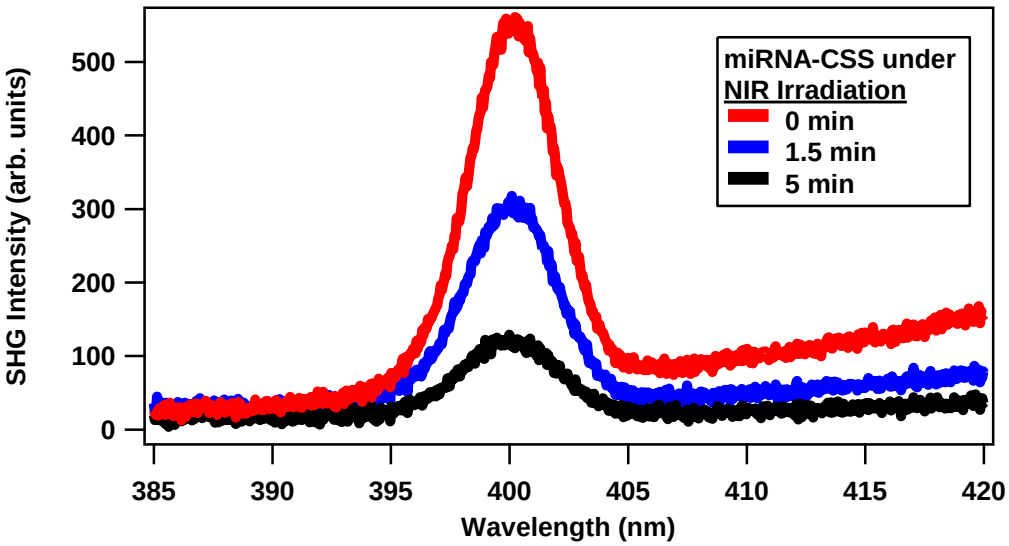

Figure 5.3. Representative SHG spectra of miRNA-functionalized CSS nanoparticles at different NIR irradiation times.

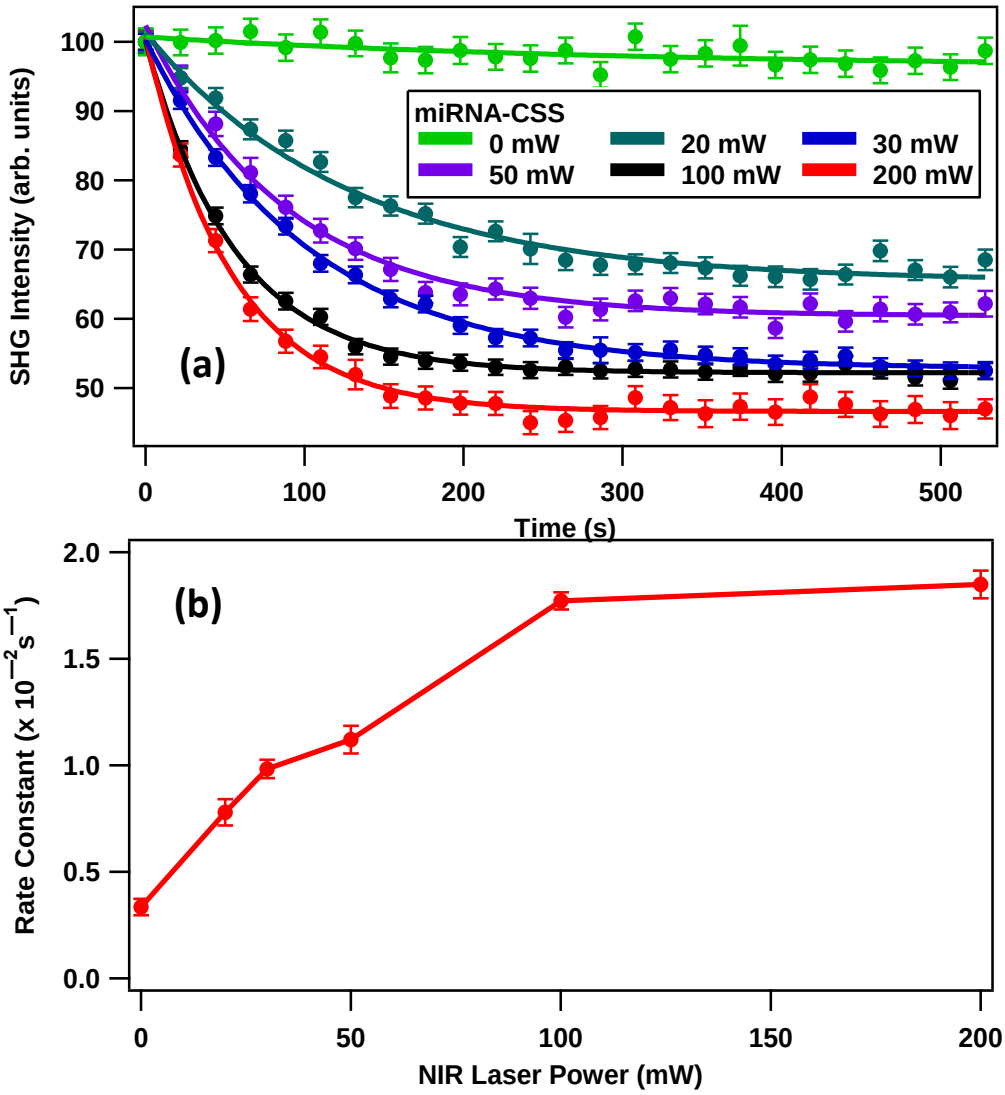

Figure 5.4. (a) SHG intensity of the miRNA-functionalized CSS nanoparticles as a function of time under varying NIR irradiation powers. (b) The obtained photothermal cleaving rate constants as a function of laser power.

Figure 5.4 (a) shows the power dependent analysis of the photothermal release of miRNA from the surface of CSS nanoparticle. The sample is irradiated with different laser powers of 0 mW, 12 mW, 30 mW, 50 mW, 100 mW, and 200 mW centered at 800 nm using the amplifier laser. The change in SHG intensity with time for miRNA-functionalized CSS nanoparticles is due to the photothermal release of miRNA from the interface. The time profile using no NIR irradiation from the amplifier laser (0 mW) shows only a slight decrease in SHG intensity of approximately

1% over time which is attributed to a small amount of photothermal cleaving by the oscillator probe laser. The kinetics of the photothermal release of miRNA under NIR irradiation is further analyzed by fitting the SHG time traces using a pseudo first-order exponential equation given by $E_{SHG} = A + B\, e^{-kt}$, where A and B are constants.[21-22] The obtained rate constants k are (0.48 ± 0.03) × 10^{-2} s^{-1}, (0.78 ± 0.06) × 10^{-2} s^{-1}, (1.08 ± 0.04) × 10^{-2} s^{-1}, (1.41 ± 0.10) × 10^{-2} s^{-1}, (1.99 ± 0.09) × 10^{-2} s^{-1} and (4.42 ± 0.21) × 10^{-2} s^{-1} for 12 mW, 30 mW, 50 mW, 100 mW, and 200 mW irradiation laser powers, respectively. The obtained rate constants are plotted as a function of laser power, as shown in Figure 5.4 (b).

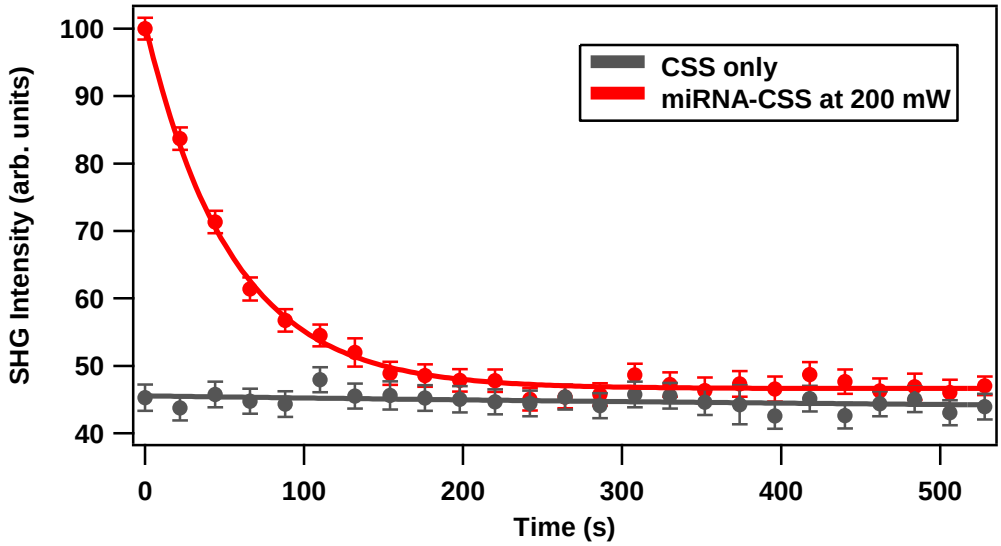

Figure 5.5. Control experiments showing the time-dependent SHG signal for CSS nanoparticlesusing 300 mW 800 nm probe laser only (gray data) and miRNA-functionalized CSS nanoparticles using both 300 mW 800 nm probe laser and 200 mW 800 pump laser (red data).

The thermal release of miRNA from the surface of colloidal CSS nanoparticles is also studied using SHG spectroscopy. The thermal treatment consists of placing 2 mL of the miRNA-functionalized CSS sample in a quartz cuvette wrapped by electrical heating tape. The sample is allowed to run for 8 min under slow stirring for each measurement using temperatures of 25 °C, 40 °C, 60 °C, and 80 °C while measuring the SHG signal as a function of time. Thermal release of

miRNA from the surface of CSS nanoparticle is shown in Figure 5.6. There is no thermal release of miRNA at 25 °C and 40 °C indicating that the oligonucleotides do not release at room temperature or normal body temperature. The rate of photothermal release is apparent at temperatures of 60 °C and 80 °C with faster thermal cleaving rates at the higher temperature of 80 °C.

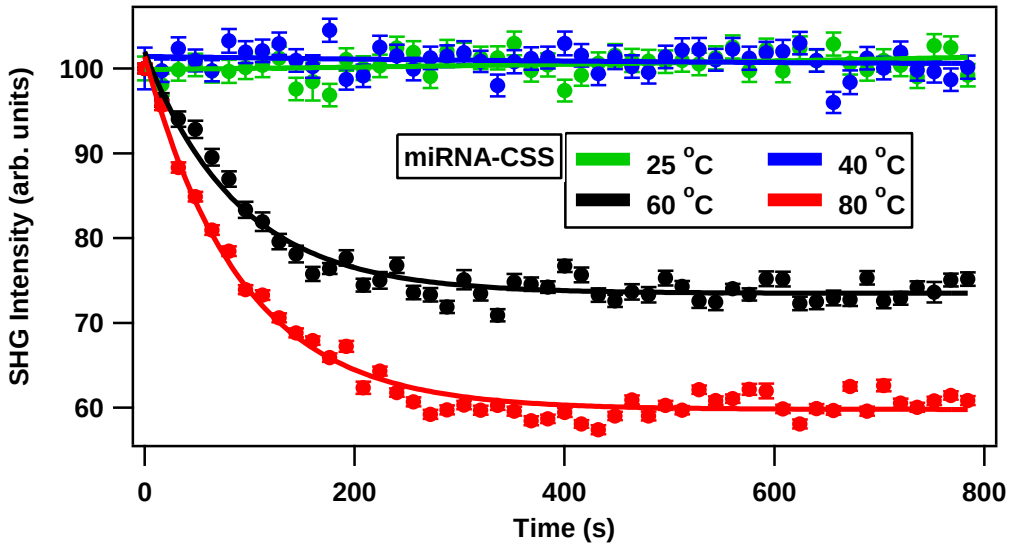

Figure 5.6. SHG intensity as a function of time from the miRNA-functionalized CSS nanoparticles showing the thermal release of miRNA from the nanoparticle surface under different temperatures.

The amount of miRNA released from the surface of CSS nanoparticle is quantified using fluorescence measurements with the results shown in Figure 5.7. The procedure for miRNA fluorescence quantification has been described previously.[21-22] The nanoparticle samples are centrifuged and the amount of remaining miRNA in the supernatant is quantified from a fluorescence calibration curve. The amount of miRNA released from the surface of CSS and GNPs are comparable when performing chemical reduction using dithiothreitol (DTT), which completely cleaves the miRNA from the nanoparticle surface. This indicates that both the CSS and GNP samples originally have comparable amounts of attached miRNA. However, the amount of miRNA released from the surface of miRNA-functionalized CSS nanoparticles is significantly

higher than the amount released from the GNPs under NIR irradiation. The CSS nanoparticles show complete cleaving using NIR irradiation powers of 12 mW, 30 mW, 50 mW, 100 mW, and 200 mW, respectively, to within experimental uncertainty for 8 min. Much lower miRNA release is observed for the GNP sample at these NIR powers, with increasing release concentrations under increasing NIR powers. These results further demonstrate the dramatically improved photothermal efficiencies and corresponding photothermal cleaving efficiencies of the miRNA-functionalized CSS nanoparticles compared to the miRNA-functionalized gold nanoparticles.

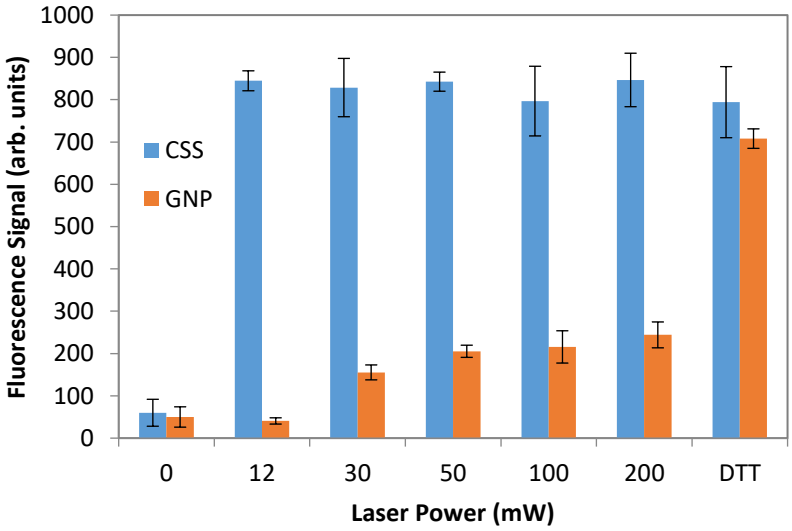

Figure 5.7. Fluorescence signals of miRNA-functionalized CSS (blue) and miRNA-functionalized GNP samples after DTT reduction and after NIR laser irradiations at various powers.

5.5 Conclusion

The NIR photothermal cleaving kinetics of miRNA functionalized to the surface of gold-silver-gold core-shell-shell nanoparticles are studied using time dependent second harmonic generation spectroscopy. The core and shell sizes are optimized for a maximum plasmonic peak in the NIR region, as verified by extinction spectroscopy and TEM measurements. The miRNA is attached to the CSS surface by a thermal-cleavable linker prepared by Diels Alder chemistry. The measured photothermal cleaving rate constants vary linearly with NIR irradiation power.

Additionally, fluorescence quantification of the amount of miRNA release shows that the photothermal cleaving efficiency is significantly higher for the CSS nanoparticles compared to gold nanoparticles prepared under similar conditions. These results demonstrate that gold-silver-gold core-shell-shell nanoparticles with photothermal cleaving linkers can be successfully utilized for targeted drug-delivery applications using near infrared irradiation in the optical window of biological tissue.

5.6 References

1. Austin, L. A.; Mackey, M. A.; Dreaden, E. C.; El-Sayed, M. A. The Optical, Photothermal, and Facile Surface Chemical Properties of Gold and Silver Nanoparticles in Biodiagnostics, Therapy, and Drug Delivery. *Arch. Toxicol.* **2014**, 1-27.

2. Ghosh, S. K.; Pal, T. Interparticle Coupling Effect on the Surface Plasmon Resonance of Gold Nanoparticles: from Theory to Applications. *Chem. Rev.* **2007,** *107*, 4797-4862.

3. Haes, A. J.; Hall, W. P.; Chang, L.; Klein, W. L.; Van Duyne, R. P. A Localized Surface Plasmon Resonance Biosensor: First Steps Toward an Assay for Alzheimer's Disease. *Nano Lett.* **2004,** *4*, 1029-1034.

4. Homola, J. Surface Plasmon Resonance Sensors for Detection of Chemical and Biological Species. *Chem. Rev.* **2008,** *108*, 462-493.

5. Homola, J.; Yee, S. S.; Gauglitz, G. Surface Plasmon Resonance Sensors: Review. *Sensors and Actuators B: Chemical* **1999,** *54*, 3-15.

6 Hou, W.; Cronin, S. B. A Review of Surface Plasmon Resonance-Enhanced Photocatalysis. *Adv. Funct. Mater.* **2013,** *23*, 1612-1619.

7. Hu, M.; Chen, J.; Li, Z.-Y.; Au, L.; Hartland, G. V.; Li, X.; Marquez, M.; Xia, Y. Gold Nanostructures: Engineering Their Plasmonic Properties for Biomedical Applications. *Chem. Soc. Rev.* **2006,** *35*, 1084-1094.

8. Hutter, E.; Fendler, J. H. Exploitation of Localized Surface Plasmon Resonance. *Adv. Mater.* **2004,** *16*, 1685-1706.

9. Jackson, J.; Halas, N. Silver Nanoshells: Variations in Morphologies and Optical Properties. *J. Phys. Chem. B* **2001,** *105*, 2743-2746.

10. Mody, V. V.; Siwale, R.; Singh, A.; Mody, H. R. Introduction to Metallic Nanoparticles. *J. Pharm. Bioall. Sci.* **2010,** *2*, 282-289.

11. Nikoobakht, B.; Wang, J.; El-Sayed, M. A. Surface-Enhanced Raman Scattering of Molecules Adsorbed on Gold Nanorods: Off-Surface Plasmon Resonance Condition. *Chem. Phys. Lett.* **2002,** *366*, 17-23.

12. Olson, J.; Dominguez-Medina, S.; Hoggard, A.; Wang, L.-Y.; Chang, W.-S.; Link, S. Optical Characterization of Single Plasmonic Nanoparticles. *Chem. Soc. Rev.* **2015,** *44*, 40-57.

13. Pattnaik, P. Surface Plasmon Resonance. *Biotechnol. Appl. Biochem.* **2005,** *126*, 79-92.

14. Willets, K. A.; Van Duyne, R. P. Localized Surface Plasmon Resonance Spectroscopy and Sensing. *Annu. Rev. Phys. Chem.* **2007,** *58*, 267-297.

15. Yeh, Y.-C.; Creran, B.; Rotello, V. M. Gold Nanoparticles: Preparation, Properties, and Applications in Bionanotechnology. *Nanoscale* **2012,** *4*, 1871-1880.

16. Halas, N. J.; Lal, S.; Chang, W.-S.; Link, S.; Nordlander, P. Plasmons in Strongly Coupled Metallic Nanostructures. *Chem. Rev.* **2011,** *111*, 3913-3961.

17. Klar, T.; Perner, M.; Grosse, S.; Von Plessen, G.; Spirkl, W.; Feldmann, J. Surface-Plasmon Resonances in Single Metallic Nanoparticles. *Phy. rev. lett.* **1998,** *80*, 4249-4252.

18. Lal, S.; Link, S.; Halas, N. J. Nano-Optics from Sensing to Waveguiding. *Nat. Photon.* **2007,** *1*, 641-648.

19. Ghosh Chaudhuri, R.; Paria, S. Core/Shell Nanoparticles: Classes, Properties, Synthesis Mechanisms, Characterization, and Applications. *Chem. Rev.* **2011,** *112*, 2373-2433.

20. Zhong, C.-J.; Maye, M. M. Core–Shell Assembled Nanoparticles as Catalysts. *Adv. Mater.* **2001,** *13*, 1507-1511.

21. Kumal, R. R.; Abu-Laban, M.; Landry, C. R.; Kruger, B.; Zhang, Z.; Hayes, D. J.; Haber, L. H. Plasmon-Enhanced Photocleaving Dynamics in Colloidal MicroRNA-Functionalized Silver Nanoparticles Monitored with Second Harmonic Generation. *Langmuir* **2016,** *32*, 10394-10401.

22. Kumal, R. R.; Landry, C. R.; Abu-Laban, M.; Hayes, D. J.; Haber, L. H. Monitoring the Photocleaving Dynamics of Colloidal MicroRNA-Functionalized Gold Nanoparticles Using Second Harmonic Generation. *Langmuir* **2015,** *31*, 9983-9990.

23. Karam, T. E.; Smith, H. T.; Haber, L. H. Enhanced Photothermal Effects and Excited-State Dynamics of Plasmonic Size-Controlled Gold–Silver–Gold Core–Shell–Shell Nanoparticles. *J. Phys. Chem. C* **2015,** *119*, 18573-18580.

24. Eisenthal, K. B. Second Harmonic Spectroscopy of Aqueous Nano-and Microparticle Interfaces. *Chem. Rev.* **2006,** *106*, 1462-1477.

25. Yan, E. C. Y.; Liu, Y.; Eisenthal, K. B. New Method for Determination of Surface Potential of Microscopic Particles by Second Harmonic Generation. *J. Phys. Chem. B* **1998,** *102*, 6331-6336.

26. Hayes, P. L.; Malin, J. N.; Jordan, D. S.; Geiger, F. M. Get Charged up: Nonlinear Optical Voltammetry for Quantifying the Thermodynamics and Electrostatics of Metal Cations at Aqueous/Oxide Interfaces. *Chem. Phys. Lett.* **2010,** *499*, 183-192.

27. Boman, F. C.; Gibbs-Davis, J. M.; Heckman, L. M.; Stepp, B. R.; Nguyen, S. T.; Geiger, F. M. DNA at Aqueous/Solid Interfaces: Chirality-Based Detection via Second Harmonic Generation Activity. *J. Am. Chem. Soc.* **2008,** *131*, 844-848.

28. Malin, J. N.; Hayes, P. L.; Geiger, F. M. Interactions of Ca, Zn, and Cd Ions at Buried Solid/Water Interfaces Studied by Second Harmonic Generation. *J. Phys. Chem. C* **2009,** *113*, 2041-2052.

29. Malin, J. N.; Holland, J. G.; Saslow, S. A.; Geiger, F. M. U(VI) Adsorption and Speciation at the Acidic Silica/Water Interface Studied by Resonant and Nonresonant Second Harmonic Generation. *J. Phys. Chem. C* **2011,** *115*, 13353-13360.

30. Gonella, G.; Dai, H.-L. Determination of adsorption geometry on spherical particles from nonlinear Mie theory analysis of surface second harmonic generation. *Phys. Rev. B: Condens. Matter Mater. Phys.* **2011,** *84* (12), 121402/1-121402/5.

31. Gonella, G.; Dai, H.-L. Second Harmonic Light Scattering from the Surface of Colloidal Objects: Theory and Applications. *Langmuir* **2013,** *30*, 2588-2599.

32. Kumal, R. R.; Karam, T. E.; Haber, L. H. Determination of the Surface Charge Density of Colloidal Gold Nanoparticles Using Second Harmonic Generation. *J. Phys. Chem. C* **2015,** *119*, 16200-16207.

CHAPTER 6

IMPACTS OF SALT, BUFFER, AND LIPID NATURE ON MOLECULAR ADSORPTION AND TRANSPORT IN LIPID BILAYER AS OBSERVED BY SECOND HARMONIC GENERATION*

6.1 Introduction

Living cell activities depend critically on cell interactions with the surrounding environment through the transport of biomolecules and contents exchange between intracellular and extracellular fluids via the plasma membrane interface, which is composed of lipid bilayers and membrane proteins.[1-3] Active transport across the plasma membrane requires energy for moving molecules from low concentration regions to high concentration regions as a result of the aid provided by membrane proteins, while passive transport involves molecular flux arising mainly from concentration gradients.[4-9] In this regard, most drugs and chemotherapeutic agents enter cells by passive transport through the cellular membrane.[10-15] Thus, the translocation of such molecules in a contacting solution across the cellular membrane is characterized by events that include molecular adsorption, partitioning, and diffusion, wherein the partition coefficient is indicative of molecule solubility in the hydrophobic lipid bilayer region, and the diffusion coefficient is representative of the rate of molecular transfer in the membrane.[16-18] The rich variety of lipid species in the membrane undergo different chemical interactions with molecules and ions, which are ultimately attributed to processes such as protein organization,[19, 20] membrane fusion,[7] and cellular signal communication.[19] Liposomes—small spherical vesicles whose bilayers are composed of phospholipids—can be considered as models of cell membranes that are useful for fundamental investigations of molecular interactions with lipid bilayers in aqueous millieu.[21]

*"Reprinted with permission from [Kumal, R. R.; Nguyenhuu, H.; Winter, J.; McCarley, R.; Haber, L. H. J. Phys. Chem. C **2017**, 121, 15851-15860]. Copyright [2017] American Chemical Society."

Additionally, liposomes are widely utilized for drug delivery applications.[17, 21] Therefore, obtaining information regarding time-resolved molecular transport kinetics of small molecules in liposomal models, as a function of lipid nature (composition) and environment (electrolyte nature and concentration) is important to establish a basic understanding of factors influencing drug uptake and intrinsic molecular interactions involved at cell membrane interfaces.

Second harmonic generation (SHG) is a versatile surface-sensitive technique for probing various interfacial phenomena, such as molecular transport in living cells,[22-24] molecular adsorption,[25-29] surface charge densities,[30-32] and interfacial dynamics of micrometer- to nanometer-sized colloidal particles.[33-39] SHG is a two-photon process wherein two photons of frequency ω are added coherently in phase to generate a third photon of frequency 2ω. While SHG is a dipole and symmetry forbidden process in isotropic media, such as randomly-oriented molecules in solution, it can be generated from the surface of nanoparticles and liposomes where the symmetry is broken. This makes SHG a non-invasive, highly surface-sensitive spectroscopic technique that is well suited for investigating molecular adsorption and real-time molecular transport kinetics in liposome samples in solution.[32-33, 38-39]

The second harmonic response from an interface is induced by the second-order polarization under an applied optical electric field E_ω characterized by the second-order and third-order nonlinear susceptibilities, $\chi^{(2)}$ and $\chi^{(3)}$, respectively. The total second harmonic electric field E_{SHG} is a coherent process given by the equation,[38, 40-46]

$$E_{SHG} = \sqrt{I_{SHG}} = \chi^{(2)} E_\omega E_\omega + \chi^{(3)} E_\omega E_\omega \phi_0 \qquad (6.1)$$

where I_{SHG} is the SHG intensity and ϕ_0 is the interfacial electrostatic potential arising from a static electric field. The $\chi^{(2)}$ susceptibility tensor comes about from the second-order

hyperpolarizability of the colloidal nanoparticle and each molecule at the nanoparticle interface in the presence of the optical electric field E_ω, including both electric dipole and quadruple terms.[44, 47] The genesis of the $\chi^{(3)}$ susceptibility tensor is the third-order hyperpolarizability of water molecules that are partially aligned by the static electric field at the nanoparticle surface. SHG from spherical, centrosymmetric colloidal nanoparticles can be observed even for sizes much smaller than the wavelength of light due to the phase shift of the SHG fields on opposite sides of the nanoparticle.[38, 44, 47-48] The SHG signal from a colloidal sample is then an incoherent sum of second harmonic contributions from each colloidal nanoparticle.[49-51] For membrane systems, such as liposomes having a bilayer thickness of about 5 nm, dye molecules adsorbed at the outer membrane/water interface and the inner membrane/water interface generate approximately equal and opposite second order polarizations.[52] The SHG electric field signals from the two populations of dye molecules across the membrane are therefore out of phase, and the measured net SHG signal is approximately proportional to the difference in the inner and outer populations of the adsorbed dye molecules.[53-56]

Here, we demonstrate the use of time-resolved SHG to study molecular adsorption and transport of cationic dyes in phospholipid bilayers of liposomes prepared in aqueous media. The adsorption and transport of dye molecules are monitored in real time for dioleoylphosphatidyl-glycerol (DOPG), dioleoylphosphoserine (DOPS), tri-methyl quinone dioleoylphospho-ethanolamine (QPADOPE), and dioleoylphosphocholine (DOPC) liposomes under various buffer and salt conditions. Key insight toward understanding basic ion-transport phenomena in liposome-based, drug-delivery processes is provided by investigations of the interactions and transport of cationic, drug-like molecules, such as malachite green (MG) and methyl green (MetG) that possess aromatic and ammonium functionalities, using charged and neutral lipid bilayers. Use of these

small-molecule organic dyes offers enhanced SHG signals because they absorb near 400 nm, which is on resonance with the SHG frequency, and have large $\chi^{(2)}$ susceptibilities when adsorbed to a colloidal surface.[25] By carefully monitoring the time-dependent SHG signal in different liposome samples after the addition of these molecular dyes under varying concentrations and solution conditions, the quantitative properties of adsorption and transport are determined to better understand fundamental molecular and ionic interactions at the liposome interface for advancing potential drug-delivery applications.

6.2 Synthesis and Characterization

The liposome samples are prepared by an extrusion method, as described previously.[57-58] Approximately 3–5 mg of dry lipid is dissolved in dichloromethane in a glass ground joint test tube. The solvent is removed via rotary evaporation so as to produce a lipid film on the interior of the test tube, which is then placed overnight under high vacuum. The dried thin film of lipid is hydrated by addition of 1 mL of the desired buffer. After 2 hours, the vessel is agitated by six freeze-thaw cycles. An Avanti mini-extruder (Avanti Polar Lipids) equipped with a 200-nm pore track-etched polycarbonate membrane is used to control the size distribution of the vesicles. The quinone phospholipid (QPADOPE) is synthesized by coupling the *N*-hydroxysuccinimide ester of the quinone acid with the amine group of DOPE.[57] The molecular structures of DOPG, DOPS, MG and MetG are shown in Figure 6.1, and those of QPADOPE and DOPC are provided in the Appendix 3. The lipid concentration is determined using a Bartlett assay, as described in the Appendix 3.

Liposome nanoparticles are characterized using dynamic light scattering (DLS) and zeta potential measurements. The average hydrodynamic diameter of the liposomes is measured to be 154 ± 35 nm with a polydispersity index of ≤ 0.07 for all samples. Representative DLS size

distributions are shown in Figure A3.2. The zeta potentials of different liposomes at different buffer compositions are summarized in Table 6.1. Citrate buffers of four different compositions at pH 4.0 are used corresponding to (A) 5 mM citrate with 0 mM KCl, (B) 50 mM citrate with 0 mM KCl, (C) 5 mM citrate with 100 mM KCl, and (D) 50 mM citrate with 100 mM KCl. The zeta potentials of liposomes in the absence of KCl are more negative than the corresponding zeta potentials in the presence of KCl due to ionic screening. The zeta potential of DOPG and DOPS in the absence of KCl (Buffer A and B) is nearly the same whereas, in presence of KCl, the zeta potential of DOPG is slightly more negative than that of DOPS, indicating that there are different amounts of potassium cation and chloride anion adsorption at the surfaces of these liposomes. Similarly, the zeta potential of QPADOPE liposomes is comparable to that of DOPG and DOPS,

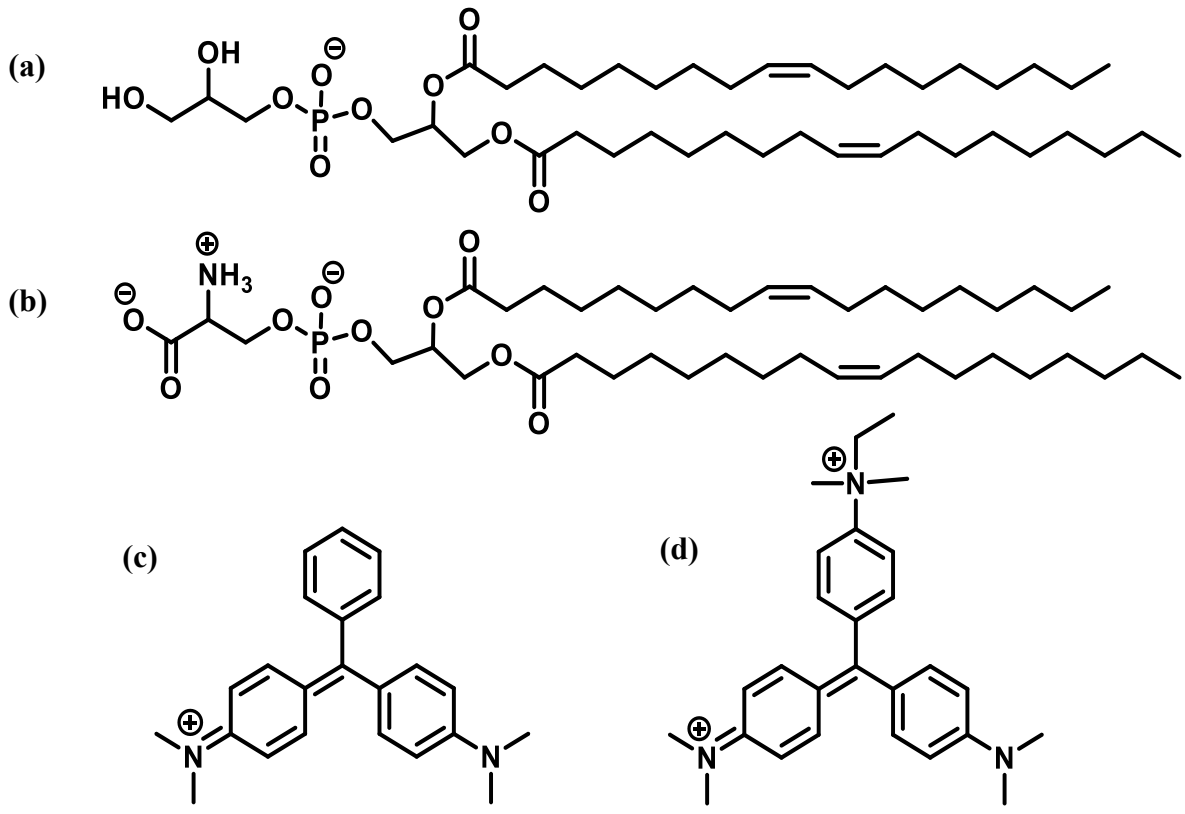

Figure 6.1. Molecular structures of (a) DOPG, (b) DOPS, (c) malachite green (MG), and (d) methyl green (MetG).

but DOPC is found to have a significantly lower zeta potential due to its neutral zwitterionic structure. The measured osmotic pressure and conductivity of the buffer solutions are also shown in Table 6.1.

Table 6.1. Conductivities and osmotic pressures of buffer solutions and the corresponding zeta potentials of different liposome samples.

Buffer	Conductivity (mS/cm)	Osmotic pressure (mmol/kg)	Zeta potential (mV)			
			DOPG	DOPS	QPADOPE	DOPC
A	0.66 ± 0.01	35 ± 2	-73.2 ± 1.1	-74.8 ± 1.7	-67.3 ± 1.5	-21.7± 2.3
B	5.57 ± 0.76	93 ± 3	-75.9 ± 2.6	-73.3 ± 3.5	-59.0 ± 2.3	-7.6 ± 1.1
C	13.4 ± 0.38	168 ± 3	-57.6 ± 2.9	-49.6 ± 2.9	-51.4 ± 3.8	-5.61 ± 0.2
D	17.5 ± 0.67	250 ± 4	-50.4 ± 3.0	-43.7 ± 1.1	-52.0 ± 1.9	-5.8 ± 0.2

Buffer A is 5 mM citrate and 0 mM KCl; B is 50 mM citrate and 0 mM KCl; C is 5 mM citrate and 100 mM KCl; and D is 50 mM citrate and 100 mM KCl. pH is 4.0 for all buffers.

6.3 Second Harmonic Generation Setup

The experimental setup for the second harmonic generation experiment has been reported previously.[30] Briefly, the setup consists of an ultrafast laser system, an optical setup, and a high sensitivity spectroscopy charge-coupled device (CCD) detector connected to a monochromator. A Ti:sapphire oscillator laser is used and has its output centered at 800 nm with 75 fs pulses at a repetition rate of 80 MHz and an average power of 2.6 W. The laser beam is attenuated to an average power of 1.0 W and is focused onto the sample in a 1-cm quartz cuvette. A bandpass filter is used after the sample to remove the fundamental wavelength, and the SHG signal is acquired in the forward direction. Multiple background-subtracted SHG spectra using 1 s acquisition times are collected as a function of time. A computer-controlled beam block is used to interrupt the beam to obtain background spectra and unblock the beam for the SHG spectra, with data collected using an automated file saving program. For each run, 10 SHG spectra and 5 background spectra are

acquired, and the average background spectrum is subtracted from the average SHG spectrum to get the background-subtracted spectrum as a function of time.

6.4 Results and Discussion

Background-subtracted SHG spectra of 50 μM DOPG liposomes in 5 mM citrate buffer before and after the addition of 15 μM MG are shown in Figure 6.2 (a). The SHG spectrum of these liposomes alone in 5 mM citrate buffer is shown to have a very small intensity at 400 nm, which is comparable to the corresponding signal from water or buffer, alone. Addition of MG increases the SHG signal significantly due to MG adsorption to the liposome surface, with a corresponding increase in the $\chi^{(2)}$ term. The SHG signal is enhanced by approximately 2.5 times compared to the signal from the MG alone under these conditions. For all cases, the SHG spectra are centered at 400 nm and have a full-width-at-half-maximum of 4.5 nm, when the incident energy of the laser is kept constant, centered at 800 nm. The SHG signal from free MG alone in buffer is due to hyper-Rayleigh scattering.[44, 59] The SHG spectra showing the change in SHG intensity as a function of time from 15 μM MG in 50 μM DOPG liposomes in 5 mM citrate buffer at 0 s, 20 s, 40 s, 140 s, and 200 s after MG addition are displayed in Figure 6.2 (b). The decrease in SHG signal as a function of time is caused by the transport of dye molecules through the liposome bilayer, which results in a scenario wherein the SHG fields of the oppositely oriented dye molecules on the inside and outside of the liposome increasingly cancel out each other.[23, 53, 56]

The transport kinetics of MG for DOPG and DOPS liposomes in citrate buffer at pH 4.0 are studied under various buffer conditions using SHG measurements. Citrate buffers A–D of the four different compositions described in Table 1 are used. The SHG time profiles of MG in DOPG and DOPS liposomes in the corresponding buffers are shown in Figures 6.3 and 6.4, respectively. The SHG intensities are all normalized with respect to DOPG liposomes upon addition of 15 μM

MG in buffer A for direct comparison. Interestingly, upon addition of MG to the liposome samples, the SHG signal is larger under lower concentrations of citrate and KCl in the buffer. This may be

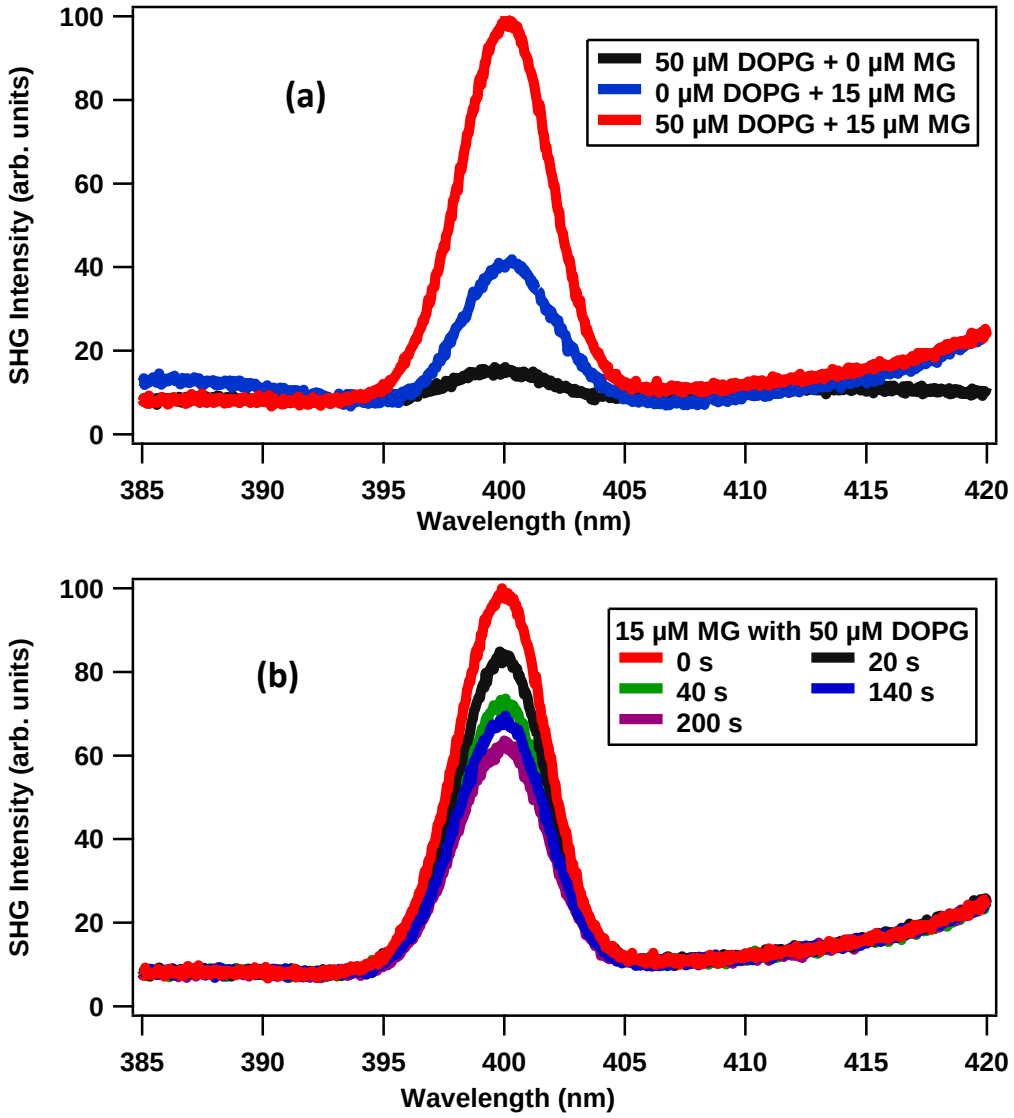

Figure 6.2. (a) SHG spectra of 150-nm diameter DOPG liposomes (50 μM lipid) in the presence of 0 μM and 15 μM malachite green (MG) compared to the SHG spectrum for 15 μM MG alone. (b) SHG spectra of 150-nm diameter DOPG (50 μM lipid) in 5 mM (pH 4.0) citrate buffer (no KCl) after the addition of 15 μM MG at various times.

caused by the formation of ion-pair complexes of anions in the buffer with the MG cation and subsequent changes in the distribution of MG orientation at the liposome surface.[55] Additionally, the added citrate and KCl may reduce the SHG intensity by lowering the $\chi^{(3)}$ term, due to ion screening of the

electrostatic surface potential.[41, 60] For both DOPG and DOPS liposomes, the SHG signals upon addition of MG are largest in buffer A and lowest in buffer D, consistent with the general trend that larger citrate and KCl concentrations decrease the SHG signal from the liposome surface with adsorbed MG. Furthermore, the SHG intensities of DOPS liposomes with added MG concentrations in buffer A are significantly larger than the DOPG liposomes under the same MG and buffer conditions. On the other hand, the SHG signals from DOPG and DOPS under corresponding MG concentrations are of comparable intensities in buffers B, C, and D. This suggests that MG interactions with liposome surfaces are significantly different in DOPG compared to DOPS, especially under low electrolyte and buffer concentrations. The SHG results are analyzed in more detail by comparing the time-dependent SHG signals of the different liposome samples in the varying buffer conditions to better understand the molecular interactions with the liposome surface, the transport of the molecular dye through the liposome bilayer, and the more complicated nature of the electrostatic ion-ion interactions at the liposome surface in aqueous colloidal suspension.

To study the molecular transport of MG through the liposome bilayer membranes under the different buffer conditions, the experimentally obtained SHG electric fields are fit to single exponential functions given by

$$E_{SHG}(t) = a_0 + a_1 e^{-t/\tau} \tag{6.2}$$

where, a_0 and a_1 are proportionality constants, t is the experimental time after MG addition, and τ is the measured transport time. The best fits are squared and plotted as SHG intensity in Figures 6.3 and 6.4 as solid lines for each corresponding MG concentration. The R^2-values for these fits are shown in Table A3.2. The obtained MG transport times for DOPG liposomes in different buffer solutions are plotted as a function of MG concentration in Figure 6.5 (a), where the transport time

is observed to gradually decrease with increasing dye concentration under all buffer conditions. All error bars from fits correspond to standard deviations. The transport rate, $1/\tau$, shows a general linear dependence on MG concentration in DOPG, as shown in Figure A3.3 (a), in agreement with previous studies.[52, 55] The rate of transport of MG through the lipid bilayer is highest in buffer A, lower in buffers B and C, and lowest in buffer D. This trend can be explained by the formation of ion pairs between MG and either chloride or the citrate, as shown previously.[55] The MG transport times for DOPS liposomes as a function of MG concentration in various buffers are shown in Figure 6.5 (b). The transport times for DOPS are significantly different than those of DOPG, with much less overall variation and no clear linear trend as a function of MG concentration, the latter possibly indicating different molecular and ion interactions at the DOPS liposome surface. In DOPS, the transport times are generally faster in 50 mM citrate than in 5 mM citrate, which is

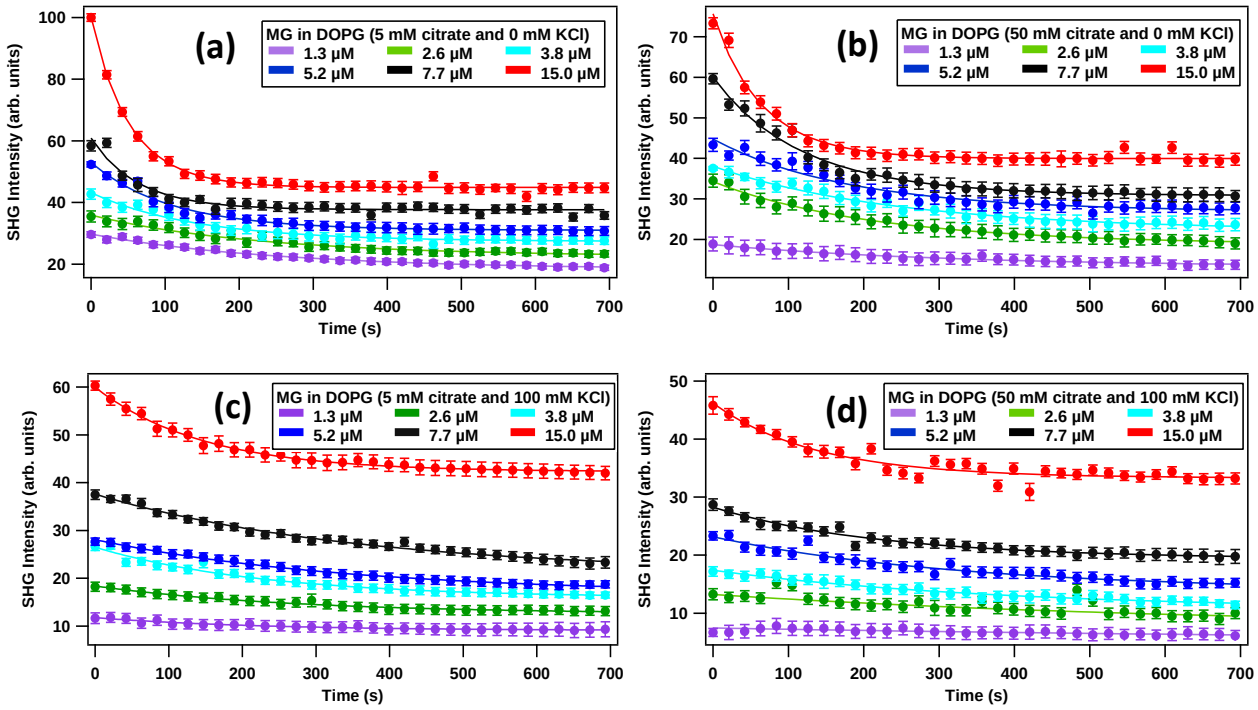

Figure 6.3. SHG time profiles of DOPG liposomes (50 μM lipid) with various MG concentrations in aqueous (pH 4.0) buffer solutions composed of (a) 5 mM citrate and 0 mM KCl, (b) 50 mM citrate and 0 KCl, (c) 5 mM citrate and 100 mM KCl, and (d) 50 mM citrate and 100 mM KCl.

opposite to the trend observed for DOPG. Additionally, the transport times are shorter with added KCl at low MG concentrations, but are longer with added KCl at high MG concentrations. The transport rate constant for DOPS liposomes as a function of MG concentration are shown in Figure A3.3 (b). In DOPS, where the transport rate constant is generally more constant as a function of MG concentration, the transport proceeds in accordance with Fick's law due to the concentration gradient across the membrane.[61] In DOPG, where the transport rate constant depends linearly with increased MG concentration, and faster transport occurs under lower ionic strength, MG transport is influenced more by ion-pair formation, in agreement with previous work;[52, 55] it may also be influenced more by electrodiffusion where the transport rate depends on the electrostatic potential across the membrane.[62] The transport times of various MG concentrations through DOPG and DOPS liposomes in different buffer solutions are also tabulated in Table A3.1 in the Appendix.

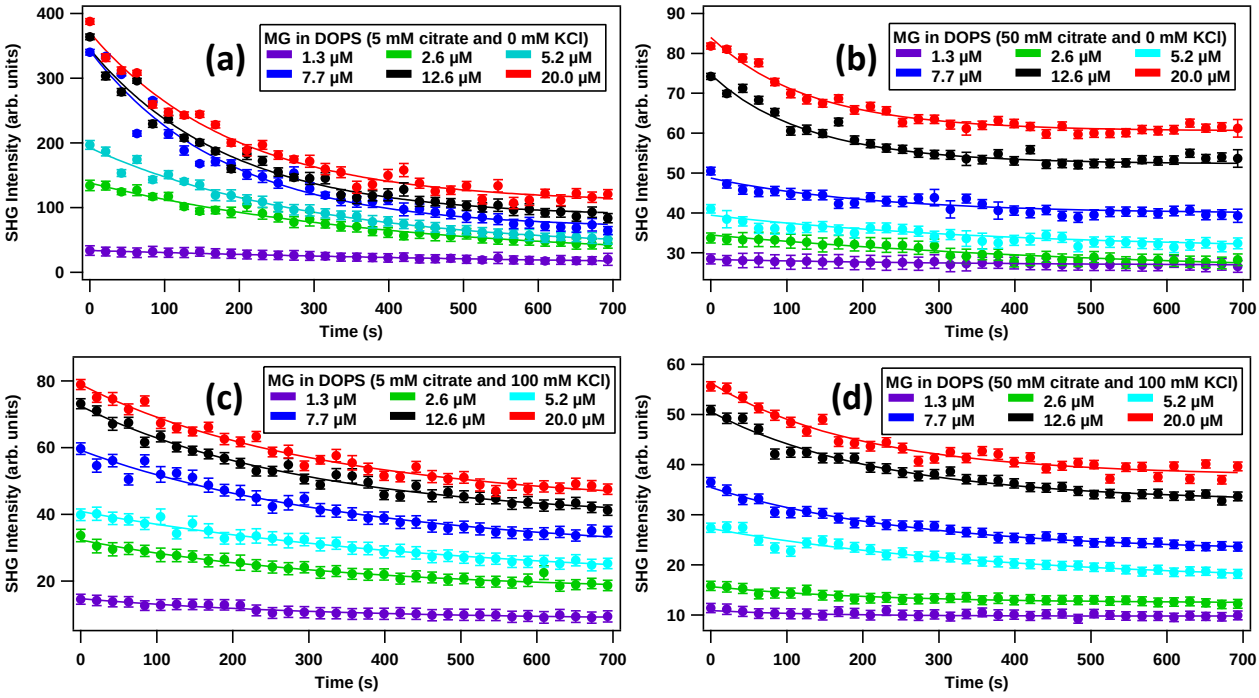

Figure 6.4. SHG time profiles of DOPS liposomes (50 μM lipid) with various MG concentrations in aqueous (pH 4.0) buffer solutions composed of (a) 5 mM citrate and 0 mM KCl, (b) 50 mM citrate and 0 KCl, (c) 5 mM citrate and 100 mM KCl, and (d) 50 mM citrate and 100 mM KCl.

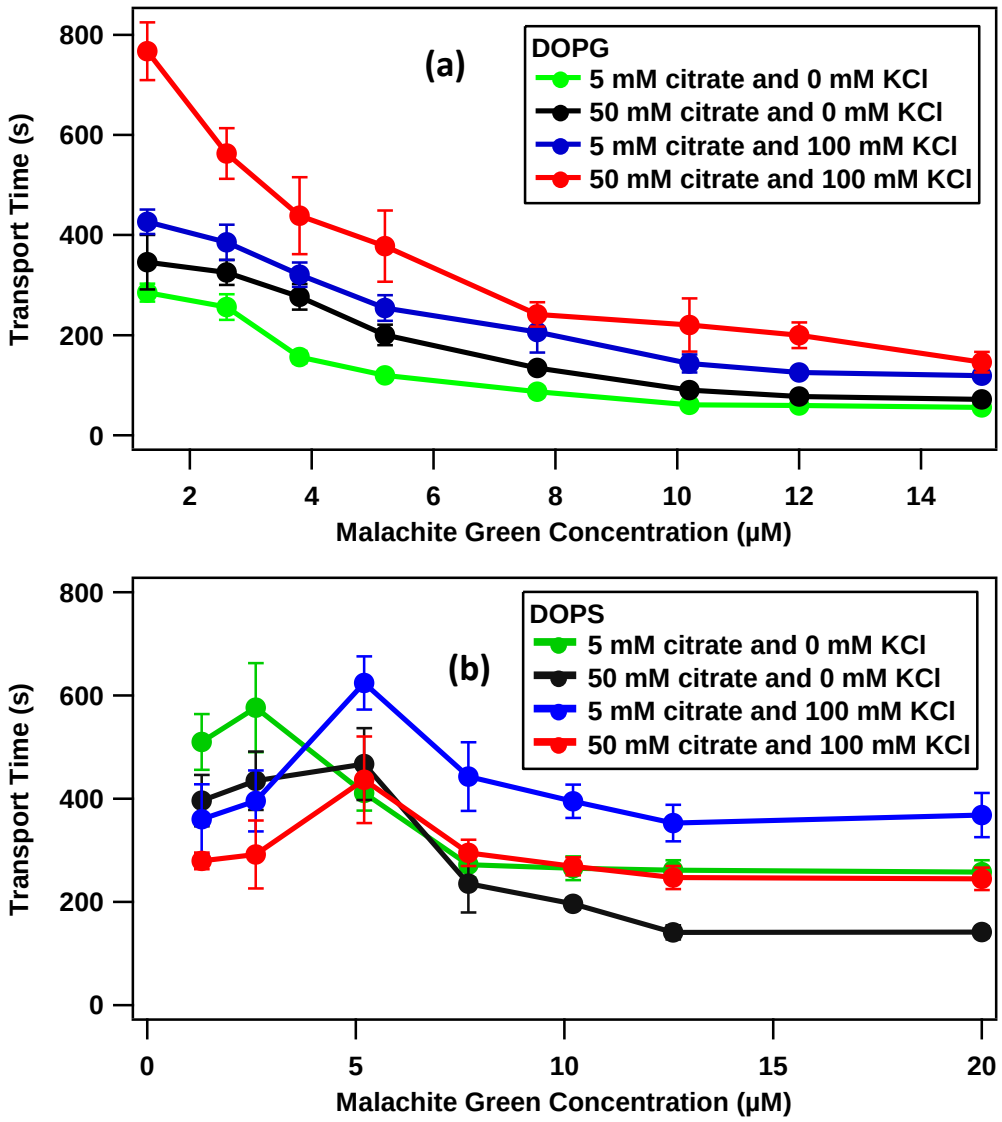

Figure 6.5. Transport times as a function of malachite green concentration at different citrate (pH 4.0) and KCl concentrations for (a) DOPG and (b) DOPS liposomes at lipid concentrations of 50 μM.

Adsorption isotherm measurements are performed in order to determine the adsorption site density and the free energy of adsorption of MG to the DOPG and DOPS liposome surfaces in citrate buffer. The SHG intensities for different MG concentrations are measured directly upon MG addition (at t = 0 s) using a fresh 50 μM liposome sample for each measurement. The SHG intensities at t = 0 s were fit using the modified Langmuir isotherm model that describes reversible adsorption to yield a monolayer, with [22, 25]

$$I_{SHG} = A\left(\frac{N}{N_{max}}\right)^2 + B + M\alpha \tag{6.3}$$

and

$$\frac{N}{N_{max}} = \frac{\left(\mathrm{C} + N_{max} + \frac{55.5}{k}\right) - \sqrt{\left(\mathrm{C} + N_{max} + \frac{55.5}{k}\right)^2 - 4CN_{max}}}{2\,N_{max}} \tag{6.4}$$

where, N is the concentration of dye molecules adsorbed, N_{max} is the maximum adsorption site concentration, A is the SHG intensity at saturation, B is the baseline offset, M is the concentration of free dye molecules in solution, α is the slope obtained from the plot of SHG intensity of dye alone as function of concentration *C*, 55.5 is the molar concentration of water, and k is the adsorption equilibrium constant. The free energy of adsorption is calculated using the equation $\Delta G = -RT\ ln\ k$. The number of lipid molecules per adsorption site of MG is obtained from the ratio of lipid concentration to the maximum adsorption site concentration.[52]

The adsorption isotherm is established by titrating a fixed concentration of lipids with an increasing concentration of MG until the SHG signal reaches a plateau at saturated adsorbate coverage. The SHG adsorption isotherms at four different buffer solutions as a function of MG concentration for DOPG and DOPS liposomes are shown in Figures 6.6 and 6.7, respectively. The corresponding variables and fitting parameters obtained are summarized in Table 2. For both DOPG and DOPS liposomes, the equilibrium constants and free energy of adsorption magnitudes are largest in buffer A having low citrate concentration and no added KCl, and are smallest in buffer D with a high citrate concentration and 100 mM KCl. The equilibrium constants for DOPG are (6.7 ± 0.4) × 10^7 in buffer A and (2.7 ± 0.3) × 10^7 in buffer D. Similarly, the equilibrium constants for DOPS are (4.7 ± 0.6) × 10^7 in buffer A and (2.2 ± 0.4) × 10^7 in buffer D. This follows the same trend as the zeta potential measurements in Table 6.1, where the more negative surface potentials lead to higher electrostatic attractions of the MG cations, causing larger equilibrium

constants. DOPG is observed to have higher equilibrium constants than DOPS under the same buffer conditions, in general agreement with the corresponding higher zeta potential magnitudes, to within experimental uncertainty.

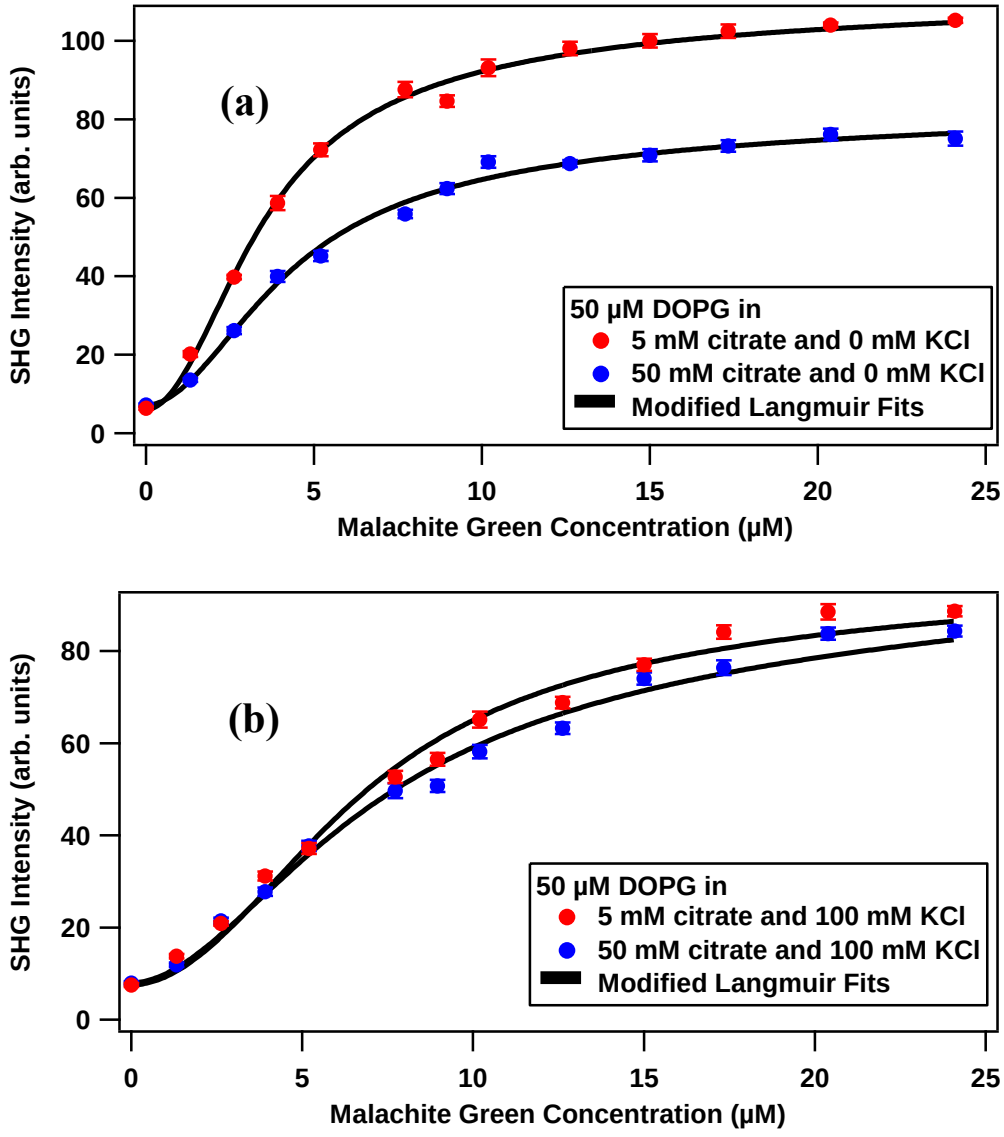

Figure 6.6. SHG-determined adsorption isotherms for MG with DOPG liposomes at different citrate buffer concentrations (5 mM and 50 mM) in the absence of added KCl (a) and with 100 mM added KCl (b). pH = 4.0 citrate buffer is used.

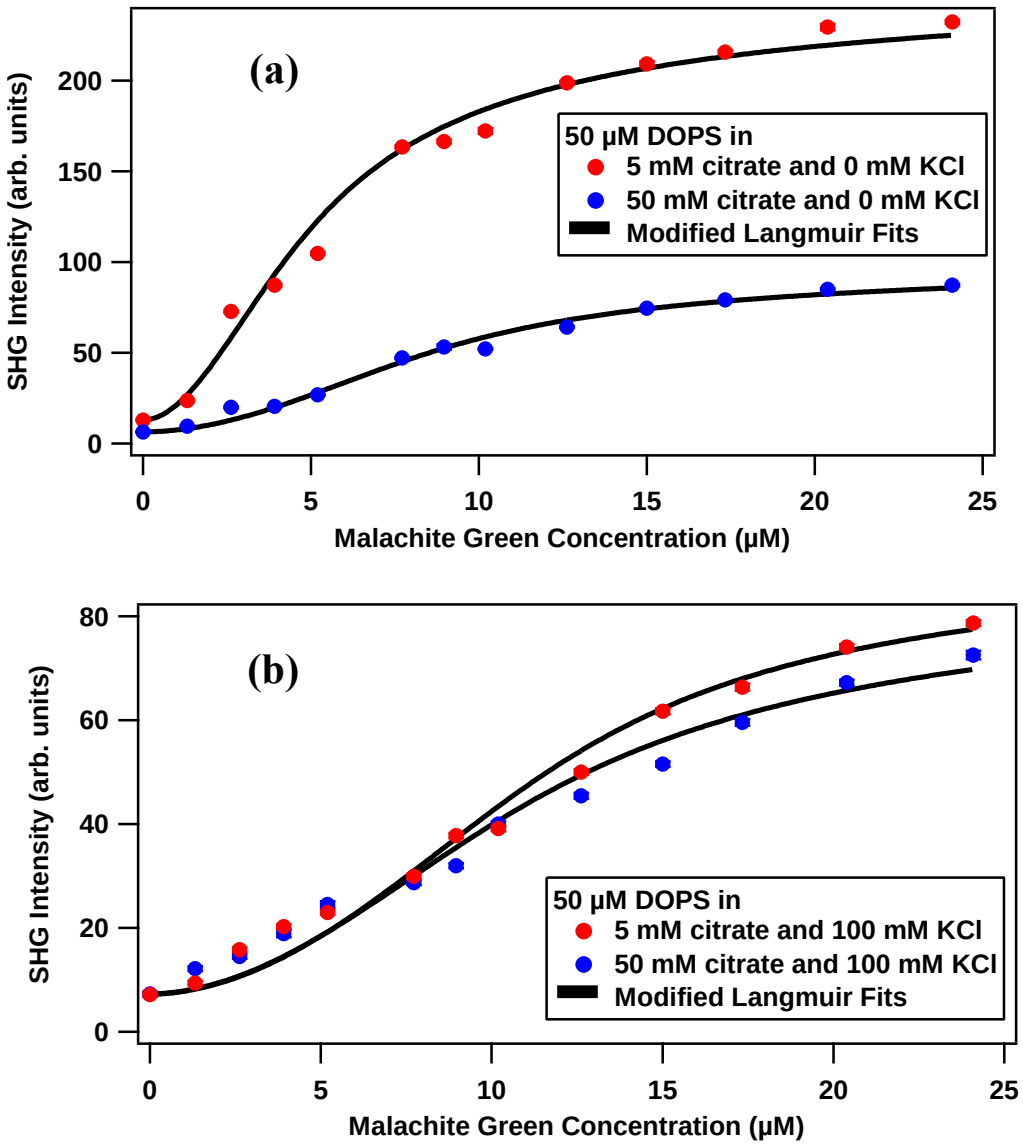

Figure 6.7. SHG-determined adsorption isotherms for MG with DOPS liposomes at different citrate buffer concentrations (5 mM and 50 mM) in the absence of added KCl (a) and with 100 mM added KCl (b). pH = 4.0 citrate buffer is used.

The determined maximum adsorption site concentrations and the corresponding numbers of lipid molecules per adsorption site provide a more nuanced description of the molecular and ion interactions at the liposomes surfaces. For both DOPG and DOPS liposomes, the largest N_{max}

Table 6.2. List of variables and fitting parameters obtained from modified adsorption isotherms.

	DOPG (50 uM)				DOPS (50 uM)			
	Buffer A	Buffer B	Buffer C	Buffer D	Buffer A	Buffer B	Buffer C	Buffer D
K (10^7)	6.7 ± 0.4	5.1 ± 0.4	3.9 ± 0.5	2.7 ± 0.3	4.7 ± 0.6	3.3 ± 0.5	3.1 ± 0.5	2.2 ± 0.4
N_{max} (μM)	2.7 ± 0.2	3.1 ± 0.4	5.6 ± 0.7	4.5 ± 0.8	3.8 ± 0.6	7.4 ± 0.9	11.1 ± 1.1	9.3 ± 1.5
−ΔG (kcal/mol)	10.7 ± 0.1	10.5 ± 0.1	10.4 ± 0.2	10.1 ± 0.2	10.5 ± 0.1	10.3 ± 0.2	10.2 ± 0.2	10.0 ± 0.3
Lipid/site	18.6 ± 1.5	16.2 ± 1.9	9.0 ± 1.2	11.1 ± 2.0	13.0 ± 2.1	6.8 ± 0.8	4.5 ± 0.5	5.4 ± 0.9
A	105.2 ± 0.6	75.1 ± 1.8	88.6 ± 1.1	84.3 ± 1.2	232.4 ± 1.1	87.2 ± 0.7	78.7 ± 0.5	72.5 ± 0.8

values of 5.6 ± 0.7 μM and 11.1 ± 1.1 μM, respectively, occur in buffer C under a low citrate concentration and 100 mM KCl, while the lowest N_{max} values of 2.7 ± 0.2 μM and 3.8 ± 0.6 μM, respectively, occur in buffer A under a lower citrate concentration and no added KCl. Intermediate N_{max} values are observed in buffers B and D, at higher citrate concentrations at no added KCl and 100 mM KCl, respectively, for both DOPG and DOPS liposomes. Here, in the absence of added KCl, the results suggest dye-dye repulsion occurs at the liposome surface, thereby lowering the adsorption site densities. In the presence of 100 mM added KCl, it is posited that greater ion-pair formation occurs, which lowers dye-dye repulsion and stabilizes the adsorbates, allowing for increased N_{max} values. However, with higher citrate concentrations and 100 mM added KCl in buffer D, diminished N_{max} values compared to those in buffer C indicate that additional competition in adsorption between MG, sodium, and potassium occurs. DOPS liposomes possess higher adsorption site densities than the DOPG for all four of the different buffer

conditions. Liposomes of DOPS, with two additional charge centers (carboxylate and ammonium), is expected to have a higher hydration level, [63-64] which may allow for more sites to which MG can adsorb. Additionally, the SHG intensity at saturation, described by A in equation (6.3), is much higher in buffer A compared to buffers B-D for both DOPG and DOPS, even though the corresponding N_{max} values are smaller, indicating that the added salts change the orientation of MG at the liposome surface and decrease the $\chi^{(3)}$ term due to ion screening of the electrostatic surface potential.

The MG dye is also used to study molecular interactions with anionic QPADOPE and neutral DOPC liposomes. QPADOPE liposomes are negatively charged with zeta potentials that are comparable to DOPG and DOPS; however, the charged phosphate site is buried further from the liposome surface due to its molecular structure, as shown in Figure A3.4. The SHG intensities of QPADOPE liposomes in citrate buffer in the presence and absence of KCl upon the addition of MG are similar to the SHG intensities of the dye alone at the corresponding concentrations. Additionally, no decay in the SHG signal over time is observed. This indicates that the MG does not adsorb to the surface of QPADOPE liposomes and is not transported through the lipid bilayer. These results demonstrate that the location of the charged site is important in determining the adsorption properties and transport kinetics of molecules interacting with liposomal surfaces. The quinone is a bulky group which has strong hydrophobic interactions with neighboring head groups, producing a dense shielding layer that prevents malachite green from adsorbing and diffusing in the QPADOPE liposomes. Here, the charged phosphate is buried below the quinone at the liposome surface, so the electrostatic Coulombic attraction with MG in solution is weakened. Similarly, SHG studies of MG interacting with neutral DOPC liposomes in citrate buffer with and without added KCl also point to there being no adsorption and no transport of MG, which is

consistent with previous work on a similar zwitterionic liposome sample of 1-palmitoyl-2-oleoyl-sn-glycero-3-phosphocholine (POPC).[52] DOPC liposomes have much lower zeta potential magnitudes than the anionic DOPG, DOPS, and QPADOPE lipids, giving rise to much weaker electrostatic interactions between the MG cation and the liposome bilayer surface. The SHG time traces of MG in QPADOPE and DOPC liposomes under different buffers conditions are shown in Figure A3.5.

The interactions of methyl green with DOPG, DOPS, DOPC, and QPADOPE liposomes in buffers A and D are also investigated. The structure of MetG is very similar to that of MG, as shown in Figure 6.1, but with MetG possessing two positive charge centers instead of one; nonetheless, their absorption spectra are quite similar, as shown in Figure A3.9. MetG possesses a calculated value of polar surface area (6.25 $Å^2$) that is indistinguishable from that of MG (6.25 $Å^2$), but MetG has a significantly different distribution coefficient D at pH 4.0 (log D of -2.93) as compared to MG (log D of 0.66).[65, 66] Additionally, MetG exhibits comparable SHG signals to MG for nanoparticle adsorption isotherm measurements.[24] The key difference between MG and MetG is that MetG is doubly charged while MG is singly charged. The higher charge of MetG should lead to larger electrostatic attraction of MetG to the liposome surface. However, no adsorption and no transport of MetG is observed for these liposome samples. In Figures 6.8 (a) and (b) are shown the SHG time profiles of DOPG and DOPS liposomes, respectively, in buffer D (pH 4.0, 50 mM citrate and 100 mM KCl) after the addition of 5.2 μM, 14.8 μM, and 27.8 μM MetG. SHG time profiles of MetG added to DOPG and DOPS liposomes in buffer A and to QPADOPE and DOPC liposomes in buffer D are shown in Figures A3.6 and A3.7, respectively. These SHG signals are all constant in time, to within experimental uncertainty with values that are approximately the same as from MetG alone at corresponding concentrations in buffer without any liposomes, as shown in

Figure A3.7 (c). Molecular ions with high charge densities typically have more negative free energies of solvation and tightly-bound solvation shells,[67] as indicated by the much less positive $\log D$ value for MetG. A strong hydration shell may prevent MetG from adsorbing to and transporting through the liposomal surface/bilayer. This demonstrates that electrostatic interactions between the lipid surface and charged molecular dye is not the only important factor for adsorption and transport. Other factors such as the structure of the lipid head group, the extent

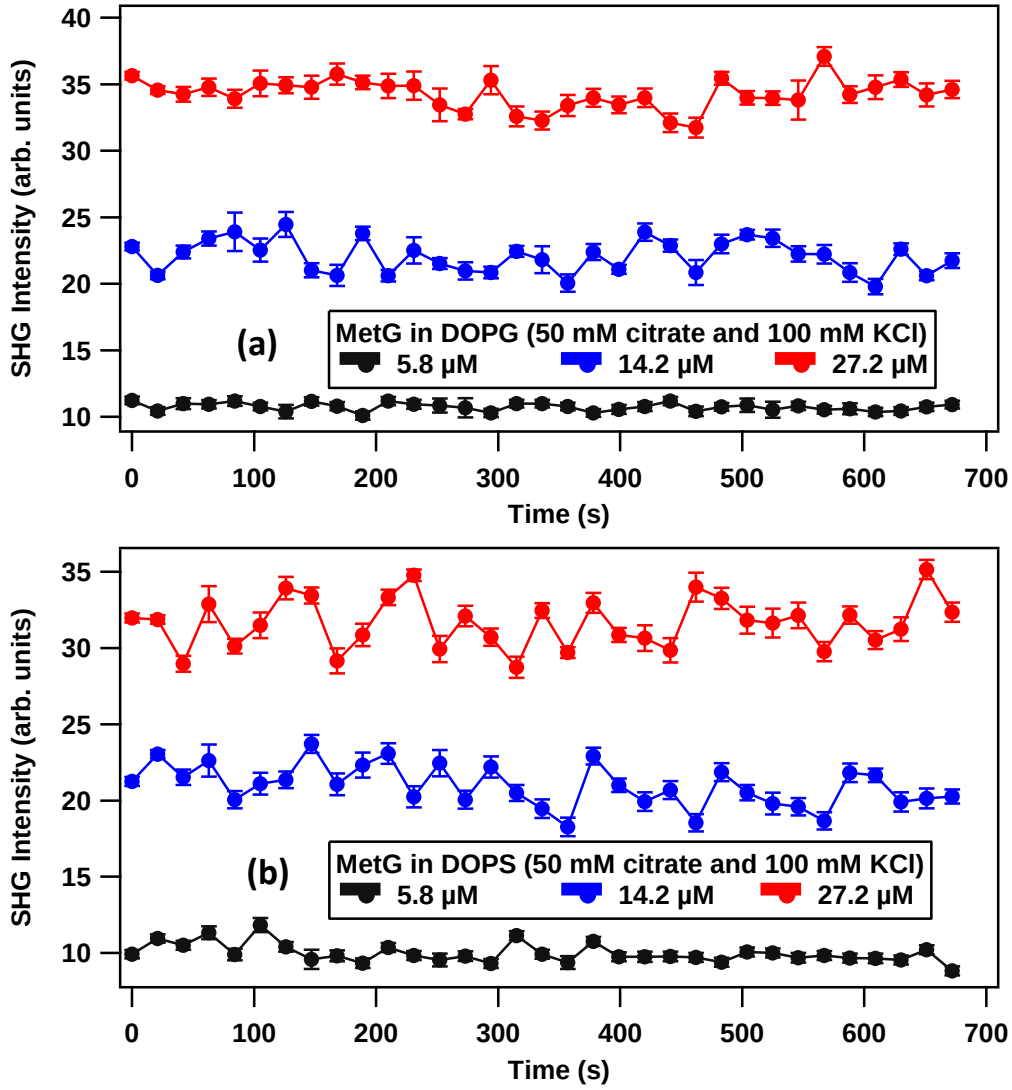

Figure 6.8. SHG time profiles upon addition of various concentrations of methyl green (MetG) to (a) DOPG and (b) DOPS liposomes at lipid concentrations of 50 μM and pH 4.0 citrate buffer.

of hydration around the molecule, and more complicated interactions with salts and buffer ions can all play important roles in the mechanisms involved in molecular adsorption properties and transport kinetics in liposomes. These SHG investigations of liposomes, where both molecular adsorption and transport kinetics are directly compared for different dyes, lipids, and buffer conditions, provide a framework for future studies of fundamental chemical interactions involving phospholipid bilayers in water.

6.5 Conclusions

Time-dependent second harmonic generation is used to study the properties of molecular adsorption and transport of small cationic organic dyes in the presence of different liposomes under varying buffer conditions. The SHG results are analyzed to determine the transport rate constants, free energy of adsorption, and adsorption site density of malachite green interacting with DOPG and DOPS liposomes in citrate buffers at different concentrations with and without added KCl electrolytes. Malachite green is found to adsorb strongly with lower adsorption site densities and faster transport times with liposomes in the absence of added salts. The transport rates vary linearly with malachite green concentration and are slower with added KCl in DOPG liposomes, but the rates exhibit less variation as a function of dye and salt concentration for DOPS liposomes. Additionally, malachite green shows no adsorption and no transport with DOPC and QPADOPE liposomes. SHG studies using the dicationic methyl green dye also show no adsorption and no transport for any of these liposome samples. Factors such as electrostatic interactions between the molecular ions and the charged liposome surface, the structure of the lipid head group, electrolyte adsorption, ion-pair formation, adsorbate-adsorbate repulsion, and hydration of the ions are found to influence the overall adsorption and transport properties. Understanding the complexity of

interactions between molecules, ions, and lipid bilayers is important for advancing potential drug-delivery applications.

6.6 References

1. Pierce, S. K. Invertebrate Cell Volume Control Mechanisms: a Coordinated use of Intracellular Amino Acids and Inorganic Ions as Osmotic Solute. *Biol. Bull.* **1982,** *163*, 405-419.

2. Strange, K. Regulation of Solute and Water Balance and Cell Volume in the Central Nervous System. *J. Am. Soc. Nephrol.* **1992,** *3*, 12-27.

3. Larsen, B.; Pörtner, H.-O.; Jensen, F. Extra-and Intracellular Acid-Base Balance and Ionic Regulation in Cod (Gadus Morhua) During Combined and Isolated Exposures to Hypercapnia and Copper. *Mar. Biol.* **1997,** *128*, 337-346.

4. Alberts, B.; Johnson, A.; Lewis, J.; Raff, M.; Roberts, K.; Walter, P. Carrier Proteins and Active Membrane Transport. *Molecular Biology of the Cell. 4th edition. New York: Garland Science;* **2002**.

5. Finkelstein, A. Water and Nonelectrolyte Permeability of Lipid Bilayer Membranes. *J. Gen. Physiol.* **1976,** *68*, 127-135.

6. Hediger, M. A.; Romero, M. F.; Peng, J.-B.; Rolfs, A.; Takanaga, H.; Bruford, E. A. The ABCs of Solute Carriers: Physiological, Pathological and Therapeutic Implications of Human Membrane Transport Proteins. *Pflügers Archiv* **2004,** *447*, 465-468.

7. Holthuis, J. C.; Menon, A. K. Lipid Landscapes and Pipelines in Membrane Homeostasis. *Nature* **2014,** *510*, 48-57.

8. Lee, A. Lipid–Protein Interactions in Biological Membranes: a Structural Perspective. *Biochim. Biophys.* **2003,** *1612*, 1-40.

9. Walter, A.; Gutknecht, J. Permeability of Small Nonelectrolytes Through Lipid Bilayer Membranes. *J. Membr. Biol.* **1986,** *90*, 207-217.

10. Camenisch, G.; Folkers, G.; van de Waterbeemd, H. Review of Theoretical Passive Drug Absorption Models: Historical Background, Recent Developments and Limitations. *Pharm Acta Helv.* **1996,** *71*, 309-327.

11. Dobson, P. D.; Kell, D. B. Carrier-Mediated Cellular Uptake of Pharmaceutical Drugs: an Exception or the Rule? *Nat. Rev. Drug Discov.* **2008,** *7*, 205-220.

12. Higuchi, W. I. Diffusional Models Useful in Biopharmaceutics. Drug Release Rate Processes. *J. Pharm. Sci.* **1967,** *56*, 315-324.

13. Orsi, M.; Essex, J. W. Passive Permeation Across Lipid Bilayers: a Literature Review. In *Molecular Simulations and Biomembranes. RSC*, 2010; pp 76-90.

14. Schanker, L. Mechanisms of Drug Absorption and Distribution. *Annu Rev Pharmacol.* **1961,** *1*, 29-45.

15. Smith, D.; Artursson, P.; Avdeef, A.; Di, L.; Ecker, G. F.; Faller, B.; Houston, J. B.; Kansy, M.; Kerns, E. H.; Krämer, S. D. Passive Lipoidal Diffusion and Carrier-Mediated Cell Uptake are Both Important Mechanisms of Membrane Permeation in Drug Disposition. *Mol. Pharm.* **2014,** *11*, 1727-1738.

16. Avdeef, A. Physicochemical Profiling (Solubility, Permeability and Charge State). *Curr. Top. Med. Chem.* **2001,** *1*, 277-351.

17. Liu, X.; Testa, B.; Fahr, A. Lipophilicity and its Relationship with Passive Drug Permeation. *Pharm. Res.* **2011,** *28*, 962-977.

18. Pang, K. S. Modeling of Intestinal Drug Absorption: Roles of Transporters and Metabolic Enzymes. *Drug Metab. Dispos.* **2003,** *31*, 1507-1519.

19. Van Meer, G.; Voelker, D. R.; Feigenson, G. W. Membrane Lipids: Where they are and How they Behave. *Nat. Rev. Mol. Cell Biol.* **2008,** *9*, 112-124.

20. Bailey, A. L.; Cullis, P. R. Membrane Fusion with Cationic Liposomes: Effects of Target Membrane Lipid Composition. *Biochem.* **1997,** *36*, 1628-1634.

21. McCarley, R. L. Redox-Responsive Delivery Systems. *Annu. Rev. Anal. Chem.* **2012,** *5*, 391-411.

22. Zeng, J.; Eckenrode, H. M.; Dai, H.-L.; Wilhelm, M. J. Adsorption and Transport of Charged vs. Neutral Hydrophobic Molecules at the Membrane of Murine Erythroleukemia (MEL) Cells. *Colloids Surf., B* **2015,** *127*, 122-129.

23. Wilhelm, M. J.; Sheffield, J. B.; Sharifian Gh, M.; Wu, Y.; Spahr, C.; Gonella, G.; Xu, B.; Dai, H.-L. Gram's Stain Does Not Cross the Bacterial Cytoplasmic Membrane. *ACS Chem. Biol.* **2015,** *10*, 1711-1717.

24. Wilhelm, M. J.; Sheffield, J. B.; Gonella, G.; Wu, Y.; Spahr, C.; Zeng, J.; Xu, B.; Dai, H.-L. Real-Time Molecular Uptake and Membrane-Specific Transport in Living Cells by Optical Microscopy and Nonlinear Light Scattering. *Chem. Phys. Lett.* **2014,** *605*, 158-163.

25. Karam, T. E.; Haber, L. H. Molecular Adsorption and Resonance Coupling at the Colloidal Gold Nanoparticle Interface. *J. Phys. Chem. C* **2013,** *118*, 642-649.

26. Haber, L. H.; Kwok, S. J.; Semeraro, M.; Eisenthal, K. B. Probing the Colloidal Gold Nanoparticle\Aqueous Interface with Second Harmonic Generation. *Chem. Phys. Lett.* **2011,** *507*, 11-14.

27. Campen, R. K.; Zheng, D.-s.; Wang, H.-f.; Borguet, E. Second Harmonic Generation as a Probe of Multisite Adsorption at Solid-Liquid Interfaces of Aqueous Colloid Suspensions. *J. Phys. Chem. C* **2007,** *111*, 8805-8813.

28. Malin, J. N.; Holland, J. G.; Saslow, S. A.; Geiger, F. M. U(VI) Adsorption and Speciation at the Acidic Silica/Water Interface Studied by Resonant and Nonresonant Second Harmonic Generation. *J. Phys. Chem. C* **2011,** *115*, 13353-13360.

29. Malin, J. N.; Hayes, P. L.; Geiger, F. M. Interactions of Ca, Zn, and Cd Ions at Buried Solid/Water Interfaces Studied by Second Harmonic Generation. *J. Phys. Chem. C* **2009,** *113*, 2041-2052.

30. Kumal, R. R.; Karam, T. E.; Haber, L. H. Determination of the Surface Charge Density of Colloidal Gold Nanoparticles Using Second Harmonic Generation. *J. Phys. Chem. C* **2015,** *119*, 16200-16207.

31. Boman, F. C.; Gibbs-Davis, J. M.; Heckman, L. M.; Stepp, B. R.; Nguyen, S. T.; Geiger, F. M. DNA at Aqueous/Solid Interfaces: Chirality-Based Detection via Second Harmonic Generation Activity. *J. Am. Chem. Soc.* **2008,** *131*, 844-848.

32. Liu, Y.; Yan, E. C.; Zhao, X.; Eisenthal, K. B. Surface Potential of Charged Liposomes Determined by Second Harmonic Generation. *Langmuir* **2001,** *17*, 2063-2066.

33. Yan, E. C.; Eisenthal, K. B. Effect of Cholesterol on Molecular Transport of Organic Cations Across Liposome Bilayers Probed by Second Harmonic Generation. *Biophys. J.* **2000,** *79*, 898-903.

34. Kumal, R. R.; Abu-Laban, M.; Landry, C. R.; Kruger, B.; Zhang, Z.; Hayes, D. J.; Haber, L. H. Plasmon-Enhanced Photocleaving Dynamics in Colloidal MicroRNA-Functionalized Silver Nanoparticles Monitored with Second Harmonic Generation. *Langmuir* **2016,** *32*, 10394-10401.

35. Kumal, R. R.; Landry, C. R.; Abu-Laban, M.; Hayes, D. J.; Haber, L. H. Monitoring the Photocleaving Dynamics of Colloidal MicroRNA-Functionalized Gold Nanoparticles Using Second Harmonic Generation. *Langmuir* **2015,** *31*, 9983-9990.

36. Wilhelm, M. J.; Sharifian Gh, M.; Dai, H.-L. Chemically Induced Changes to Membrane Permeability in Living Cells Probed with Nonlinear Light Scattering. *Biochem.* **2015,** *54*, 4427-4430.

37. Kim, J. H.; Kim, M. W. In-Situ Observation of the Inside-to-Outside Molecular Transport of a Liposome. *J. Phys. Chem. B* **2008,** *112*, 15673-15677.

38. Eisenthal, K. B. Second Harmonic Spectroscopy of Aqueous Nano-and Microparticle Interfaces. *Chem. Rev.* **2006,** *106*, 1462-1477.

39. Srivastava, A.; Eisenthal, K. B. Kinetics of Molecular Transport Across a Liposome Bilayer. *Chem. Phys. Lett.* **1998,** *292*, 345-351.

40. Hayes, P. L.; Malin, J. N.; Jordan, D. S.; Geiger, F. M. Get Charged up: Nonlinear Optical Voltammetry for Quantifying the Thermodynamics and Electrostatics of Metal Cations at Aqueous/Oxide Interfaces. *Chem. Phys. Lett.* **2010,** *499*, 183-192.

41. Yan, E. C. Y.; Liu, Y.; Eisenthal, K. B. New Method for Determination of Surface Potential of Microscopic Particles by Second Harmonic Generation. *J. Phys. Chem. B* **1998,** *102*, 6331-6336.

42. Gonella, G.; Dai, H.-L. Second Harmonic Light Scattering from the Surface of Colloidal Objects: Theory and Applications. *Langmuir* **2013,** *30*, 2588-2599.

43. Lütgebaucks, C.; Gonella, G.; Roke, S. Optical Label-Free and Model-Free Probe of the Surface Potential of Nanoscale and Microscopic Objects in Aqueous Solution. *Phys. Rev. B* **2016,** *94*, 195410.

44. Roke, S.; Gonella, G. Nonlinear Light Scattering and Spectroscopy of Particles and Droplets in Liquids. *Annu. Rev. Phys. Chem.* **2012,** *63*, 353-378.

45. Dadap, J. I.; Shan, J.; Heinz, T. F. Theory of Optical Second-Harmonic Generation From a Sphere of Centrosymmetric Material: Small-Particle Limit. *JOSA B* **2004,** *21*, 1328-1347.

46. Darlington, A. M.; Gibbs-Davis, J. M. Bimodal or Trimodal? The Influence of Starting pH on Site Identity and Distribution at the Low Salt Aqueous/Silica Interface. *J. Phys. Chem. C* **2015,** *119*, 16560-16567.

47. Jen, S.-H.; Dai, H.-L.; Gonella, G. The Effect of Particle Size in Second Harmonic Generation From the Surface of Spherical Colloidal Particles. II: The Nonlinear Rayleigh−Gans−Debye Model. *J. Phys. Chem. C* **2010,** *114*, 4302-4308.

48. Dadap, J. I.; Shan, J.; Eisenthal, K. B.; Heinz, T. F. Second-Harmonic Rayleigh Scattering from a Sphere of Centrosymmetric Material. *Phys. Rev. Lett.* **1999,** *83*, 4045-4048.

49. Butet, J.; Brevet, P.-F.; Martin, O. J. Optical Second Harmonic Generation in Plasmonic Nanostructures: from Fundamental Principles to Advanced Applications. *ACS Nano* **2015,** *9*, 10545-10562.

50. Dadap, J. I.; Eisenthal, K. B. Probing the Relative Orientation of Molecules Bound to DNA by Second-Harmonic Generation. *J. Phys. Chem. B* **2014,** *118*, 14366-14372.

51. Matlack, K.; Kim, J.-Y.; Jacobs, L.; Qu, J. Review of Second Harmonic Generation Measurement Techniques for Material State Determination in Metals. *J. Nondesttruct. Eval.* **2015,** *34*, 1-23.

52. Liu, Y.; Yan, E. C.; Eisenthal, K. B. Effects of Bilayer Surface Charge Density on Molecular Adsorption and Transport Across Liposome Bilayers. *Biophys. J.* **2001,** *80*, 1004-1012.

53. Zeng, J.; Eckenrode, H. M.; Dounce, S. M.; Dai, H.-L. Time-Resolved Molecular Transport Across Living Cell Membranes. *Biophys. J.* **2013,** *104*, 139-145.

54. Liu, J.; Subir, M.; Nguyen, K.; Eisenthal, K. B. Second Harmonic Studies of Ions Crossing Liposome Membranes in Real Time. *J. Phys. Chem. B* **2008,** *112*, 15263-15266.

55. Shang, X.; Liu, Y.; Yan, E.; Eisenthal, K. B. Effects of Counterions on Molecular Transport Across Liposome Bilayer: Probed by Second Harmonic Generation. *J. Phys. Chem. B* **2001,** *105*, 12816-12822.

56. Saini, R.; Dube, A.; Gupta, P.; Das, K. Diffusion of Chlorin-p 6 Across Phosphatidyl Choline Liposome Bilayer Probed by Second Harmonic Generation. *J. Phys. Chem. B* **2012,** *116*, 4199-4205.

57. Ong, W.; Yang, Y.; Cruciano, A. C.; McCarley, R. L. Redox-Triggered Contents Release from Liposomes. *J. Am. Chem. Soc.* **2008,** *130*, 14739-14744.

58. McCarley, R. L.; Forsythe, J. C.; Loew, M.; Mendoza, M. F.; Hollabaugh, N. M.; Winter, J. E. Release Rates of Liposomal Contents Are Controlled by Kosmotropes and Chaotropes. *Langmuir* **2013,** *29*, 13991-13995.

59. Rao, Y.; Guo, X.-m.; Tao, Y.-S.; Wang, H.-f. Observation of the Direct S 2→ S 0 Two-Photon Fluorescence Between 370 and 480 nm and the Hyperpolarizability of Crystal Violet (CV) From Spectrally Resolved Hyper-Rayleigh Scattering Measurement. *J. Phys. Chem. A* **2004,** *108*, 7977-7982.

60. Geiger, F. M. Second Harmonic Generation, Sum Frequency Generation, and χ (3): Dissecting Environmental Interfaces with a Nonlinear Optical Swiss Army Knife. *Annu. Rev. Phys. Chem.* **2009,** *60*, 61-83.

61. Friedman, M. H. Free Diffusion. In *Principles and Models of Biological Transport*, Springer: 2008; pp 1-37.

62. Sharifian Gh, M.; Wilhelm, M. J.; Dai, H.-L. Label-Free Optical Method for Quantifying Molecular Transport Across Cellular Membranes In Vitro. *J. Phys. Chem. Lett.* **2016,** *7*, 3406-3411.

63. Petrache, H. I.; Zemb, T.; Belloni, L.; Parsegian, V. A. Salt Screening and Specific Ion Adsorption Determine Neutral-Lipid Membrane Interactions. *Proc. Natl. Acad. Sci.* **2006,** *103*, 7982-7987.

64. Garcia-Manyes, S.; Oncins, G.; Sanz, F. Effect of Ion-Binding and Chemical Phospholipid Structure on the Nanomechanics of Lipid Bilayers Studied by Force Spectroscopy. *Biophys. J.* **2005,** *89*, 1812-1826.

65. Klopman, G.; Li, J.-Y.; Wang, S.; Dimayuga, M. Computer Automated log P Calculations Based on an Extended Group Contribution Approach. *J. Chem. Inf. Model.* **1994,** *34*, 752-781.

66. Ertl, P.; Rohde, B.; Selzer, P. Fast Calculation of Molecular Polar Surface Area as a Sum of Fragment-Based Contributions and its Application to the Prediction of Drug Transport Properties. *J. Med. Chem.* **2000,** *43*, 3714-3717.

67. Hummer, G.; Pratt, L. R.; Garcia, A. E. Free Energy of Ionic Hydration. *J. Phys. Chem.* **1996,** *100*, 1206-1215.

APPENDIX 1

DETERMINATION OF THE SURFACE CHARGE DENSITY OF COLLOIDAL GOLD NANOPARTICLES USING SECOND HARMONIC GENERATION

A1.1 Aggregation Measurements Using Second Harmonic Generation

While the SHG signal is observed to decrease due to the $\chi^{(3)}$ effect at low salt concentrations, as shown in Figures 2.4, 2.5, and 2.7, the SHG signal is observed to increase dramatically at higher salt concentrations due to nanoparticle aggregation. Figure A1.1 shows the SHG signal from the nanoparticle sample when adding much higher NaCl and $MgCl_2$ concentrations, where aggregation begins at around 15 and 0.3 mM, respectively. Corresponding extinction spectroscopy measurements of the gold nanoparticle sample at varying NaCl and $MgCl_2$, shown in Figure A1.2, display no spectral shifts or spectral changes up to 10 mM and 0.08 mM, respectively. At higher concentrations, nanoparticle aggregation is clearly observed in the extinction spectra, in corroboration with the SHG measurements.[1] Aggregation is shown to occur at much lower concentrations for $MgCl_2$, as expected due to the higher valence of the Mg^{2+} ion compared to the Na^+ ion having a much stronger shielding effect.

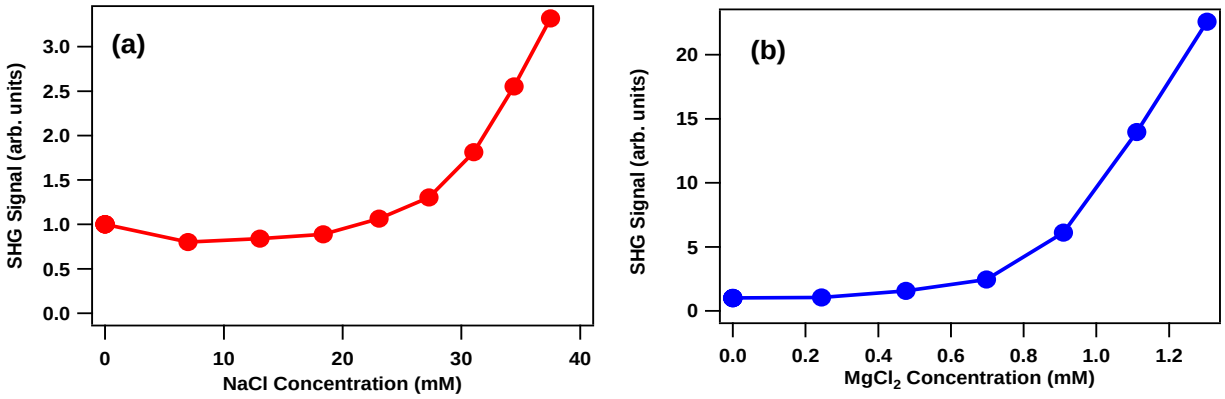

Figure A1.1. SHG signal from the gold nanoparticle sample at higher (a) NaCl and (b) $MgCl_2$ concentrations, showing aggregation. The error bars are smaller than the data points.

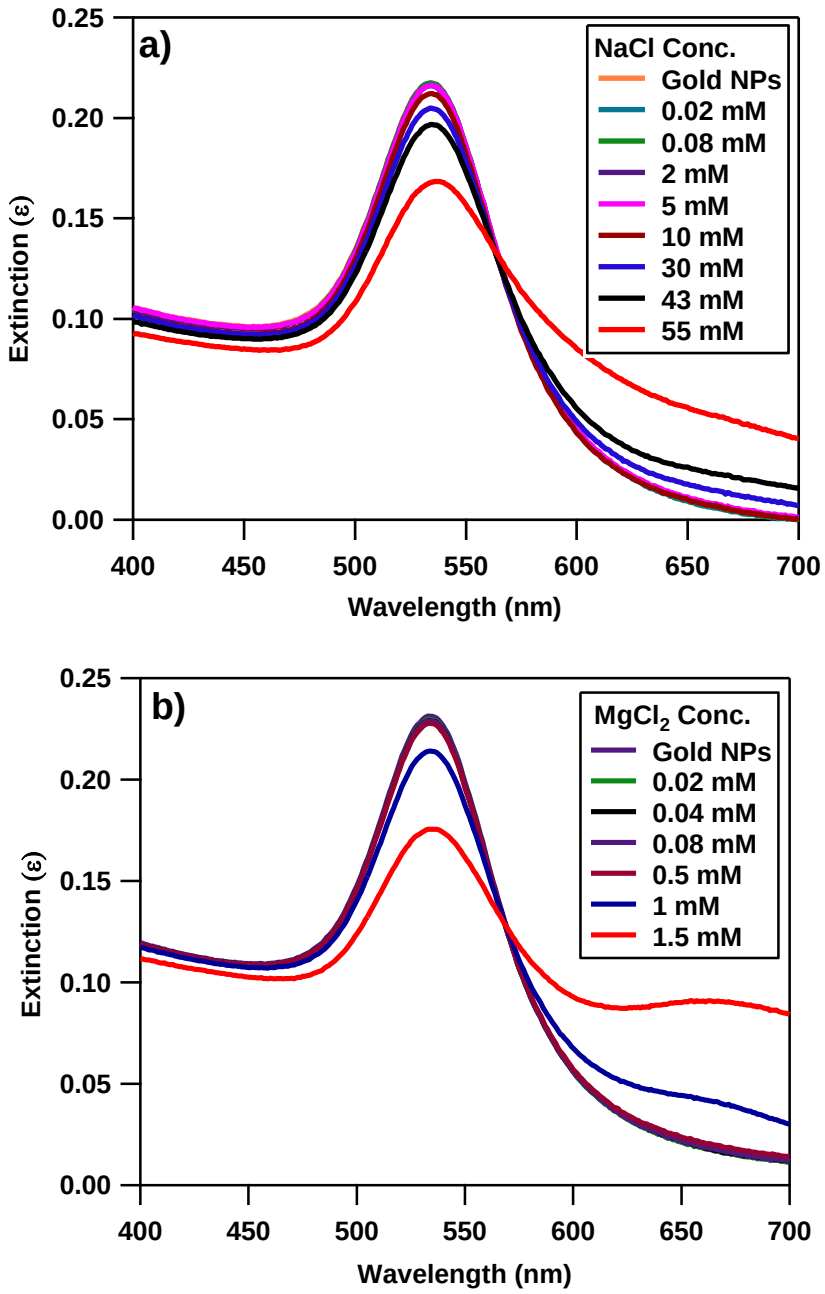

Figure A1.2. Extinction spectra of 50 nm gold nanoparticles as a function of (a) NaCl and (b) $MgCl_2$ salt concentrations. The spectra show that aggregation starts near 6 mM for NaCl and near 0.5 mM for $MgCl_2$.

A1.2 Fitting with Numerical Solutions to the Poisson-Boltzmann Equation

The Poisson-Boltzmann equation is given in equation (1). The Laplacian is equal to $\frac{\partial^2}{\partial x^2}$ for a planar surface and is equal to $\frac{\partial^2}{\partial r^2} + \frac{2}{r}\frac{\partial}{\partial r}$ for the spherical surface. The second-order Runge-Kutta

method is used to solve the spherical Poisson-Boltzmann equation with the boundary conditions that $\left(\frac{\partial \Phi}{\partial r}\right)_{r=a} = -\frac{\sigma}{\varepsilon}$ and that $\Phi(\infty) = 0$.[2-4] Here, the nanoparticle radius a equals 25 nm. The numerical solutions are calculated to find the electrostatic surface potential Φ_0 for many concentrations for both the 1:1 and 2:1 electrolytes, simulating the NaCl and $MgCl_2$ salts, respectively. For large κa values and symmetric electrolytes, the potentials agree with the Gouy-Chapman model, as expected, where κ is the inverse of the Debye length. For the experimental conditions described by Figure 2.7, the κa values range from approximately 0.17 to 0.81 for NaCl and from 0.09 to 0.88 for $MgCl_2$, which are all conditions where the Gouy-Chapman is an inaccurate approximation to the Poisson-Boltzmann equation. Representative surface potentials from the Gouy-Chapman model, using equation (2.2), and from the numerical solutions to the Poisson-Boltzmann equation for a surface charge density σ of -0.0015 C/m^2 are shown in Figure A1.3.

In order to fit the experimental measurements of the SHG electric field as a function of the salt concentration C for the gold nanoparticle sample to the numerical solutions to the Poisson-Boltzmann equation, correction factors that depend on C and σ are determined to relate the Gouy-Chapman model to the numerical solutions for nanoparticles with a 25 nm radius. First, a trial value of σ is used for both the Gouy-Chapman model and numerical solutions to obtain the surface potentials, Φ_0^{GC} and Φ_0^{ns}, respectively for both the 1:1 and 2:1 electrolytes. Here, for the Gouy-Chapman calculation, z equals 1 for the 1:1 electrolyte, and z is taken as 2 for the 2:1 electrolytes, as explained earlier. The surface potentials are calculated for seven equally spaced concentrations from 0.1 μM to 2 μM and for fifteen equally spaced concentrations from 2 μM to 90 μM for the 1:1 electrolyte. Similarly, the surface potentials are calculated for seven equally spaced concentrations from 0.01 μM to 0.3 μM and for fifteen equally spaced concentrations from 0.3

μM to 42 μM for the 2:1 electrolyte. Next, a concentration-dependent correction factor given by $f(C) = [\Phi_0^{ns}(C)/\Phi_0^{GC}(C)]$ is calculated and fit to a double-exponential given by $f(C) = A_1\exp(-C/b_1) + A_2\exp(-C/b_2) + y_0$. Representative calculated correction factors as a function of salt concentration are shown in Figure A1.4 along with the double-exponential best fits. These steps are repeated for five different σ values ranging from −0.0025 C/m^2 to −0.0005 C/m^2. The corresponding double-exponential fit parameters, A_1, A_2, b_1, b_2, and y_0 for the 1:1 and 2:1 electrolytes are shown in Figure A1.5 as a function of surface charge density σ. These parameters are each fit to separate quadratic polynomials as a function of σ. This provides correction factors that are functions of both C and σ over the range of values investigated experimentally. Finally the experimental results of the SHG measurements are fit using $E_{SHG} = A + B\Phi_0$ where $\Phi_0 = f(C,\sigma)\,\Phi_0^{GC}(C,\sigma)$ for both the NaCl and $MgCl_2$ using the correction factor best fits. These numerical solution best fits are done for the case where ion adsorption is neglected and for the case where ion adsorption is included, as described in the paper.

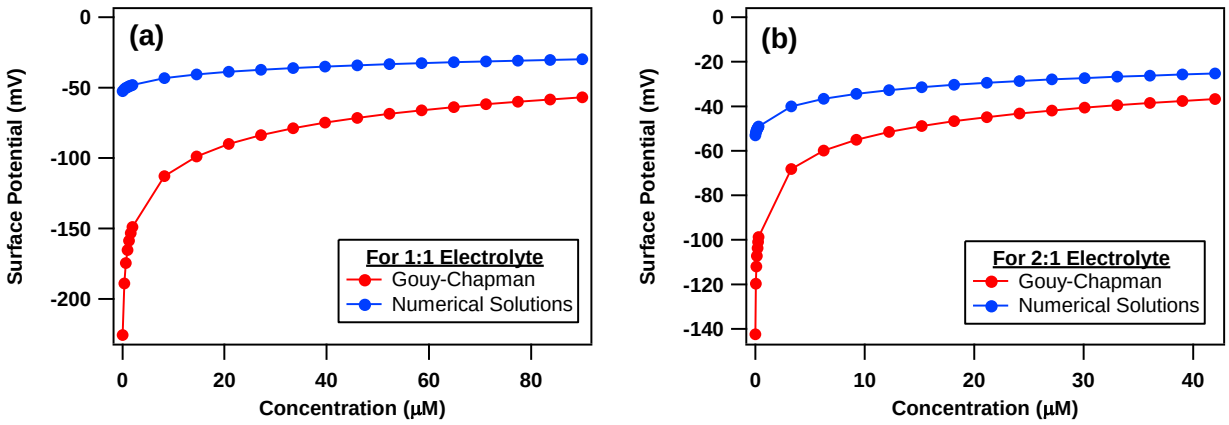

Figure A1.3. The calculated electrostatic surface potentials as a function of the salt concentration for (a) the 1:1 electrolyte and (b) the 2:1 electrolyte for a surface charge density of -0.0015 C/m^2 using the Gouy-Chapman model (red circles) and numerical solutions to the Poisson-Boltzmann equation for a nanoparticle with a 25 nm radius (blue circles).

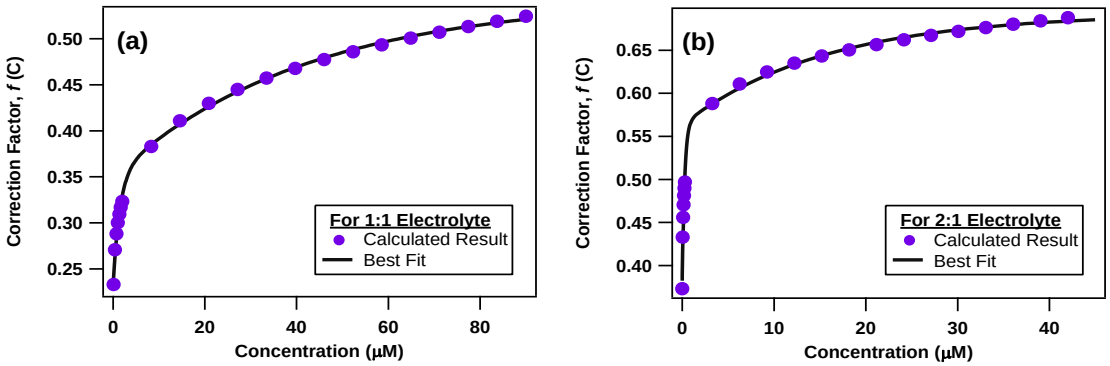

Figure A1.4. Calculated correction factors for (a) a 1:1 electrolyte and (b) a 2:1 electrolyte as a function of salt concentration for a surface charge density of -0.0015 C/m^2 and a nanoparticle with a 25 nm radius (purple circles) along with the corresponding double-exponential best fits (black curves).

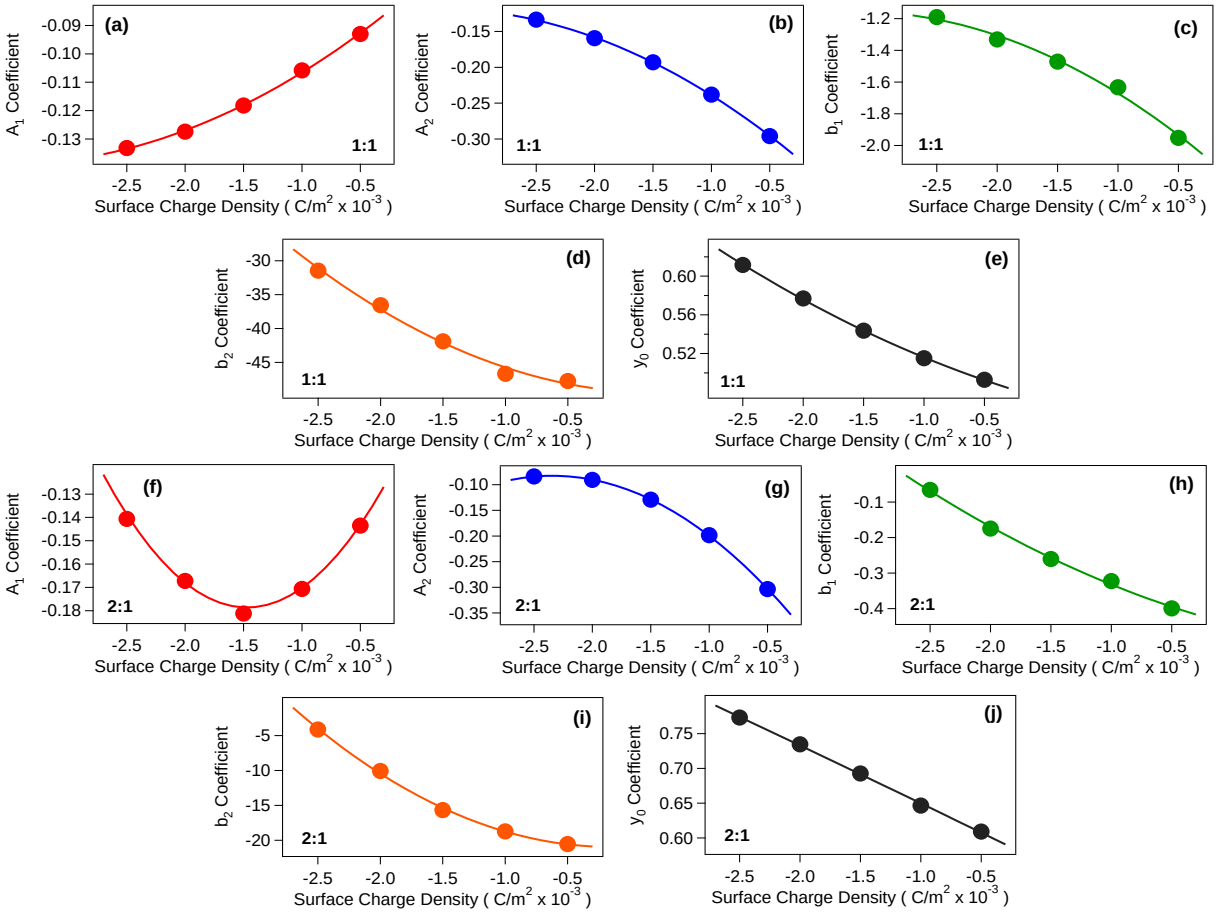

Figure A1.5. The double-exponential fit parameters, (a) A_1, (b) A_2, (c) b_1, (d) b_2, and (e) y_0 for 1:1 electrolytes and (f) A_1, (g) A_2, (h) b_1, (i) b_2, and (j) y_0 for 2:1 electrolytes corresponding to the correction factors as a function of surface charge density σ. These calculated fit parameters (solid circles) are each fit to quadratic polynomials (solid lines) as a function of σ.

The resulting surface potentials corresponding to the best fits to the SHG experimental measurements using the three models described in the manuscript as a function of added salt concentration for NaCl and $MgCl_2$ are shown in Figure A1.6 (a) and (b), respectively. These calculated results are compared to the zeta potential measured before the addition of salts, showing that the numerical solutions to the Poisson-Boltzmann equation including ion adsorption provides the best agreement.

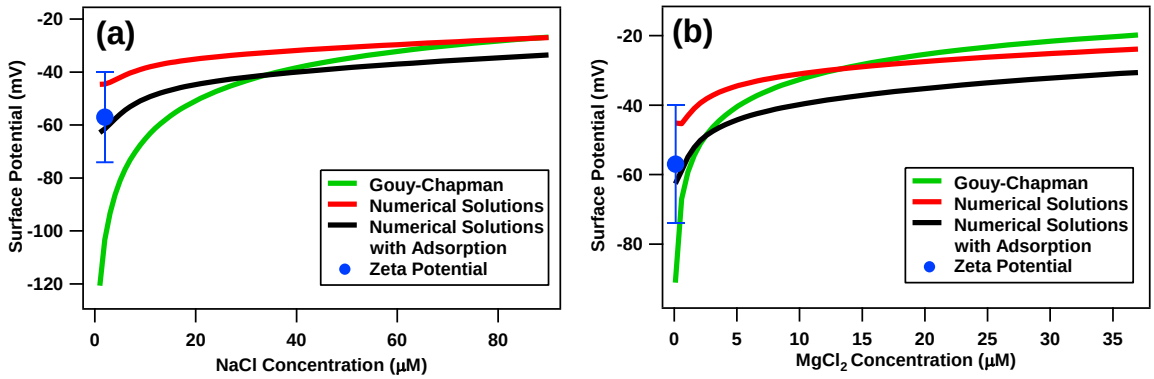

Figure A1.6. Surface potential as a function of added (a) NaCl and (b) $MgCl_2$ salt concentrations using the best fits calculated using the Gouy-Chapman model (green curves) and numerical solutions to the Poisson-Boltzmann equation without ion adsorption (red curves) and with ion adsorption (black curves). The measured zeta potential before the addition of salt is also shown for comparison.

A1.3 References

1. Vance, F. W.; Lemon, B. I.; Hupp, J. T. Enormous Hyper-Rayleigh Scattering From Nanocrystalline Gold Particle Suspensions. *J. Phys. Chem. B* **1998,** *102*, 10091-10093.

2. Hiemenz, P. C.; Rajagopalan, R. *Principles of Colloid and Surface Chemistry, Revised and Expanded*. 3rd ed.; CRC Press: New York, USA, 1997.

3. Ohshima, H.; Healy, T. W.; White, L. R. Accurate Analytic Expressions for the Surface Charge Density/Surface Potential Relationship and Double-Layer Potential Distribution for a Spherical Colloidal Particle. *J. Colloid Interface Sci.* **1982,** *90*, 17-26.

4. Tuinier, R. Approximate Solutions to the Poisson–Boltzmann Equation in Spherical and Cylindrical Geometry. *J. Colloid Interface Sci.* **2003,** *258*, 45-49.

APPENDIX 2

PLASMON-ENHANCED PHOTOCLEAVING DYNAMICS IN COLLOIDAL MICRORNA-FUNCTIONALIZED SILVER NANOPARTICLES USING SECOND HARMONIC GENERATION

A2.1 Scheme of Photocleaving Process

The nitrobenzyl photocleaveable linker is a commonly used linker utilized for its high cleaving efficiency under UV irradiation.[1-3] The photolytic mechanism is understood to follow the nitro group reduction to nitroso and oxidation of the benzylic carbon through the *aci*-nitro anion intermediate to release the phosphate ester.[4] Scheme A2.1 shows the structure of the photocleavable (PC) miRNA-148b functionalized nanoparticles before and after UV irradiation.

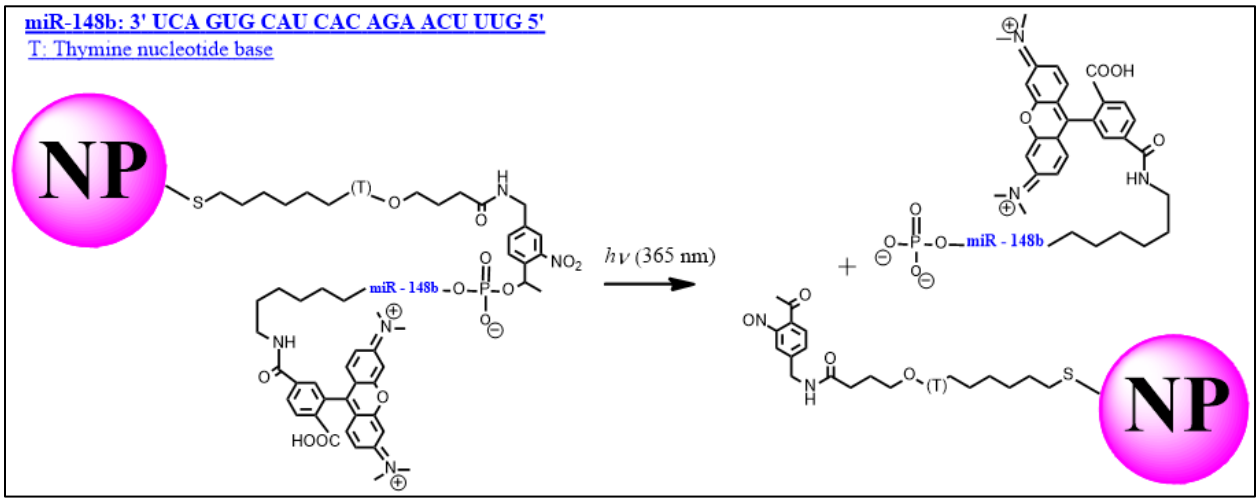

Scheme A2.1: Details of the sequences and the photocleaving process. The alkyl thiol linker attaches to the nanoparticle surface and connects through the PC-linker to the miRNA that is labeled with the 6-TAMARA fluorophore.

A2.1 Fluorescence Measurement

Additional fluorescence measurements are taken on the colloidal silver nanoparticles (SNPs) and the miRNA-functionalized SNPs labeled with the 6-TAMRA fluorophore. When

excited with 531 nm, negligible emission is observed from the SNP sample. However, a strong emission peak centered at 572 nm is observed from the miRNA-functionalized SNPs due to the labeled 6-TAMRA fluorophore, as shown in Figure A2.1.

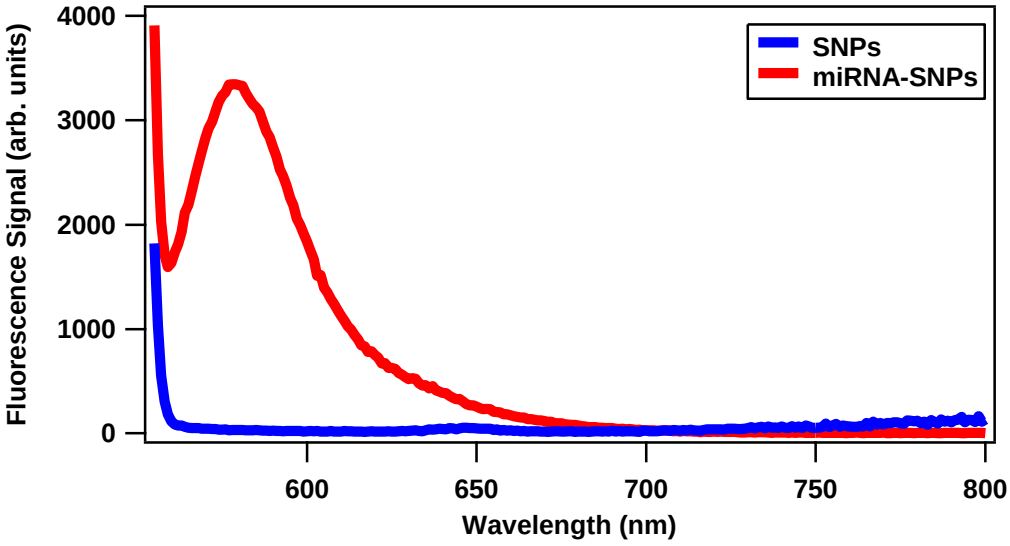

Figure A2.1. Fluorescence signal of the SNPs before and after miRNA functionalization.

A2.3 Power Dependent Analysis in miRNA-PSNP

MiRNA-functionalized PSNPs are irradiated at different laser powers at 365 nm and the time-dependent SHG electric fields are shown in Figure A2.2. The rate constants from the miRNA-functionalized PSNPs obtained at the laser powers of 15, 25, 35, 60, and 85 mW are (0.9 ± 0.3) x 10^{-3} s^{-1}, (1.3 ± 0.3) x 10^{-3} s^{-1}, (1.8 ± 0.2) x 10^{-3} s^{-1}, (3.5 ± 0.3) x 10^{-3} s^{-1} and (4.5 ± 0.3) x 10^{-3} s^{-1}, respectively. These power-dependent photocleaving rates are much lower than the corresponding rates from the miRNA-functionalized SNP sample shown in the manuscript.

A2.4 Zeta Potential Measurement

The controlled release of miRNA from the surface of the SNPs as a function of UV irradiation time is studied using a zeta potential measurements. The zeta potential of the miRNA-SNPs increases to less negative values under increasing UV irradiation times, as shown in Figure

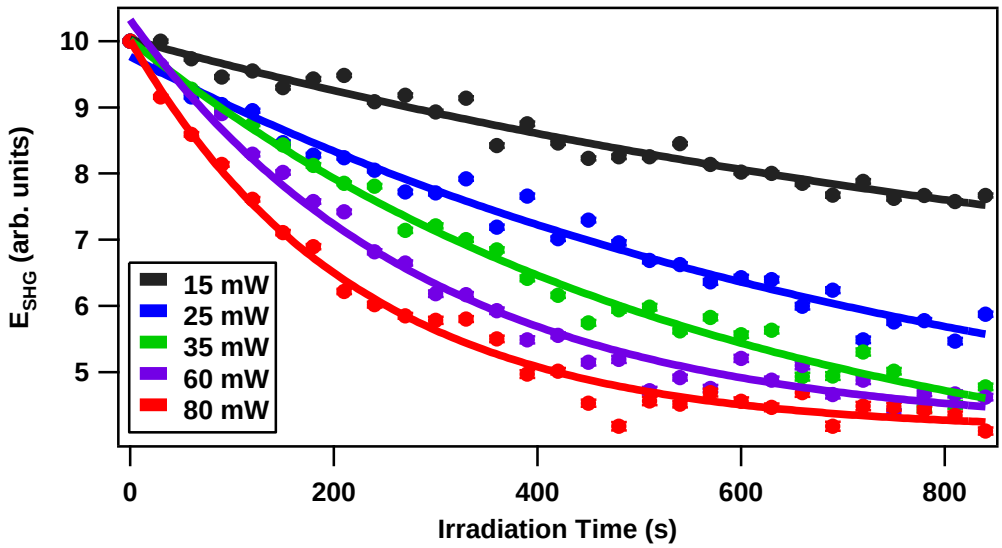

Figure A2.2. Measured SHG electric fields from miRNA-functionalized PSNPs as a function of irradiation time with 365 nm at different UV laser average powers with corresponding exponential fits.

A2.3 (a) and (b). Figure A2.3 (a) shows electrophoretic mobilities of the miRNA-functionalized SNPs at different UV irradiation times using 365 nm irradiation at an average power of 20 mW. The electrophoretic motilities at 0 min, 0.5 min and 14 min are $(3.9 \pm 0.6) \times 10^{-8}$ m^2/Vs, $(3.5 \pm 0.5) \times 10^{-8}$ m^2/Vs and $(2.5 \pm 0.5) \times 10^{-8}$ m^2/Vs, respectively. The corresponding zeta potentials are –74.8 ± 11.4 mV, –66.7 ± 9.6 mV and –48.3 ± 10.3 mV for 0 min, 0.5 min and 14 min of UV irradiation, respectively, using Huckel's aproximation. The zeta potential of the miRNA-functionalized SNPs after 14 min of photolysis is equal to the zeta potential of the original SNPs

sample, −49.8 ± 10.2 mV, to within experimental uncertainty. Figure A2.3 (b) shows the zeta potential of the miRNA-functionalized SNPs as a function of UV irradiation time.

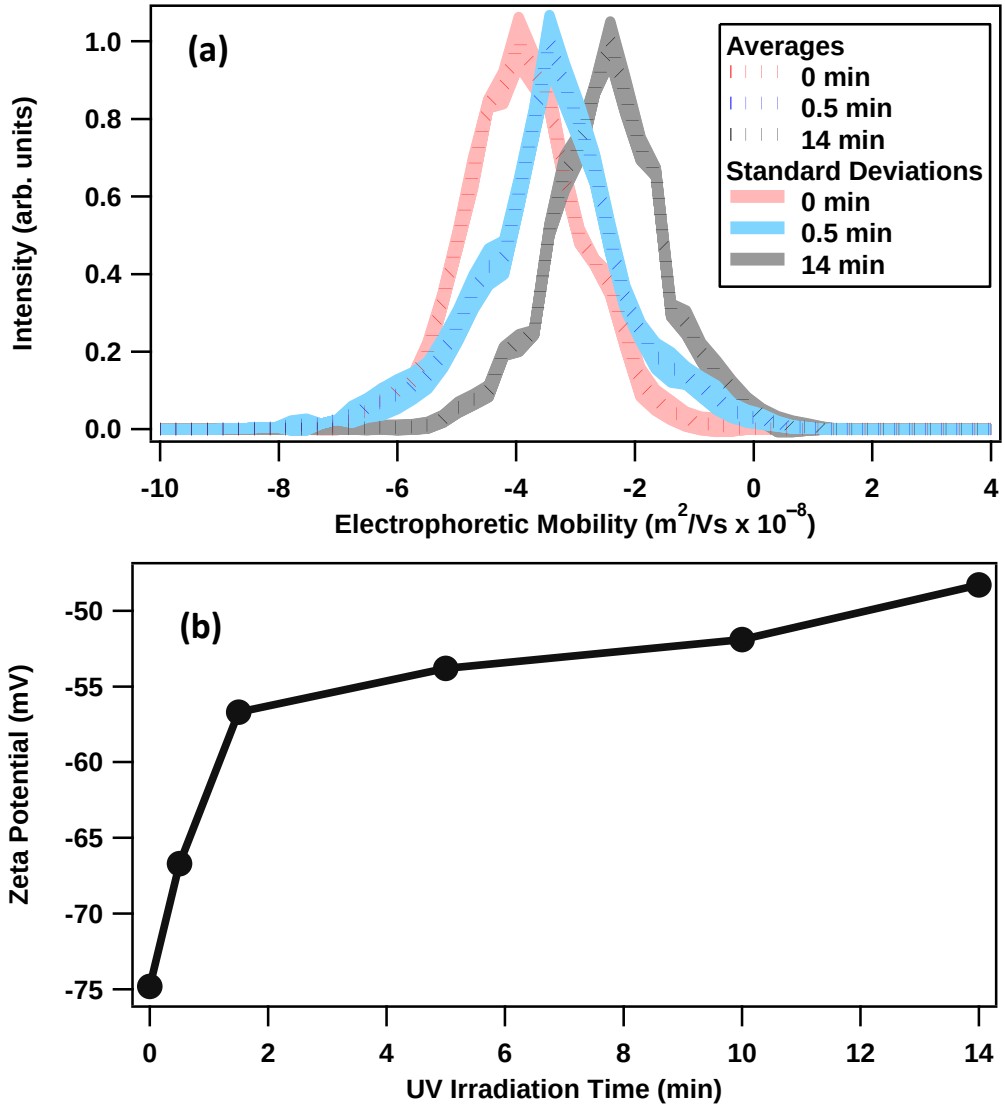

Figure A2.3. (a) The electrophoretic mobility of the miRNA-functionalized SNPs under different UV irradiation times. (b) Zeta potential of the miRNA-functionalized SNPs under varying UV irradiation times.

A2.5 References

1. Kim, M. S.; Diamond, S. L. Photocleavage of O-Nitrobenzyl Ether Derivatives for Rapid Biomedical Release Applications. *Bioorg. Med. Chem. Lett.* **2006,** *16*, 4007-4010.

2. Bai, X.; Li, Z.; Jockusch, S.; Turro, N. J.; Ju, J. Photocleavage of a 2-Nitrobenzyl Linker Bridging a Fluorophore to the 5′ end of DNA. *Proc. Natl. Acad. Sci.* **2003,** *100*, 409-413.

3. Kumal, R. R.; Landry, C. R.; Abu-Laban, M.; Hayes, D. J.; Haber, L. H. Monitoring the Photocleaving Dynamics of Colloidal MicroRNA-Functionalized Gold Nanoparticles Using Second Harmonic Generation. *Langmuir* **2015,** *31*, 9983-9990.

4. McCray, J. A.; Trentham, D. R. Properties and Uses of Photoreactive Caged Compounds. *Annu. Rev. Biophys. Biophys. Chem.* **1989,** *18*, 239-270.

APPENDIX 3

IMPACTS OF SALT, BUFFER, AND LIPID NATURE ON MOLECULAR ADSORPTION AND TRANSPORT IN LIPID BILAYER AS OBSERVED BY SECOND HARMONIC GENERATION

A3.1 Lipid Concentration Determination and Liposome Size Distributions

A Bartlett assay is used to determine the lipid concentration in the liposome samples. A set of phosphate standards is prepared in triplicate in the range of 10 nmole to 130 nmole. An appropriate volume of 0.65 mM phosphate standard is placed in a 10 mL disposable glass test tube. 10 µL of the vesicle solution is also aliquoted into separate test tubes in triplicate. 0.4 mL of 70% perchloric acid ($HClO_4$) is added to each test tube and the test tubes are placed in a heating block at 180 °C for 30 min. The test tubes are allowed to cool down to room temperature before adding 4.6 mL of 0.22% ammonium molybdate ($(NH_4)_6Mo_7O_{24}$) in 0.125 M sulfuric acid and 0.2 mL of a prepared 0.16 g/mL Fiske-Subbarow reducer solution from Sigma Aldrich. These test tubes are vortexed and placed in a 100 °C water bath for 10 min. The presence of phosphorus is apparent by the formation of an aqua-blue color in the solution. Absorbance at 800 nm of the phosphorus-

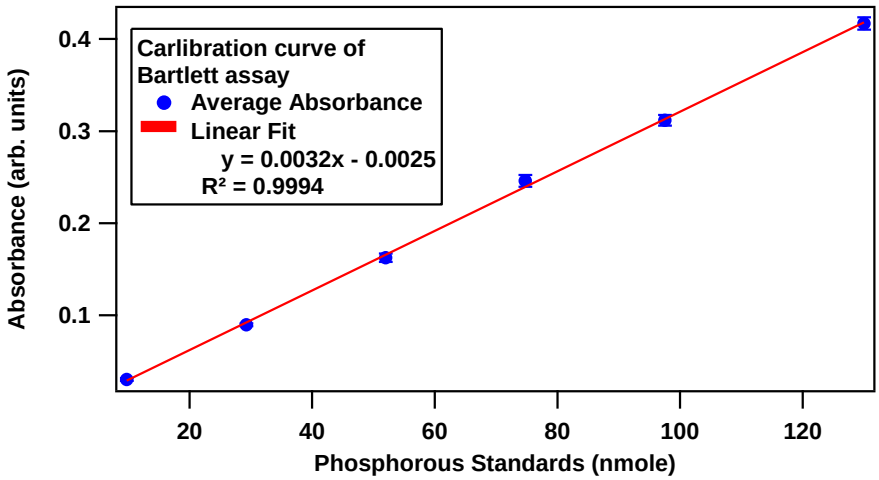

Figure A3.1. Bartlett assay calibration for determining the lipid concentration.

molybdate complex is directly measured from the test tubes without dilution using a UV-Vis spectrometer. The calibration curve for the Bartlett assay is shown in Figure A3.1. The liposome size distributions are measured by dynamic light scattering (DLS). Representative size distributions for DOPG, DOPS, DOPC, and QPADOPE liposomes in 50 mM citrate and 100 mM KCl at pH 4.0 are shown in Figure A3.2. These measured average sizes correspond to 153 nm ± 29 nm, 155 nm ± 33 nm, 156 nm ± 41 nm, and 154 nm ± 36 nm, respectively. DLS measurements of these liposomes in all buffer solutions A-D show the same size distributions, to within experimental uncertainty.

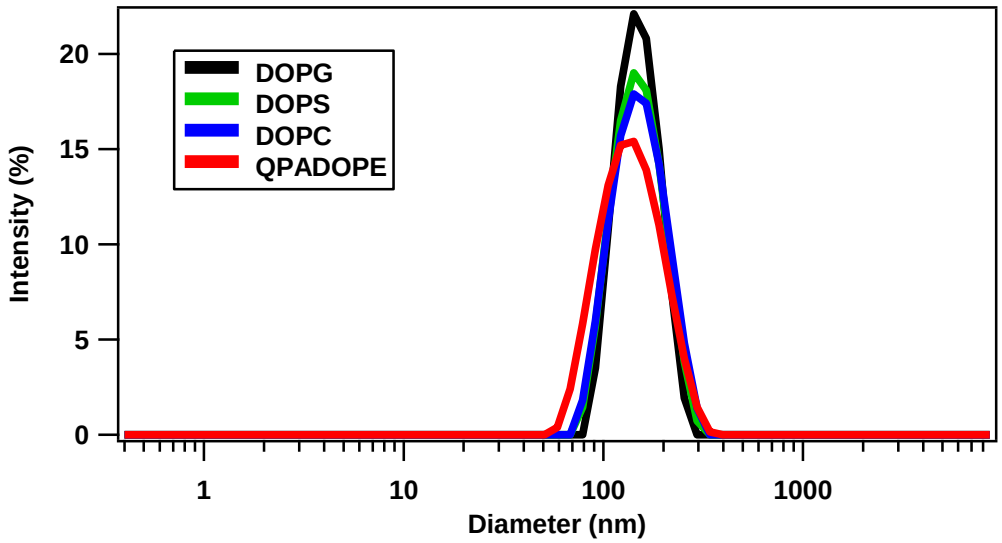

Figure A3.2. Size distributions measured by dynamic light scattering for DOPG, DOPS, DOPC, and QPADOPE liposomes.

Additional Details on SHG Measurements of Molecular Interactions with Liposomes

The transport times of MG through DOPG and DOPS liposome bilayers in the various buffer solutions are listed in Table A3.1. Figure A3.3 shows the variation of transport rate constants τ^{-1} as a function of malachite green concentration. For DOPG, the transport rate constants vary linearly with the dye concentration whereas there is no clear linear variation for DOPS. The molecular structures of tri-methyl quinone dioleoylphosphoethanolamine (QPADOPE) and

dioleoylphosphocholine (DOPC) liposomes are shown in Figure A3.4. The interaction of malachite green with QPADOPE and DOPC liposomes is studied in 50 mM citrate buffer in the absence of KCl and with 100 mM added KCl. Neither transport nor adsorption of malachite green is observed in these liposomes, as shown in the Figure A3.5. Figure A3.5 (e) displays the results from control experiments where the SHG intensity of malachite green dye in the buffer solution is measured as a function of time in the absence of liposomes for direct comparison. The SHG signal after the addition of malachite green in the liposome samples is comparable with the signal from the malachite green in the absence of liposomes at their corresponding concentrations, with no change in SHG signal over time to within experimental uncertainty. Similarly, SHG studies of methyl green in DOPG, DOPS, QMEDOPE, and DOPC liposome samples in different buffer conditions are conducted. The results, shown in Figures A3.6 and A3.7 demonstrate that methyl green does not adsorb to these liposome surfaces and does not transport through these liposome bilayer membranes. The SHG signal from MG alone as a function dye concentration in the different buffer solutions is shown in Figure A3.8. Figure A3.9 shows the absorption spectra of MG and MetG in citrate buffer at pH 4.0 at different times. The absorption spectra are constant with time, showing the stability of the dyes in citrate buffer. However, in phosphate buffer (PBS) at a 50 mM concentration, the hydroxylation reaction of MG and MetG over time causes significant changes in the corresponding absorption spectra, as shown in Figure A3.10.

Error Analysis of Fits

The R^2-values for the fits describing the time-dependent exponential functions for the molecular transport studies are shown in Table SA3.2. The R^2-values for the fits describing the modified Langmuir functions for the molecular adsorption studies are shown in Table 3.3. All error bars presented from fits correspond to standard deviations.

Table A3.1. Transport times of malachite green in DOPG and DOPS liposomes under different buffer conditions. N/M indicates data were not measured.

	Transport time (s)							
	DOPG				DOPS			
MG (μM)	Buffer A	Buffer B	Buffer C	Buffer D	Buffer A	Buffer B	Buffer C	Buffer D
1.3	285 ± 18	345 ± 54	426 ± 24	767 ± 57	510 ± 53	396 ± 49	360 ± 67	279 ± 16
2.6	256 ± 25	325 ± 25	385 ± 35	567 ± 50	576 ± 86	434 ± 56	395 ± 59	291 ± 66
3.8	156 ± 12	276 ± 25	320 ± 24	438 ± 76	N/M	N/M	N/M	N/M
5.2	119 ± 7	200 ± 20	254 ± 25	377 ± 71	411 ± 34	466 ± 69	624 ± 51	436 ± 83
7.7	87 ± 10	134 ± 7	205 ± 40	241 ± 24	271 ± 24	235 ± 55	443 ± 66	295 ± 25
10.2	61 ± 6	90 ± 7	143 ± 18	220 ± 53	265 ± 23	196 ± 11	395 ± 32	269 ± 17
12.6	59 ± 4	77 ± 10	125 ± 6	199 ± 25	261 ± 19	141 ± 13	353 ± 35	247 ± 22
15.0	55 ± 2	72 ± 4	119 ± 3	146 ± 20	N/M	N/M	N/M	N/M
20.0	N/M	N/M	N/M	N/M	257 ± 23	141 ± 11	368 ± 42	244 ± 22

Table A3.2. R^2-values of time-dependent exponential fits. N/M indicates data were not measured.

MG (μM)	R^2-values of exponential fits							
	DOPG				DOPS			
	Buffer A	Buffer B	Buffer C	Buffer D	Buffer A	Buffer B	Buffer C	Buffer D
1.3	0.99	0.95	0.94	0.87	0.96	0.84	0.94	0.85
2.6	0.97	0.99	0.98	0.95	0.98	0.96	0.97	0.90
3.8	0.97	0.98	0.97	0.96	N/M	N/M	N/M	N/M
5.2	0.98	0.96	0.99	0.95	0.99	0.88	0.97	0.95
7.7	0.94	0.98	0.99	0.97	0.98	0.91	0.97	0.98
12.6	N/M	N/M	N/M	N/M	0.98	0.95	0.98	0.97
15.0	0.99	0.98	0.91	0.91	N/M	N/M	N/M	N/M
20.0	N/M	N/M	N/M	N/M	0.98	0.97	0.98	0.95

Table A3.3. R^2-values of modified Langmuir isotherm fits.

Buffer	R^2-values of isotherm fits	
	DOPG	DOPS
A	0.998	0.990
B	0.996	0.992
C	0.991	0.990
D	0.993	0.987

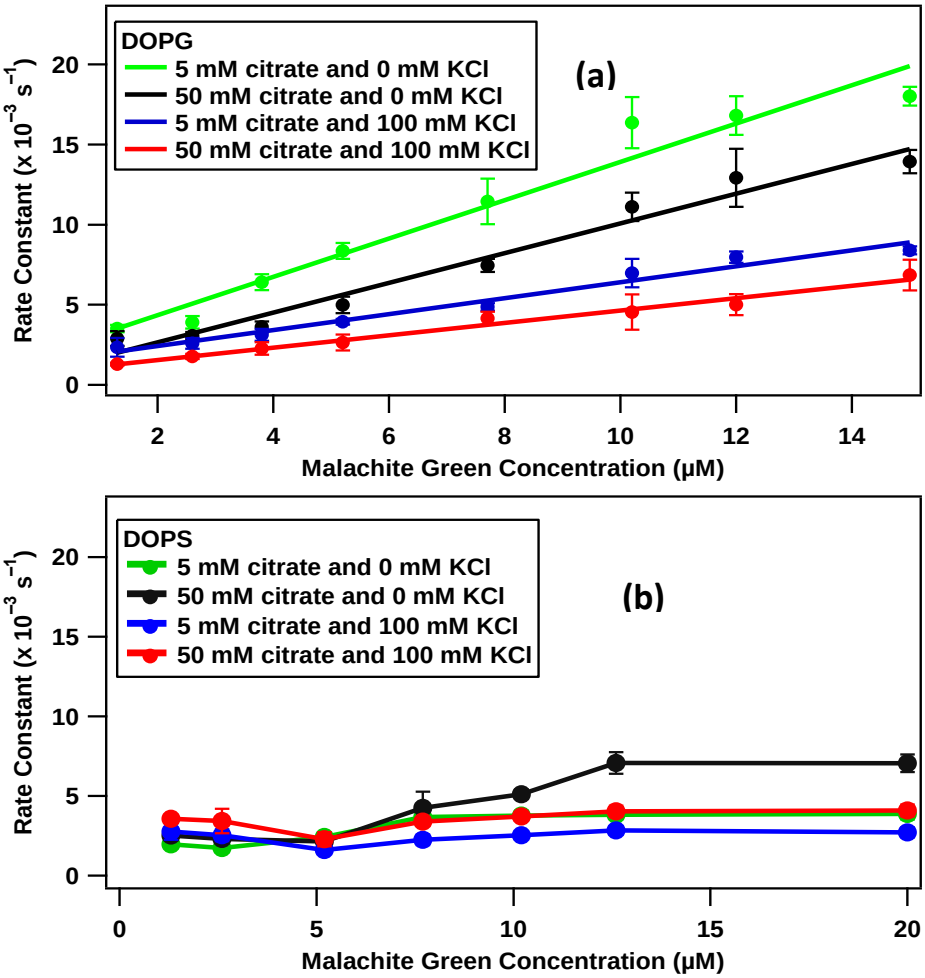

Figure A3.3. Variation of the transport rate constant ($1/\tau$) as a function of malachite green concentration for (a) DOPG and (b) DOPS liposomes at different citrate (pH 4.0) and KCl concentrations.

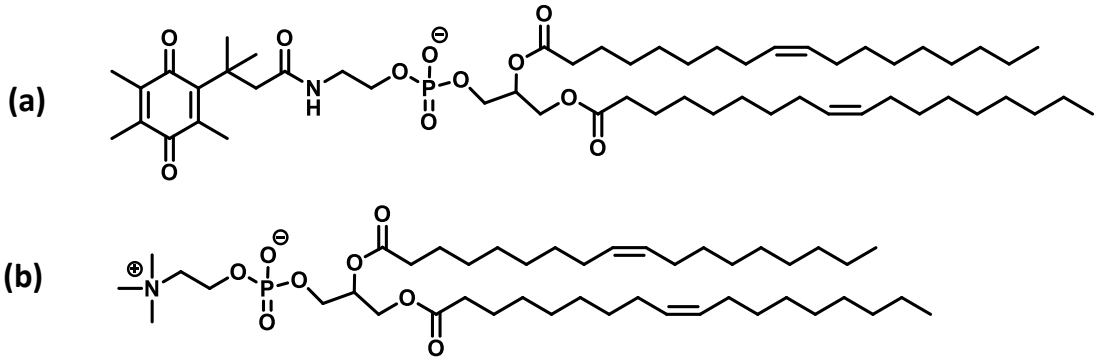

Figure A3.4. Molecular structures of (a) QPADOPE and (b) DOPC, respectively.

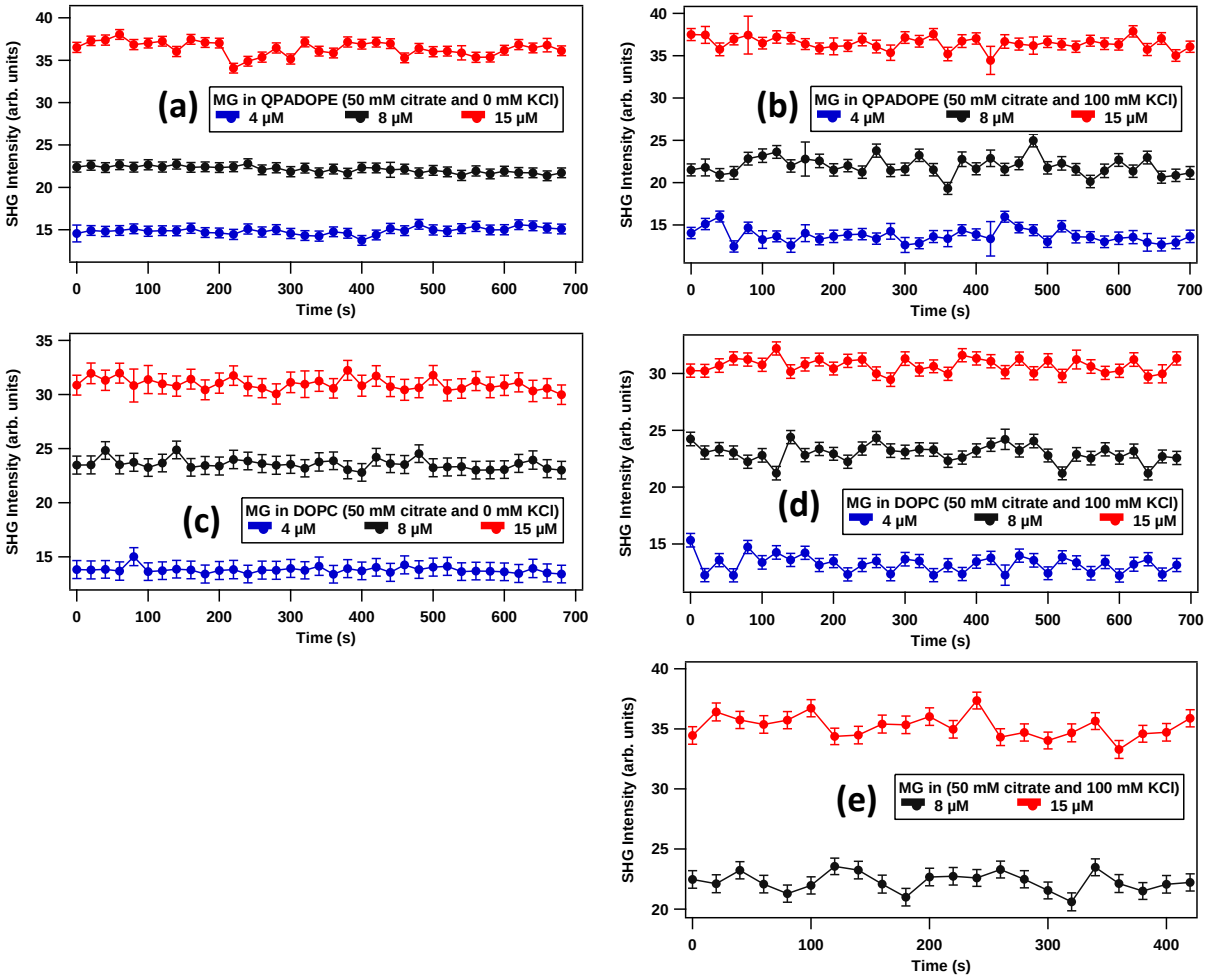

Figure A3.5. SHG data at pH 4.0 showing no adsorption to and no transport of MG for QDOPE liposomes in 50 mM citrate buffer with (a) 0 mM KCl and (b) 100 mM KCl, and DOPC liposomes in 50 mM citrate buffer with (c) 0 mM KCl and (d) 100 mM KCl, under various MG concentrations. SHG data of MG alone (e) in pH 4.0, 50 mM citrate buffer with 100 mM KCl are shown for comparison.

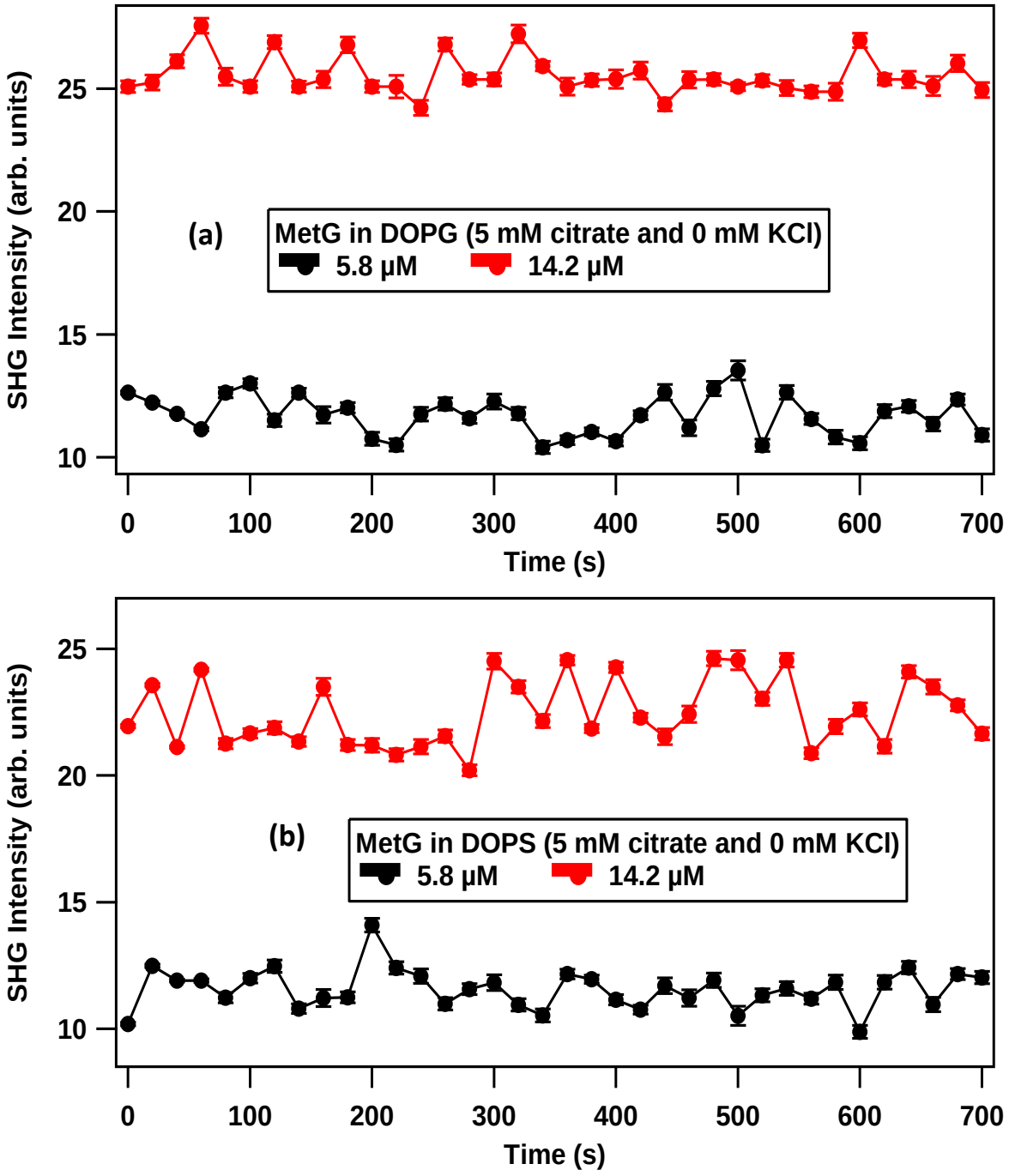

Figure A3.6. SHG data showing no adsorption to and no transport of MetG for (a) DOPG and (b) DOPS liposomes at various MetG concentrations in pH 4.0, 5 mM citrate buffer.

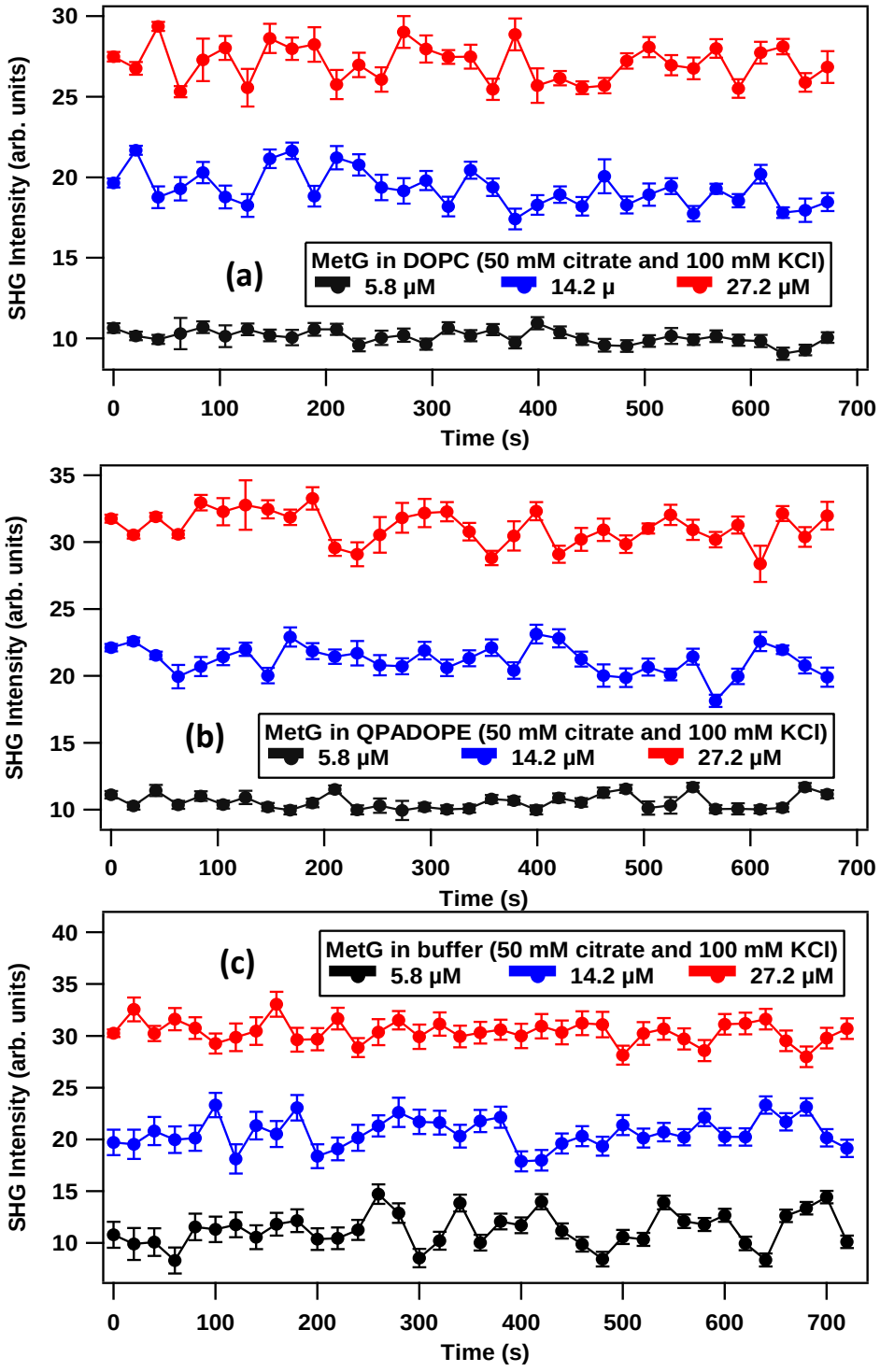

Figure A3.7. SHG data at pH 4.0 showing no adsorption to and no transport of MetG for (a) DOPC and (b) QDOPE liposomes at various MetG concentrations. SHG data of MetG alone (c) in pH 4.0, 50 mM citrate buffer with 100 mM KCl are shown for comparison.

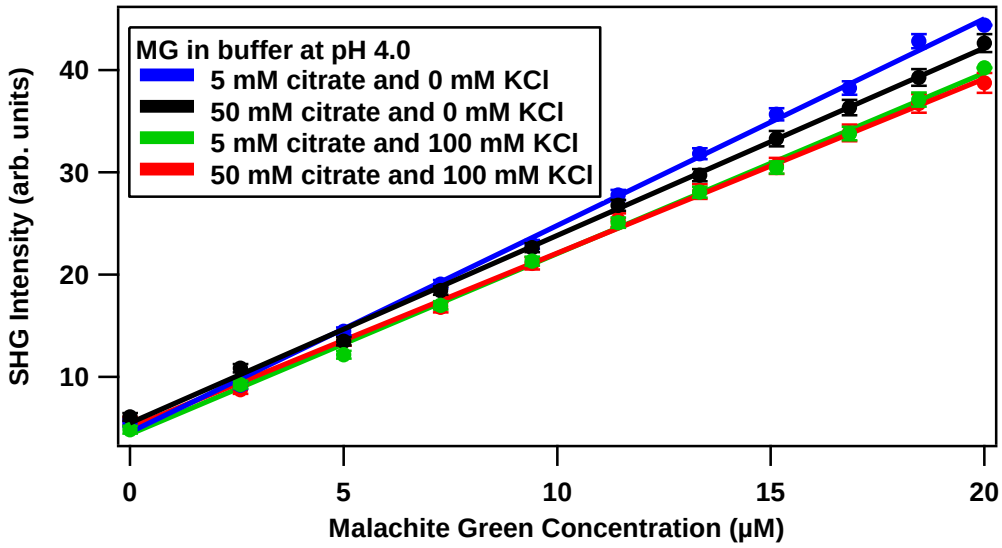

Figure A3.8. SHG signal intensity of malachite green dye as a function of concentration in different buffer concentrations, pH 4.0.

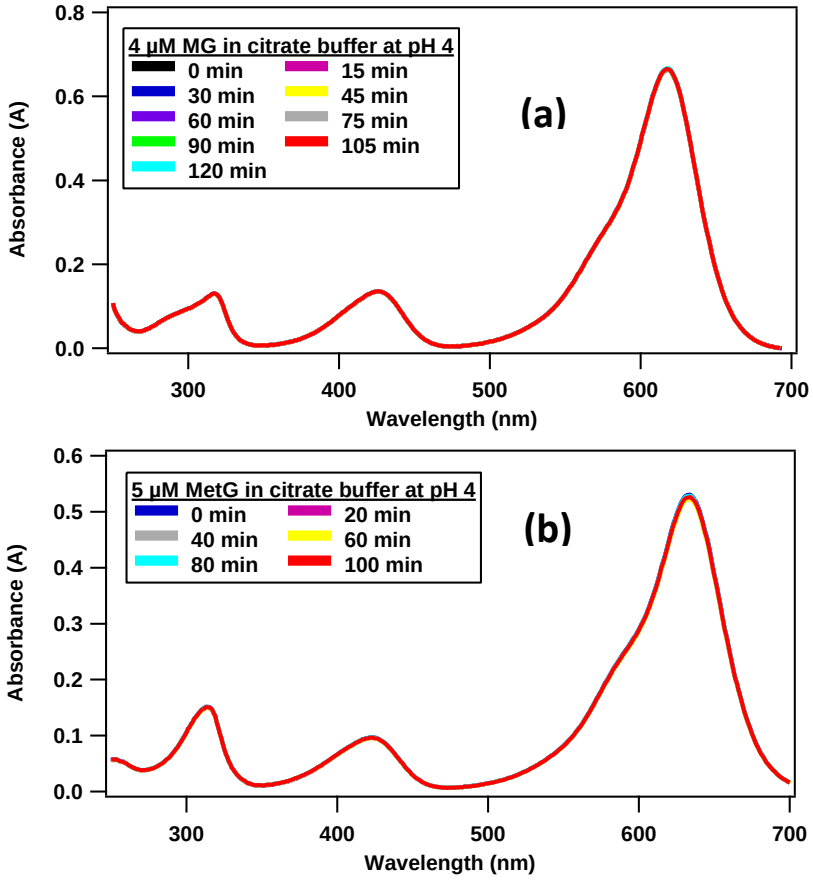

Figure A3.9. Absorption spectra of (a) malachite green and (b) methyl green in citrate buffer at pH 4.0.

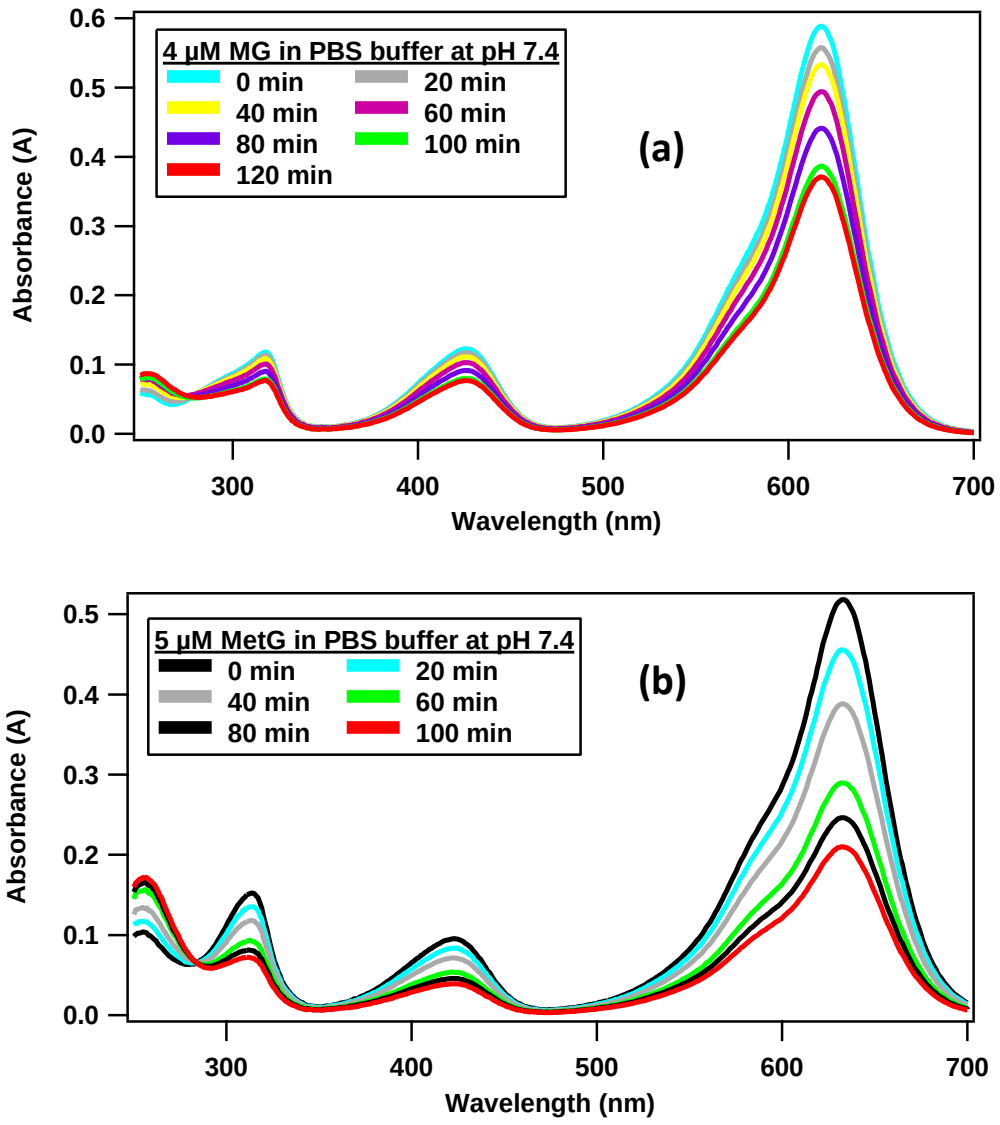

Figure A3.10. Absorption spectra of (a) malachite green and (b) methyl green in phosphate buffer at pH 7.4.

APPENDIX 4
PERMISSIONS

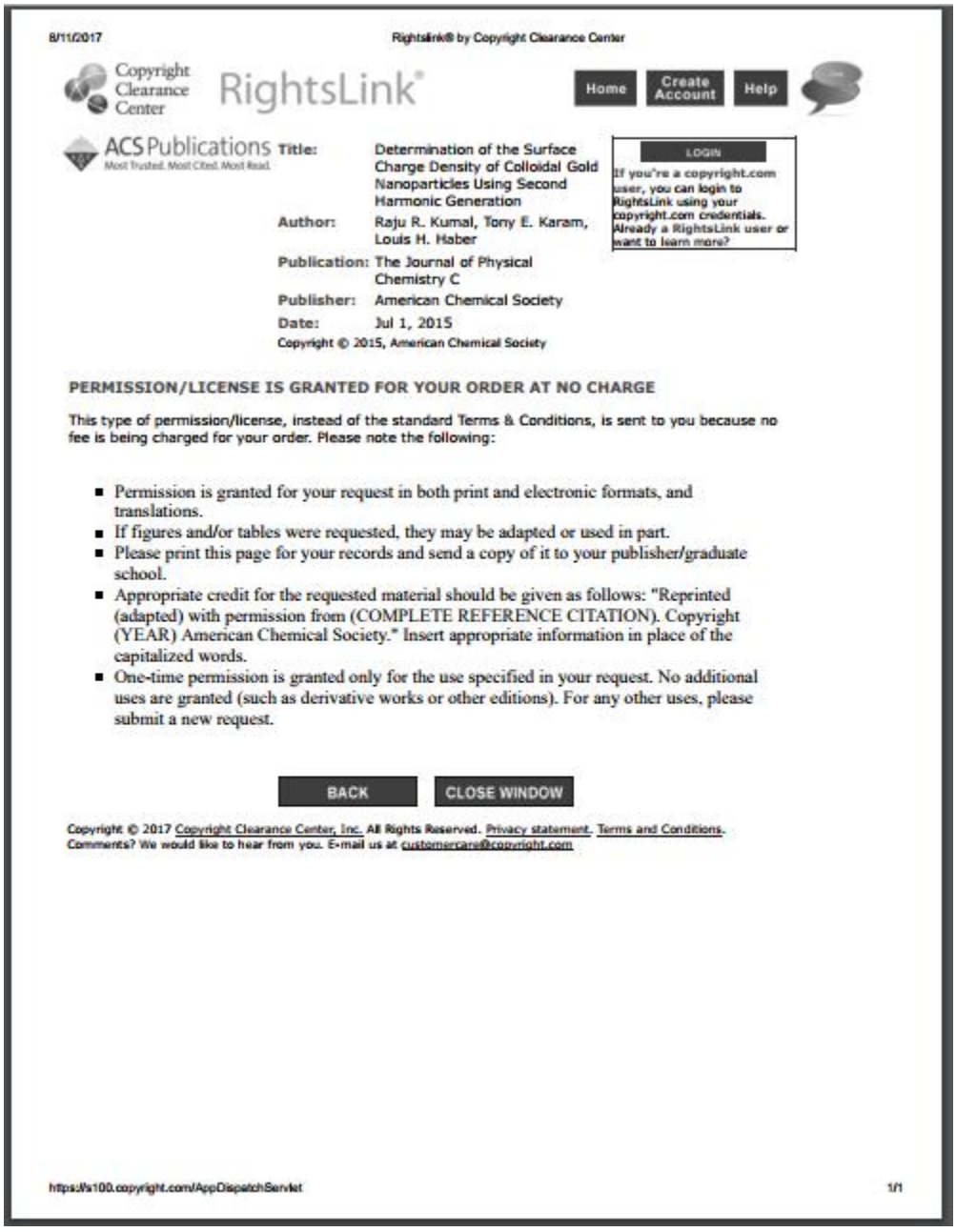

8/11/2017 RightsLink® by Copyright Clearance Center

Copyright Clearance Center RightsLink®

Home | Create Account | Help

ACS Publications Most Trusted. Most Cited. Most Read.

Title: Determination of the Surface Charge Density of Colloidal Gold Nanoparticles Using Second Harmonic Generation

Author: Raju R. Kumal, Tony E. Karam, Louis H. Haber

Publication: The Journal of Physical Chemistry C

Publisher: American Chemical Society

Date: Jul 1, 2015

Copyright © 2015, American Chemical Society

LOGIN

If you're a copyright.com user, you can login to RightsLink using your copyright.com credentials. Already a RightsLink user or want to learn more?

PERMISSION/LICENSE IS GRANTED FOR YOUR ORDER AT NO CHARGE

This type of permission/license, instead of the standard Terms & Conditions, is sent to you because no fee is being charged for your order. Please note the following:

- Permission is granted for your request in both print and electronic formats, and translations.
- If figures and/or tables were requested, they may be adapted or used in part.
- Please print this page for your records and send a copy of it to your publisher/graduate school.
- Appropriate credit for the requested material should be given as follows: "Reprinted (adapted) with permission from (COMPLETE REFERENCE CITATION). Copyright (YEAR) American Chemical Society." Insert appropriate information in place of the capitalized words.
- One-time permission is granted only for the use specified in your request. No additional uses are granted (such as derivative works or other editions). For any other uses, please submit a new request.

BACK | CLOSE WINDOW

Copyright © 2017 Copyright Clearance Center, Inc. All Rights Reserved. Privacy statement. Terms and Conditions.
Comments? We would like to hear from you. E-mail us at customercare@copyright.com

https://s100.copyright.com/AppDispatchServlet 1/1

RightsLink®

Home | Create Account | Help

Title:	Monitoring the Photocleaving Dynamics of Colloidal MicroRNA-Functionalized Gold Nanoparticles Using Second Harmonic Generation
Author:	Raju R. Kumal, Corey R. Landry, Mohammad Abu-Laban, et al
Publication:	Langmuir
Publisher:	American Chemical Society
Date:	Sep 1, 2015

LOGIN

If you're a copyright.com user, you can login to RightsLink using your copyright.com credentials. Already a RightsLink user or want to learn more?

PERMISSION/LICENSE IS GRANTED FOR YOUR ORDER AT NO CHARGE

This type of permission/license, instead of the standard Terms & Conditions, is sent to you because no fee is being charged for your order. Please note the following:

- Permission is granted for your request in both print and electronic formats, and translations.
- If figures and/or tables were requested, they may be adapted or used in part.
- Please print this page for your records and send a copy of it to your publisher/graduate school.
- Appropriate credit for the requested material should be given as follows: "Reprinted (adapted) with permission from (COMPLETE REFERENCE CITATION). Copyright (YEAR) American Chemical Society." Insert appropriate information in place of the capitalized words.
- One-time permission is granted only for the use specified in your request. No additional uses are granted (such as derivative works or other editions). For any other uses, please submit a new request.

BACK | CLOSE WINDOW

RightsLink®

Home | Create Account | Help

Title: Plasmon-Enhanced Photocleaving Dynamics in Colloidal MicroRNA-Functionalized Silver Nanoparticles Monitored with Second Harmonic Generation

Author: Raju R. Kumal, Mohammad Abu-Laban, Corey R. Landry, et al

Publication: Langmuir

Publisher: American Chemical Society

Date: Oct 1, 2016

LOGIN

If you're a copyright.com user, you can login to RightsLink using your copyright.com credentials. Already a RightsLink user or want to learn more?

PERMISSION/LICENSE IS GRANTED FOR YOUR ORDER AT NO CHARGE

This type of permission/license, instead of the standard Terms & Conditions, is sent to you because no fee is being charged for your order. Please note the following:

- Permission is granted for your request in both print and electronic formats, and translations.
- If figures and/or tables were requested, they may be adapted or used in part.
- Please print this page for your records and send a copy of it to your publisher/graduate school.
- Appropriate credit for the requested material should be given as follows: "Reprinted (adapted) with permission from (COMPLETE REFERENCE CITATION). Copyright (YEAR) American Chemical Society." Insert appropriate information in place of the capitalized words.
- One-time permission is granted only for the use specified in your request. No additional uses are granted (such as derivative works or other editions). For any other uses, please submit a new request.

BACK CLOSE WINDOW

RightsLink®

Home | Create Account | Help

Title: Impacts of Salt, Buffer, and Lipid Nature on Molecular Adsorption and Transport in Liposomes As Observed by Second Harmonic Generation

Author: Raju R. Kumal, Huy Nguyenhuu, James E. Winter, et al

Publication: The Journal of Physical Chemistry C

Publisher: American Chemical Society

Date: Jul 1, 2017

LOGIN

If you're a copyright.com user, you can login to RightsLink using your copyright.com credentials. Already a RightsLink user or want to learn more?

PERMISSION/LICENSE IS GRANTED FOR YOUR ORDER AT NO CHARGE

This type of permission/license, instead of the standard Terms & Conditions, is sent to you because no fee is being charged for your order. Please note the following:

- Permission is granted for your request in both print and electronic formats, and translations.
- If figures and/or tables were requested, they may be adapted or used in part.
- Please print this page for your records and send a copy of it to your publisher/graduate school.
- Appropriate credit for the requested material should be given as follows: "Reprinted (adapted) with permission from (COMPLETE REFERENCE CITATION). Copyright (YEAR) American Chemical Society." Insert appropriate information in place of the capitalized words.
- One-time permission is granted only for the use specified in your request. No additional uses are granted (such as derivative works or other editions). For any other uses, please submit a new request.

BACK | CLOSE WINDOW

VITA

Raju R. Kumal received a Master's of Science in Chemistry from Tribhuvan University of Nepal in 2008, where he studied corrosion behavior of alloys under varying pH conditions. He joined Professor Louis Haber's research group in fall 2012 in the Department of Chemistry at Louisiana State University. His research focuses on ultrafast and nonlinear spectroscopy and nanoparticle synthesis for potential applications in drug delivery, sensing, catalysis and photovoltaics.